Vertex Determination in the BRAHMS Experiment
and
Measurements of Centrality Dependent Charged Particle Production in Au–Au Collisions at $\sqrt{s_{NN}} = 130 AGeV$

Bjørn H. Samset
University of Oslo
May 11, 2001

Thesis presented for the Cand. Scient. degree (Master of Science).

Preface

For the last two years I have been working on this master thesis, dividing my time between the research group of Gunnar Løvhøiden and Trine Tveter at the Institute of Physics, University of Oslo, and the Brookhaven National Lab in New York where the BRAHMS experiment is located. They have been two very valuable years, and I hand in this product much wiser (I hope) than when I first heard the words RHIC, BRAT and *pseudorapidity density*. My thanks to Trine and Gunnar for making me feel included from the moment I came looking for a thesis subject, and for spending so much of their budget on my travels.

Thanks again to Trine and Alv Kjetil Holme who have been my supervisors, and who have always been there to discuss or help with whatever problems or frustrations I may have had. Trine has also done a formidable job proof–reading this thesis — without her help its $\frac{Stupid}{Smart}$ ratio would have been much, much higher.

The BRAHMS collaboration is a small one, but our experiment is quite complex. This means a lot of work for everyone, something especially valuable to an inexperienced master student. Outside of what is presented in the following pages I have been in touch with almost all of the diverse parts that make up a heavy–ion experiment, an experience bigger collaborations could probably not have provided. Thanks to spokesman Flemming Videbæk for letting me participate and do both software and physics — and to all the other members of BRAHMS whom I have discussed with or simply peppered with questions. In this field of physics the collaboration means everything.

Two years ago, I was the first BRAHMS student in Oslo. Since then we have grown to one of the institutes largest sub–groups, with the addition of Truls M. Larsen, Elin Enger and Mats Mikkelsen. Together we are starting to become a good team, and I think the Oslo group will contribute greatly to BRAHMS over the next few years. I know BRAT can be messy — don't give up!!!

Finally a thanks to my fiancé Elise Bergli, both for putting up with a tired and traveling boyfriend and for dragging me away from student politics for long enough to finish this thesis.

Oslo, May 2001
Bjørn H. Samset

Contents

Chapter 1

Introduction

The BRAHMS experiment is one of four detectors built around the new RHIC accelerator at the Brookhaven National Lab (BNL) in New York. RHIC saw its first nucleus–nucleus collisions in the summer of 2000, achieving a center–of–mass energy of $130GeV$ per colliding nucleon. This is almost an order of magnitude higher than what has previously been seen at the Alternating Gradient Syncrotron (AGS) at BNL and the Super Proton Syncrotron (SPS) at CERN, Switzerland, so the first RHIC data have been eagerly awaited by the heavy–ion community. It is hoped that at these energies we will come even closer to producing and studying deconfined, strongly interacting matter — a Quark–Gluon Plasma (QGP).

The major goal of the BRAHMS experiment is to study the production of charged hadrons over a wide range of rapidities and transverse momenta. This is interesting because many experimental QGP signals are predicted for these observables, and since RHIC is designed to collide any two systems ranging from protons to gold nuclei at energies up to $200AGeV$ we are in a unique position to study the systematics of hadron production in heavy–ion collisions.

In this thesis I present my two major contributions to the BRAHMS experimental effort. A central measurement for a collider experiment that must be made before any physics can be produced is the location of the collision, or the *vertex*, and extracting this information as precisely as possible has been one major part of my work. The other part deals with physics, as I extract the pseudorapidity density of produced charged particles ($dN/d\eta$) around midrapidity. This is information that will be included in an upcoming BRAHMS publication, relevant because it tells us something about the energy densities produced in our collisions and the degree of stopping that the colliding nuclei experience, and can also be used to discern between competing theoretical scenarios.

I will present this work in the following way:

First, in chapter 2, I will give the layman an introduction to way physics today views nature at its smallest scales. I will describe the fundamental particles that everything consists of and the laws they they obey, and then I will discuss the new state of matter called a *Quark-Gluon Plasma*, and how we hope it may be created from the forms of matter that we know.

In chapter 3 I move on to describe the field of *Relativistic Heavy-Ion Physics*. I will present both the essential part of the theoretical concepts behind what we do, and the experimental techniques we use to unwrap natures secrets. I will also go into some detail about the theoretical models that have been made of a relativistic nucleus–nucleus interaction.

Then, in chapter 4, I will describe in detail the RHIC accelerator and the BRAHMS experiment, and chapter 5 deals with the software that we use both for simulating our detectors and for extracting physics from our raw data. I also include a chapter on TPC technology, since a TPC is the main detector in both my result chapters.

Chapters 7 and 8 are about the work that I have done. I first describe in detail the software algorithms I have written for finding the interaction-point, or *vertex*, of a given nucleus-nucleus collision, and demonstrate their performances and efficiencies. Then I move on to describe and give results of my analysis of charged particle multiplicities ($dN/d\eta$) at midrapidity, based on data from the first year of RHIC running at $\sqrt{s} = 130GeV$.

Finally in chapter 9 I sum up my results and give some outlook to the future, and at the very end I include some appendices with more technical details about my analysis and software, and an updated list of the BRAHMS collaboration.

Chapter 2

Nature at its smallest scales

2.1 A brief history of elementarity

All matter that we see around us is composed of *atoms*, particles roughly $0.1nm = 10^{-10}m$ in diameter. The different atoms are the basic constituents of the over 100 known *elements* — Hydrogen, Helium, Lithium etc. — that make up the *periodic table of the elements* (see fig. 2.1). The newest element to be discovered, number 118, was seen only last year at Lawrence Berkeley National Lab in Berkeley, California.

The first periodic table, ordering the elements by their properties, was made in 1869 by D. Mendeleev. It was already then clear that for such a strong order to exist between the seemingly diverse atoms, they had to possess some kind of inner structure. This structure was partly revealed in 1897 and 1912, when J. J. Thompson and E. Rutherford, respectively, discovered a sub–atomic negatively charged particle known as an *electron* and that the positive charge of an atom was gathered in a clump of matter known as the *atomic nucleus*. Then, in the period up to 1950 — known as the "golden age of atomic physics" — it was discovered that the nucleus is composed of two more sub–atomic particles, the positively charged *proton* and the electrically neutral *neutron*. In addition, since the size of the nucleus was measured to be on the order of a few fm or $10^{-15}m$, physicists were lead to conclude that a new and unknown force was binding the protons and neutrons together. This force became known as the *strong nuclear force*. Table 2.1 summarizes the physicists' idea of elementarity around 1950. In addition, a positively charged particle with the same mass as the electron had been discovered, known as a *positron*.

This view was set to change, however. Experiments in the 60's and 70's probing the protons and neutrons gave results hinting at some even deeper inner structure, and theorists set to work making yet another new view of elementarity. A complicating factor was that for some reason the particles the experimentalists thought they saw inside the nucleons were never seen on their

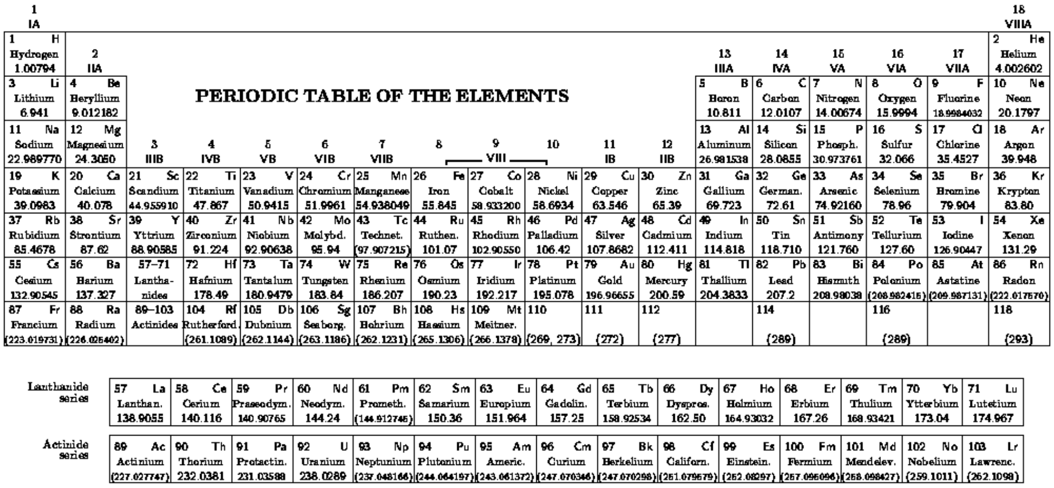

Figure 2.1: The periodic table of the elements, taken from ref. [1]

Particle	Symbol	Mass (MeV/c^2)	Electric charge
Proton	p	938	$+1$
Neutron	n	940	0
Electron	e^-	0.511	-1

Table 2.1: The particles thought to be elementary around 1950. The masses are the currently known values [1].

own. They seemed in some way *confined* to the nucleons.

In time, a clear theoretical picture formed that explained almost all of the observed features of the elementary particles. This theory is known as the *Standard Model of Particle Physics*, and describes our current view of what are the most elementary parts of Nature.

2.2 The Standard Model

The Standard Model (SM) is a quantum field theory attempting to describe all known elementary particles and their interactions. It includes the strong and weak nuclear forces and the electromagnetic force, but not gravity.

In SM, the nucleons are made up of massive *quarks* bound together by massless *gluons* — see fig. 2.2. The gluons are the carriers of the strong nuclear force just as photons are the carriers of the electromagnetic force. The SM

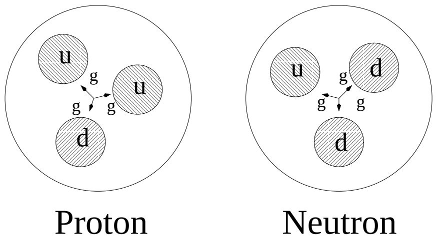

Figure 2.2: A very schematic picture of the nucleons.

predicts six quarks, ordered in *generations* according to their mass:

$$\begin{pmatrix} up : u \\ down : d \end{pmatrix} \begin{pmatrix} charm : c \\ strange : s \end{pmatrix} \begin{pmatrix} top : t \\ bottom : b \end{pmatrix} \tag{2.1}$$

These quarks have all been seen experimentally, but still only indirectly through their decays into other particles. This is because of a phenomenon, known as *quark confinement* — a fundamental property of Quantum ChromoDynamics (QCD), the theory describing the strong nuclear force. It states that at normal energies (to be defined below) the force between two quarks is proportional to their separation and therefore one can never see a free quark.

The electrons and positrons, known for almost 100 years, are still considered elementary, but they have acquired new properties and both heavier and lighter cousins. The known *leptons* are

$$\begin{pmatrix} \nu_e \\ electron : e^- \end{pmatrix} \begin{pmatrix} \nu_\mu \\ muon : \mu^- \end{pmatrix} \begin{pmatrix} \nu_\tau \\ tau : \tau^- \end{pmatrix} \tag{2.2}$$

where the ν's are massless or very light particles known as *neutrinos*.

In addition to these particle types, the SM includes force carriers for the three fundamental forces. They are the photon (γ) for the electromagnetic force, the $W^\pm$ and Z^0 for the weak nuclear force and as mentioned the gluon (g) for the strong nuclear force. Just as the photon mediates the electromagnetic force by coupling to electric charges, the gluon couples to something known as *color charges*. Only the quarks and gluons themselves are "colored", and therefore they are the only particles that feel the strong nuclear force.[1] Finally there is a particle known as the *Higgs boson*, needed by the theory to give mass to the particles. It is currently the only SM particle that has not been seen experimentally, though there were hints from the LEP accelerator at CERN in the autumn of 2000 that they had at least seen some Higgs candidates (see e.g. [3]).

[1] Notice the interesting property that this gives the gluons — they both carry and mediate color charge, and can therefore interact with themselves. See e.g. [2].

Quark	Mass	Electric charge (e)	Baryon number	Spin ($\hbar$)
u	1 - 5 MeV/c^2	+2/3	1/3	1/2
d	3 - 9 MeV/c^2	-1/3	1/3	1/2
s	75 - 17 MeV/c^2	-1/3	1/3	1/2
c	1.15 - 1.35 GeV/c^2	+2/3	1/3	1/2
b	4.0 - 4.4 GeV/c^2	-1/3	1/3	1/2
t	174.3 $\pm$ 5.1 GeV/c^2	+2/3	1/3	1/2

Table 2.2: Properties of the quarks [1]. Note that the definition of the quark masses is still controversial, since they are not individually measurable. The u- , d- and s-masses are the current quark masses, the c- and b-masses are the "running" masses and the t-mass is from directly observed events.

Lepton	Mass (MeV/c^2)	Electric charge (e)	Lepton number	Spin ($\hbar$)
e^-	0.5110	-1	$L_e = 1,\ L_\mu = L_\tau = 0$	1/2
ν_e	$< 3 \cdot 10^{-6}$	0	$L_e = 1,\ L_\mu = L_\tau = 0$	1/2
μ^-	105.7	-1	$L_\mu = 1,\ L_e = L_\tau = 0$	1/2
ν_μ	< 0.19	0	$L_\mu = 1,\ L_e = L_\tau = 0$	1/2
τ^-	1777	-1	$L_\tau = 1,\ L_e = L_\mu = 0$	1/2
ν_τ	< 18.2	0	$L_\tau = 1,\ L_e = L_\mu = 0$	1/2

Table 2.3: Properties of the leptons [1].

Tables 2.2, 2.3 and 2.4 summarize some important properties of the particles in the standard model.

In addition to the particles described above, there also exists a complementary set known as the *anti–particles*. They are identical in mass to their matter–cousins, but have opposite sign quantum numbers. Anti–particles are denoted with a bar over their name, e.g. an anti–u–quark is $\bar{u}$. The force–carriers are their own anti–particles, with the exception of the gluon which has an anti–particle with opposite color charge.

2.3 Hadrons and exotic particles

Of course, the quarks do not only form into protons and neutrons. These are only the lowest–mass species of a huge number of composite particles, and are therefore the ones that make up normal matter. Collectively, particles composed of quarks are known as *hadrons*.

[2] Carries dual color charge
[3] Still undiscovered — maybe seen at CERN last autumn? (see e.g. [3])

Force boson	Force	Mass (GeV/c^2)	Electric charge (e)	Spin ($\hbar$)
Photon, γ	Electromagnetic	0	0	1
Gluon[2], g	Strong nuclear	0	0	1
$W^{\pm}$	Weak nuclear	80.419±0.056	±1	1
Z^0	Weak nuclear	91.1882±0.0022	0	1
H^0	—	114.5??[3]	0	1

Table 2.4: Properties of the force carriers

There are two major types of hadrons:

- Baryons/antibaryons are composed of either three quarks or three anti-quarks respectively. The obvious examples are protons and neutrons, and more exotic species are e.g. $\Lambda(uds)$, $\Xi^0(uss)$ and $\Omega^+(\bar{s}\bar{s}\bar{s})$.
- Mesons are made up of one quark and one anti–quark. Typical examples are $\pi^+(u\bar{d})$, $\pi^-(\bar{u}d)$ and the oddly named $J/\psi(c\bar{c})$.

The standard model quite heavily constrains what quark–combinations are allowed in nature, demanding that they have an integer total baryon–number and no net color charge. Other combinations than the ones given above do satisfy this requirement, but none have ever been seen experimentally despite many active searches.

2.4 Nuclear matter

The atomic nucleus is a system tightly bound by the strong nuclear force. It is composed of protons and neutrons, or on a more fundamental level of u and d quarks and gluons binding them into hadrons.

As a collective system it can be ascribed a matter–density ρ varying with the radius, usually parameterized by

$$\rho_{A\leq 11} = \rho_0 e^{-\frac{r^2}{R^2}} \tag{2.3}$$

$$\rho_{A>11} = \rho_0 \frac{1}{1 - e^{\frac{r-R}{a}}} \tag{2.4}$$

where A is the number of nucleons, $\rho_0 \approx 0.15$ nucleons$/fm^3$ is the nuclear ground state density and

$$R = r_0 A^{\frac{1}{3}}; r_0 = 1.2fm \tag{2.5}$$

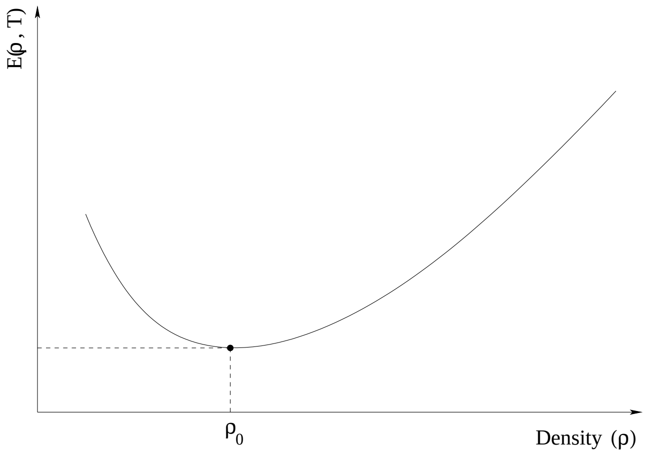

Figure 2.3: Schematic nuclear equation of state as a function of density. In nature the curvature around ρ_0 is very steep, meaning that it is hard to push nuclear matter away from its ground state.

is the nuclear radius. Equation 2.4 is known as a Woods-Saxon potential, where a is a parameter related to the diffuseness of the nuclear surface. Parameters and functional forms for different nuclei can be found e.g. in [4].

It was long believed that being bound so strongly, nuclear matter would be incompressible. This view changed with the development of machines like cyclotrons and linear accelerators, capable of smashing nuclei into each other at high energies and thus heating or deforming them. This opened the door to studying the entire nuclear phase diagram, or the nuclear *equation of state* which gives the energy content in infinite nuclear matter as function of pressure/density and temperature (see fig. 2.3).

The study of the parts of the phase–diagram far from the ground state is the business of *ultra–relativistic heavy–ion physics*, the field this thesis is about. More will be said about this in the next chapter.

2.5 Quark–Gluon Plasma

The picture drawn so far of matter can be summarized as follows:

Matter	$\Rightarrow$	Atoms
Atoms	$\Rightarrow$	Electrons and a nucleus
Nuclei	$\Rightarrow$	Protons and neutrons
Protons and neutrons	$\Rightarrow$	Gluons and confined quarks

That the quarks are confined means that they are bound to their respective nucleons, and cannot move freely within the nuclear volume.

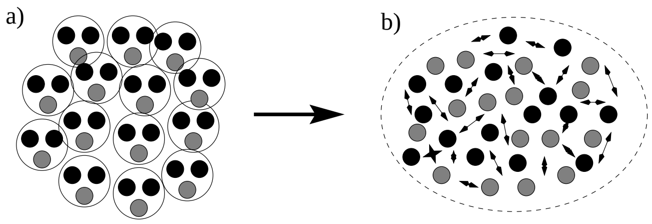

Figure 2.4: Very simplified picture of the QCD phase transition. a) Normal nuclear matter, i.e. an atomic nucleus. b) When the pressure or temperature is increased above some critical point, the nucleons "melt" into a soup of quarks and gluons known as a quark–gluon plasma.

2.5.1 A new state of matter?

In the 70's, theorists developing Quantum ChromoDynamics (QCD) discovered a phenomenon known as the *running coupling constant*. The coupling constant is a measure of the strength of a force, and what they discovered was that as the energy transfer between particles described by QCD increases the coupling constant decreases logarithmically.[4] This means that if there is enough energy in nuclear matter, either in the form of high matter density or high "temperature",[5] the force holding the quarks together may become weak enough that they cease to be confined. It is then possible that the nucleons may "melt" in a way analogous to when ice melts into water, leaving the quarks and gluons free to move in the entire deconfined volume. This hypothetical, totally new state of matter was in 1978 dubbed a *quark–gluon plasma* (QGP) by E. Shuryak [5, 6], and has been the object of heavy research for the last 25 years. See illustration in figure 2.4.

2.5.2 The nuclear phase diagram

With this information, we can now try to draw the theoretically expected phase diagram for nuclear matter — see fig. 2.5.

The $\rho - T$ plane shows the part of the diagram that I have discussed so far. Notice that the part of phase space occupied by "normal nuclei", i.e. nuclear matter in its ground state, consists of only one point. All the other points in this complex picture have to be reached artificially through some kind of experimental setup. This, again, is the topic of the next chapter.

[4] A phenomenon known as *asymptotic freedom*.

[5] It is not established that one can really use the term temperature for nuclear matter, since it usually consists of a finite number of particles. However a grand canonical formalism, employing the parameters T (temperature) and μ (chemical potential), is often used in statistical (fireball) nuclear models and the term temperature has entered the common vocabulary.

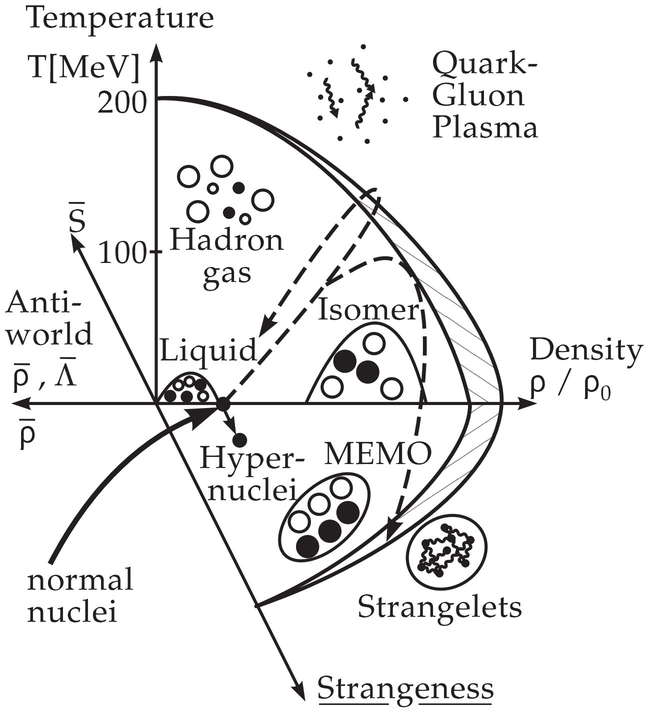

Figure 2.5: The nuclear phase diagram, in a rather complicated form. Taken from [7].

There are two other points of immediate interest in figure 2.5. First, the boundary between the gaseous phase of confined hadrons and the deconfined QGP is not drawn sharply. This is because several theorists predict a second–order phase transition[6], leading to the possibility of a *mixed phase* where confined and deconfined matter coexist. Second, note that since the phase boundary spans the entire $\rho - T$ plane we can predict two very different types of QGP. One kind is formed when the baryon density ρ gets high enough, and will have a high baryon–to–antibaryon ratio because of the quarks in the initial baryons. The other kind forms when there is low or zero baryon density but high temperature — a state called an *excited vacuum*. In the extreme limit this QGP will have a vanishing baryon–to–antibaryon ratio, since all particles in it will be formed by quark–antiquark pair creation. The distinction between these two types of QGP is important, since they will have very different observable properties (see section 3.5).

[6]The distinction is as follows [8]:
First order = sharp transition, abruptly changing the entire system from one phase to another.
Second order = gradual phase transition, up to a point where the entire system is in the new phase.

2.5.3 QGP in Nature?

On Earth, there is no place with a high enough natural temperature or density to support a stable quark–gluon plasma. Still, there are two places in the space–time of the Universe where it is of high relevance.

One is the center of neutron stars. A neutron star is a star that has undergone a supernova explosion and subsequently collapsed, and massive enough that the gravitational pressure is balanced only by the strong nuclear force working between neutrons. Some theories predict that the dense centers of such stars are made up of deconfined matter[9], so future observations of neutron stars may give us important information about the nuclear equation of state. Since a neutron star has high density but approximately zero temperature, this would be an example of the first kind of QGP mentioned in section 2.5.2.

The other instance where QGP is important for our understanding of Nature is in the Big Bang — the way cosmologists believe our universe began. All energy then started expanding from a single point, and approximately 10^{-6} seconds afterwards the entire universe is thought to have been in a state of quark–gluon plasma. Understanding the QCD phase transition is therefore important also for our understanding of the evolution of the early universe and the way matter formed from the initial energy[7]. Since there were no baryons — i.e. quarks — present when the universe began, this is an example of the second kind of QGP presented in section 2.5.2.

2.6 Where do we stand?

So where do we currently stand in our understanding of QCD and nuclear matter? We face a major problem in that since QCD is both non–perturbative and confined at all accessible energies, neither theorists nor experimentalists can give a clear idea of what is "supposed" to happen. Theories and large–scale simulations (to be described in chapter 3) are still struggling to achieve a rough understanding of infinite[8], thermalized matter in equilibrium, while the QCD plasma that we hope to create in today's and tomorrow's particle accelerators is very far from equilibrated. There is a genuine concern[7] that this difference between the theoretical and experimental situation may be misguiding both experimental design and interpretations of experimental results.

That was the sceptic's view. On the other hand, a lot of strong theoretical predictions have been confirmed by experimenters at e.g. the AGS and SPS, and we have a large amount of experimental results that show the systematics of nuclear matter under different conditions. This at least gives us a clear

[7] A process known as *hadronization*.

[8] Or, in the case of lattice QCD periodic.

phenomenological understanding of what we study, and the current culmination of this understanding came in February 2000 when seven experiments at CERN issued a joint statement saying that they had enough experimental evidence to claim that they had seen the creation of *a new state of matter*[10]. Whether this new state is the predicted Quark–Gluon Plasma or a transition into an excited hadron gas dominated by mesons and baryonic resonances[7] is still under debate, but there is little doubt in the community that we are seeing the onset of new physics, and that we can at least not understand heavy–ion interactions at the current $\sqrt{s}$ energies[9] simply in terms of hadronic degrees of freedom. We have to consider the properties of the partons, or quarks, that make up the hadrons, and this puts both experimentalist and theorists in a largely unknown — and therefore very exciting — territory. It is worth bearing all of this in mind as I now move on to introducing some central concepts of ultra–relativistic heavy–ion physics.

[9] See chapter 3.

Chapter 3

Ultra–relativistic heavy ion physics

Having in chapter 2 presented the way we currently view nature at its smallest scales, I will now move on to describing how we go about exploring the nuclear phase diagram.

This is currently the business of a research field known as *Ultra–relativistic heavy ion physics*, or *UrHIP* for short. The stated goal of UrHIP is to explore the properties of nuclear matter under extreme conditions, both phenomenologically through experiments and theoretically through thorough QCD calculations and mathematical models. In fact, UrHIP has been one of the few fields where experimental and theoretical knowledge have advanced at roughly the same pace and thus provided valuable input to each other.

The term *ultra–relativistic* deserves explanation. As I will explain below, we deal with matter accelerated to way above $0.1 \cdot c$ [1] meaning we have to use a relativistic formalism to describe our experiments mathematically. The term *relativistic* has traditionally been used for beam energies of around $100AMeV$, while *ultra–relativistic* means a beam energy of $10AGeV$ or higher — see table 3.1 below for examples of todays energies.

3.1 Creating QGP in the lab

To explore the different parts of the phase diagram in figure 2.5, we need some way of compressing and/or heating nuclear matter. The way the UrHIP community goes about this is to build particle accelerators — huge machines that strip the electrons from heavy atoms, accelerate them as much as possible and then smash them into each other. An individual collision of this type, known as an *event*, is the basic experimental situation in UrHIP and all our results are based on analyzing what comes out of such a high–energy collision. Table 3.1 list some recent heavy–ion accelerators and some of their important properties. For further discussion of experimental methods, see chapter 4.

[1] c is the speed of light: $c = 3.0 \cdot 10^8 m/s$

Accelerator	Type	Maximum CM energy	Status
AGS (BNL)	Fixed target	4.6 $AGeV$	Start: 1960, running
SPS (CERN)	Fixed target	17.3 $AGeV$	Start: 1976, running
RHIC (BNL)	Collider	200 $AGeV$	Start: 2000, running
LHC (CERN)	Collider	6.3 $ATeV$	Will start in 2005

Table 3.1: The most recent major heavy–ion accelerator facilities

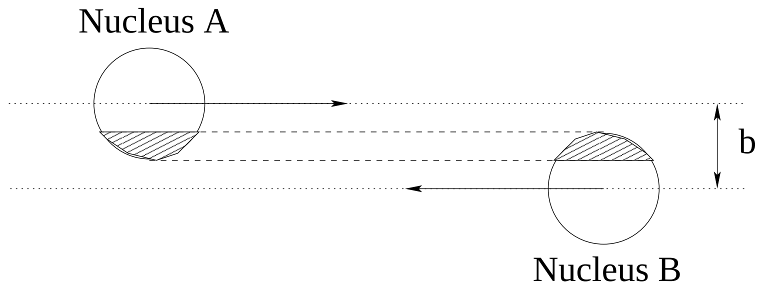

Figure 3.1: The impact parameter b of a heavy–ion collision is the radial distance between the centers of the colliding nuclei. Also, the shaded areas show the region of each nucleus that is assumed to participate in the collision.

The theoretical *ansatz* is that in a heavy ion collision, we create a region of nuclear matter that is excited away from its ground state and into the unknown regions of figure 2.5. The exact way that this happens and what mechanisms that contribute is still under dispute (see below), but it is well established that we are at least able to raise the energy density and/or temperature of the interacting matter significantly, allowing for the study of processes not seen anywhere else on earth.

3.2 Some theoretical concepts

Before going into the details of a collision, it is necessary to introduce a few theoretical concepts of heavy–ion physics. The terms presented here will be employed extensively in this entire thesis.

3.2.1 Impact parameter

Figure 3.1 illustrates the situation just before a collision, with two nuclei approaching each other. The *impact parameter* b of a collision is defined as the distance between the extrapolated trajectories of the centers of the colliding nuclei.

3.2.2 Relativistic kinematics and rapidity

As mentioned above, our nuclei are collided at velocities very close to the speed of light. This means that we have to use a relativistic mathematical formalism, and that we have to be careful which *reference frame* our calculations are made relative to. This is because the Galilean transformations

$$v = v' + u \tag{3.1}$$

break down for $v \gtrsim 0.1 \cdot c$ and we have instead to use the Lorentz transformation

$$v = \frac{v' + u}{1 + \frac{v'u}{c^2}} \tag{3.2}$$

(See e.g. [11].) Here, v is the velocity of an object as seen from a reference frame S, v' is the velocity seen from another frame S' moving with velocity u relative to S.

In UrHIP, the usual reference frames are the *lab frame* where the detectors are at rest, and the *center–of–mass frame*, or CM frame, where the total momentum of the colliding particles is zero. An important value related to the CM frame is the center–of–mass energy s, defined as [2]

$$s = -c^2(p_1 + p_2)^2 + (E_1 + E_2)^2 \rightarrow (E_1 + E_2)^2_{CM} \tag{3.3}$$

where p and E are the momenta and energies of the colliding particles, which reduces to the square of the sum of the energies of the colliding particles when measured in the CM frame. From the above we can see the major advantages of collider experiments over fixed target experiments — in a collider the lab and CM frames are the same, and since the momentum to be conserved in the CM frame is zero the entire energy $\sqrt{s}$ is available for particle production and (hopefully) QGP creation.

For simplicity, we would prefer an alternative quantity to the velocity that is relativistically additive. Such a quantity is the *rapidity*, defined as

$$y = tan^{-1}(v/c) \tag{3.4}$$

where we have the transformation

$$y = y' + y_{S'} \tag{3.5}$$

between two frames S and S' with a relative rapidity $y_{S'}$.

[2] s is actually one of the three *Mandelstam variables*, Lorentz invariant quantities defined for all reference frames. I will only use it in the CM frame, where its definition reduces to the right side of eq. 3.3.

The relativistic expression for a particles total energy E is

$$E^2 = p^2c^2 + m^2c^4 \tag{3.6}$$

where m is the rest mass. We can decompose the particles momentum p into a longitudinal and a transverse component:

$$p^2c^2 = p_L^2c^2 + p_T^2c^2 \tag{3.7}$$

If we then introduce a quantity known as the *transverse mass* m_T

$$m_T^2c^4 = p_T^2c^2 + m^2c^4 \tag{3.8}$$

we can rewrite eq. 3.6 as

$$E^2 = p_L^2c^2 + m_T^2c^4 \tag{3.9}$$

and the expression for the rapidity becomes

$$y = \frac{1}{2}ln\frac{E + p_Lc}{E - p_Lc} \tag{3.10}$$

In this form it is easy to see that for relativistic energies $pc \gg mc^2$ we can approximate the rapidity as

$$y \approx \frac{1}{2}ln\frac{pc + p_Lc}{pc - p_Lc} \tag{3.11}$$

and based on this we define the *pseudorapidity* η:

$$\eta \equiv \frac{1}{2}ln\frac{p + p_L}{p - p_L} \tag{3.12}$$

We can simplify this expression even further by introducing the *scattering angle* θ between the momenta of an incoming nucleus and the scattered (or produced) particle:

$$\eta = ln(cot\frac{\theta}{2}) = tanh^{-1}(cos\theta) \tag{3.13}$$

See figure 3.2 - as defined, the rapidity is zero for particles traveling perpendicular to the incident beam and then goes to $\pm\infty$ as the scattering angle goes to 0^o or 180^o.

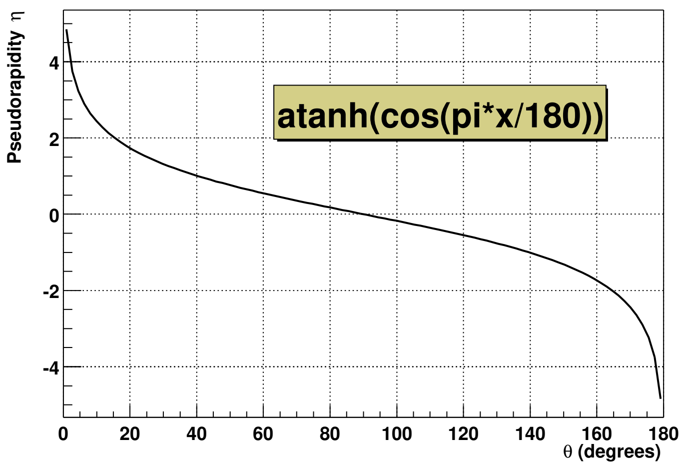

Figure 3.2: The pseudorapidity η (y axis) as a function of the scattering angle of a particle's momentum relative to that of the incident beam.

3.3 Basic collision models

Having defined a number of quantities relevant to heavy–ion collisions, the next step is to try to theoretically describe a collision from the point where the nuclei start colliding and up to the resulting spectra of hadrons. To do this, however, there are two major problems that have to be overcome. The first is the complexity of the colliding systems — a central $Au - Au$ collision involves $197 \cdot 2 \cdot 3 = 1182$ valence quarks, at least an equal number of gluons and even $q\bar{q}$ pairs drawn from the Fermi sea. This makes for an enormously complex many–body problem, in practice unsolvable. The second problem, even more fundamental, is that the QCD, which describes the relevant forces, is non–perturbative at all but the highest energies. Therefore an exact calculation of a heavy–ion collision is not only practically but also theoretically impossible.

To overcome these problems, one must make phenomenological models of the collision. The hope is that if the correct physical effects are included in a model then it should accurately describe and predict experimental results.

3.3.1 Participants and spectators

A first assumption one usually makes is to say that the nucleons in the colliding nuclei can be divided into two groups — the *participants* that lie within the regions of the colliding nuclei that overlap, and the *spectators* that make up the rest of the nuclei (see fig. 3.1). The participants will interact and make up what is known as the *fireball*, while the spectators will keep on moving forward and not notice the collision until (relatively) much later.

A concept that is much used in current papers is the *number of participants*, or N_{Part}. In the simple participant–spectator picture N_{Part} is of course just the sum of the number of nucleons in the overlapping regions of the colliding nuclei.

3.3.2 Bjorken vs. Landau

The next question is what happens to the participants. At the simplest level, one can ask whether they stop each other completely in the collision or if they are to some degree transparent to each other. The extremes of these views, full stopping or full transparency, are known respectively as the Landau and Bjorken limits.

In the Landau picture, because the strong nuclear force conserves quark flavor, the quarks in the incident nucleons are still present and we have a high net baryon density. This has many important effects on what processes we can expect to take place inside the fireball, and we will for example expect a low antibaryon–to–baryon ratio if we observe all the produced particles. These conditions are conjectured to be similar to those near the centers of heavy neutron stars.

The Bjorken picture will produce quite different results, since all the incident baryons are assumed to fly almost straight on with just a small rapidity loss relative to the beam rapidity. In the fireball we instead start with what has been called an *excited vacuum* — a state that has a zero density of all conserved quantum numbers, i.e. where all particles have been produced by particle–antiparticle creation. Here, we expect a antibaryon–to–baryon ratio of exactly unity. These conditions are thought to be similar to those that existed in the entire universe some 10^{-6}s after the Big Bang.

For an extended discussion of nuclear stopping, see sec. 8.10.

Experimental results

Experimental results on the antibaryon–to–baryon ratio from several accelerators and experiments show that we have a gradual transition from the Landau picture in central collisions at energies around $\sqrt{s} = 5 - 10AGeV$ to something much closer to the Bjorken scenario at the yet highest obtained energies, $\sqrt{s} = 130AGeV$ at RHIC. Table 3.2 shows the reported $\bar{p}/p$ numbers at midrapidity from AGS (E802), SPS (NA49) and RHIC (BRAHMS), and figure 3.3 shows the BRAHMS preliminary numbers in detail.[3] The trend indicates that when the LHC comes online in 2005 with $\sqrt{s} = 6300AGeV$ we will achieve close to full transparency, and we will then have colliders and experiments that can

[3]This measurement is submitted by BRAHMS for publication in Phys. Rev. Lett.

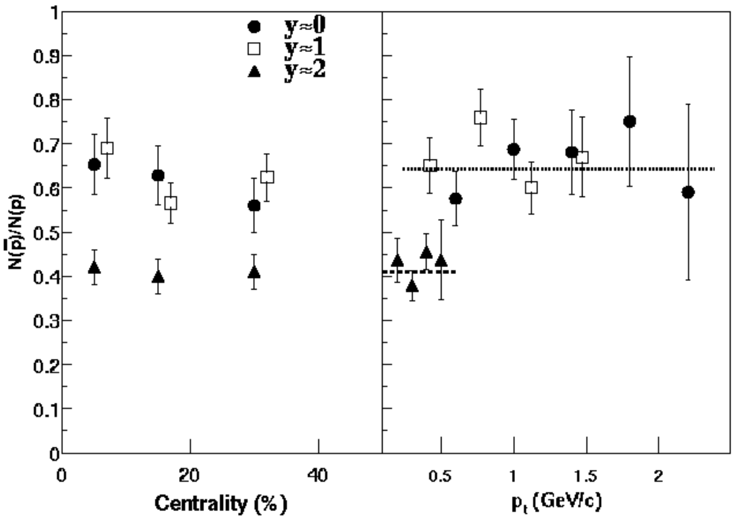

Figure 3.3: The production of antiprotons over protons at $\sqrt{s} = 130GeV$ as a function of centrality and rapidity, as measured by BRAHMS. Preliminary results.

Experiment	$\sqrt{s}$ (GeV)	$\bar{p}/p$	Ref.
E802 (AGS)	5	$\sim 2.5 \cdot 10^{-4}$	[12]
NA49 (SPS)	17	~ 0.1	[13]
BRAHMS (RHIC)	130	0.64	[14]

Table 3.2: Ratios of anti–proton to proton production at midrapidity for three energy regimes.

study both the baryon–rich and baryon–free types of QGP extensively in the lab.[4]

3.3.3 Glaubers and Wounded Nucleons

Two other models deserve mention here because they are very relevant for the rest of this thesis.

[4]Unfortunately ALICE will not have detectors looking at the baryon–rich forward rapidities.

The Glauber model

The first is the *Glauber model* of nucleus–nucleus interactions, which is a very simple but much–used way of calculating nuclear cross–sections [5] and the number of participants. Let A and B be the colliding nuclei. Then the total inelastic cross–section in the Glauber model is written as ([15])

$$\sigma_{in}^{AB} = \int d\vec{b}\{1 - [1 - \sigma_{in} T_{AB}(\vec{b})]^{AB}\} \tag{3.14}$$

where $T_{AB}(\vec{b})$ is the nuclear overlap function

$$T_{AB}(\vec{b}) = \int d\vec{b}_A dz_A d\vec{b}_B dz_B \rho_A(\vec{b}_A, z_A)\rho_B(\vec{b}_B, z_B) \times \delta(\vec{b} - \vec{b}_A - \vec{b}_B) \tag{3.15}$$

and $\vec{b}$ is the impact parameter in two transverse dimensions. $\vec{b}_A$ and $\vec{b}_B$ are parameters spanning the transverse areas of nuclei A and B, z_A and z_B span the longitudinal lengths, and ρ_A and ρ_B are the nuclear matter densities (see sec. 2.4. σ_{in} is the inelastic nucleon–nucleon cross–section, well measured by several experiments.[6]

Equation 3.14 has a simple interpretation. σ_{in}^{AB}, the total inelastic cross–section, is the probability for any interaction integrated over all impact parameters. For a specific b, this is one minus the probability for no interaction at all, which is in turn one minus the probability for any NN interaction multiplied $A + B$ times. The nuclear overlap function $T_{AB}(\vec{b})$ modifies this probability according to the densities of A and B and how much they overlap for a given b.

Using these equations we can sample the impact parameter using standard Monte–Carlo techniques on the probability density

$$\frac{dP(b)}{b} = \frac{1 - [1 - \sigma_{in} T_{AB}(b)]^{AB}}{\sigma_{in}^{AB}} \tag{3.16}$$

giving a realistic distribution of impact parameters taking the nucleus–nucleus cross–section into account.

After this selection, the Glauber model assigns random spatial coordinates to the nucleons according to the densities used in eq. 3.15, and then decomposes each nucleus into tubes of radius $(\sigma_{in}/\pi)^{1/2}$. One then assumes that all nucleons from nucleus A collide with all nucleons in nucleus B that fall within such a tube centered on the A–nucleon, neglecting exchange of nucleons between tubes. The number of participants is then just the number of nucleons that interact with at least one other, and adding additional assumptions one can easily calculate transverse momentum production etc. from this basic picture.

---

[5] The *cross–section* of a process is essentially the probability that this particular process will occur given a specified initial condition. It is called a cross–section because it has dimension *length*^{2}, and the usual unit is the *barn*. $1barn = 1 \cdot 10^{-28} m^2$

[6] σ_{in} varies with the beam energy. Often used values are $\sigma_{in} = 37 \pm 1mb$ for $\sqrt{s} = 56AGeV$ and $\sigma_{in} = 42 \pm 1mb$ for $\sqrt{s} = 130AGeV$. ([16])

The Wounded Nucleon model

The *Wounded Nucleon model* deals with the systematics of the hadron production in a heavy–ion collision. It assumes that this complex reaction can be understood in terms of single proton–nucleus collisions, and consequently that the production of hadrons scales with the number of participating, or wounded, nucleons, i.e.

$$< N_{Produced\ particles} > \propto N_{Wounded} \tag{3.17}$$

This description is relevant because it has been very successful at describing the systematics seen at SPS energies, while it has been conjectured that once we achieve a significant degree of hard scatterings in a collision we will see a deviation from this behavior signaling the onset of perturbative QCD–related phenomena — i.e. we will see experimental variables with a component scaling as $N_{Collisions}$. A hard scattering is defined as a parton–parton scattering transferring enough transverse momentum that the reaction can be treated perturbatively in QCD, meaning $p_T \gg \Lambda_{QCD} \approx 200MeV$ where Λ_{QCD} is the energy scale where the QCD coupling constant α_s becomes large, i.e. non–perturbative, when going towards smaller p_T. I will discuss this further in chapter 8.

3.4 Event generators — more complex models

As explained in section 2.5, QCD is a confined theory — its basic degrees of freedom, the quarks and gluons, can never be observed directly. Due to this and other fundamental problems it is presently not feasible to calculate the outcome of a heavy ion collision from first principles. The basic models above allow us to describe very general things about the reaction dynamics, but to predict things like the production rates of different particles, the entropy production or, especially, a possible phase transition to a deconfined phase, we need to include proper QCD, QED, statistical physics etc. in our models.

Many theorists have tried to model QCD at collider energies and densities, employing principles ranging from classical strings to relativistic quantum field theory, from purely hadronic reaction mechanisms to full partonic transport models. To make their predictions testable, theorists publicize these models in the form of *event generators* — Monte Carlo (MC) based algorithms that propagate two particles or nuclei through a collision, using the theorist's model and all known data on elementary particles and their cross–sections to calculate

- how energy is deposited and distributed in the collision
- what particles are produced in the collision
- how the colliding nuclei interact and fragment

etc. An event generator is thus a simulation of a collision between elementary particles or nuclei.

There is a large amount of different event generators currently employed by different people. At a quick glance, the models can be divided into three subgroups according to their main assumptions: [7]

- Parton cascade models that use transport theory to evolve partonic degrees of freedom. Most of them follow these three steps:

  1. Initialization where the colliding nucleons are divided into parton substructure using measured structure functions.
  2. Partonic stage where the interactions of the parton ensemble are modeled by perturbative QCD. Multiple scattering is in general included, but effects like quantum interference is as yet poorly treated. Also includes non–perturbative scatterings, usually treated in the string formulation.
  3. Hadronization where the scattered partons are recombined into hadrons — mostly via string fragmentation (see below) or quark coalescence. Because of their partonic and perturbative nature, parton cascade models have been used mostly for the highest–energy situations like RHIC and LHC collisions.

- Hadronic transport models that mainly treat the hadronic degrees of freedom. They decompose a nucleus–nucleus collision into a sequence of binary collisions between baryons, strings and sometimes diquarks (one quark scatters of another and makes a string). These models are important in that they show what to expect if only hadronic degrees of freedom are relevant and thus allow for the prediction of QGP/parton d.o.f. signals.

- Nuclear fluid dynamics are models that assume that the fireball is in local equilibrium and conserves momentum and energy — an idealized continuum description. They are well suited for studying kinematic observables such as flow, and are practical in that a phase transition can be explicitly included through the equation of state. If one makes an ideal fluid approximation the equation of state is actually the only input to the equations of motion that depends on the matter under study. Nuclear fluid dynamic models are therefore very "clean" models where one can specify the kind of scenario one wants to simulate and examine the consequences.

I'll here briefly present some models that have been and are important to the field. I am by no means trying to be complete, but I have tried to select models that include different physics and that have been used or discussed in relation to RHIC physics. Table 3.3 summarizes the EGs described below.

Event generator	Type	Comment
FRITJOF [17]	Hadronic transport	Classical strings
VENUS [18]	Hadronic transport	Relativistic strings, Gribov–Regge
HIJING [19]	Parton cascade	pQCD, jet quenching, shadowing
neXus [20]	Parton cascade	Universality hypothesis
UrQMD [21]	Quantum field approach	Complex rescattering
EKRT [22]	Hydrodynamics	QCD saturation

Table 3.3: Some event generators relevant to RHIC physics. See the text for explanations.

3.4.1 Classical string theory

Before describing FRITJOF and VENUS, it might be useful to briefly review a concept that has been central to many of the most successful pre-RHIC event generators — classical string theory.

Classical string theory [18] deals with two–dimensional objects called *strings* in four–dimensional Minkowski–space. The strings are parameterized by a spacelike parameter τ and a timelike parameter σ

$$x = x(\tau, \sigma) \tag{3.18}$$

and are subjected to requirements such as invariance under gauge–transformations

$$\begin{pmatrix} \tau \\ \sigma \end{pmatrix} \rightarrow \begin{pmatrix} \bar{\tau}(\tau, \sigma) \\ \bar{\sigma}(\tau, \sigma) \end{pmatrix} \tag{3.19}$$

locality, covariance etc. From this we can construct a Lagrangian and an action for strings, and extract equations of motion.

The simplest solution to these equations is known as the *yo–yo string* — simply a line along a single spatial dimension. The endpoints of this line will fluctuate periodically (see fig. 3.4), and the endpoints and interior can be shown to have very different mathematical properties. One can also construct ways in which a string can break forming two new strings, or in which strings can recouple or exchange parts of themselves — see e.g. fig. 3.5

What connects this model to high–energy physics is the interpretation one can give to this yo–yo string. The string itself has similarities to the color–flux tube connecting e.g. two quarks, and the endpoints to the quarks themselves. The period of the string oscillations is related to the energy and momentum of the quark pair, and in this interpretation the string fragmentation models contain energy and momentum conservation.

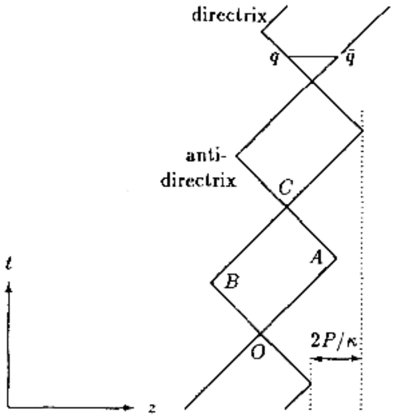

Figure 3.4: A string, oscillating in space (z) as it evolves in time (t).

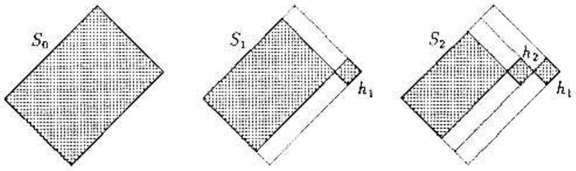

Figure 3.5: Fragmentation of an excited string S_0 into a new excited string S_1 and a hadron h_1 etc. The area of each shaded region can be interpreted as the energy of the string or particle.

3.4.2 FRITJOF

One model that employs classical string theory is FRITJOF, made by a group from Lund University. It has undergone several revisions, but the latest version, 7.02, was written by Hong Pi in 1992[17]. FRITJOF is important to BRAHMS, since it is the event generator that we have mostly used in simulating our detectors. The main reason for this is that FRITJOF predicted the highest multiplicities of produced particles at RHIC energies, and therefore using FRITJOF ensured that we did not underpredict the requirements on our experimental hardware.

The basic idea in FRITJOF is that the original partons in a nucleon can be seen as low–mass strings, and that when two nucleons collide you get longitudinal excitations of these strings and the possible exchange of incident partons. (See fig. 3.6) The collision itself is modeled as in Glauber theory, i.e. using a geometrical picture of a nucleus–nucleus where all nucleons inside a "tube" will interact. This can, amongst other things, lead to multiply excited strings,

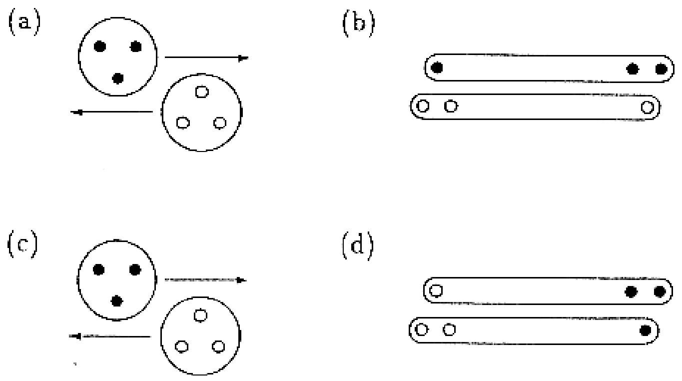

Figure 3.6: Two possible excitations, with and without parton exchange.

or *kinky* strings. A kink in a string is a point on the string interiors that has a transverse momentum component, interpreted by the Lund group as a gluon. Kinky strings turn out to provide, through fragmentation mechanisms (see below), a higher multiplicity than straight ones.

Once the primary nucleon–nucleon interactions are calculated, FRITJOF calls the routine JETSET [23, 24] which fragments the strings, meaning that it splits the strings into shorter and shorter sub–strings until it reaches something that can be identified with hadrons. This process also induces transverse momentum in the particles, so that after fragmentation a complete set of produced particles and momenta exists.

There has long been a discussion about whether or not rescattering of the produced particles is a major effect in determining the final state. FRITJOF has elected to ignore all rescattering, excluding this possibility from the model.

Up until the last revision FRITJOF was solely based on classical string theory, using no input from quantum mechanics or QCD. By its phenomenological nature, this meant that it only included soft scattering processes, i.e. processes where the transfer of transverse momentum is so low that one can not calculate their amplitudes from perturbative QCD. In FRITJOF 7.02 the validity of the model was extended up to RHIC and LHC energies by also treating hard processes. In each nucleon–nucleon collision the model first allows for a single hard scattering that is calculated according to perturbative QCD, and then the remnants of the original nucleon pair are treated as excited strings. Whether a scattering is perturbative or not is determined by the initially induced momentum transfer, which is in turn determined by the overlap of the color fields of the nucleons.

3.4.3 VENUS

VENUS[18], or *Very Energetic NUclear Scattering*, is another model based on the string picture. It is fundamentally different from the classical–string formation of FRITJOF, however, in that it is based on the Gribov–Regge equations for calculating cross–sections. Gribov–Regge theory is formulated within relativistic quantum theory, using entities known as Pomerons and Reggeons[7] — special ways of treating the partial wave expansion of the T–matrix elements[8] in h–h interactions that preserve unitarity — as elementary interactions. VENUS is therefore a fully quantized and relativistic model. Only once this formalism has been used to calculate squared amplitudes for the results of hadron–hadron collisions and a Monte Carlo procedure has been used to generate particles according to these amplitudes are they transformed into strings which are then hadronized using JETSET as for FRITJOF.

Another important assumption in VENUS is an eikonal formalism — in the expression for the scattering amplitude, the Pomeron propagator[9] is assumed to have a hard and a soft component. This hard component determines the contribution of minijets (see sec. 3.4.4) to the reactions and particle production, allowing for a natural way of differentiating between hard and soft processes.

VENUS was also used in the design of BRAHMS, both because it was a fundamentally different model from FRITJOF and because it has provided a very good description of the observed systematics at AGS and SPS energies. It has, however, not been much used lately for RHIC and LHC predictions, because its author has moved on to other models and has not included the latest developments in VENUS.

3.4.4 HIJING

HIJING[19], an acronym for *Heavy Ion Jet INteraction Generator*, is one of the more popular event generators on the market. It was written early in the 90's by M. Guylassy and X. N. Wang to explore the consequences of hard parton scatterings and assuming that the quark–gluon medium will influence the propagation of the scattered partons. Designed to work in the energy regime of RHIC and LHC, it has come heavily into focus over the last year as it closely predicts several of the features seen in early RHIC data.

For BRAHMS, HIJING has been an important event generator since the end of the first run, when it became clear that HIJING roughly predicted the number of produced particles in heavy ion collisions at $\sqrt{s} = 130GeV$. We then started using it as an input to GEANT to do for instance background subtractions in our analyses, and of course to compare our results to its various predictions.

[7] I refer the reader to [18] for a very good and instructive writeup of the gory details.

[8] See [2] for a description of scattering in relativistic field–theory

[9] Or, more precisely, the *Fourier transform* of the propagator.

Before this, we mostly used FRITJOF and VENUS in the development of our software and testing of our detectors.

The physics included in HIJING

The authors of HIJING write in the abstract to their long program writeup[25]:

Based on QCD–inspired models for multiple jet production, we developed a Monte Carlo program to study jet and the associated particle production in high energy pp, pA and AA collisions. The physics behind the program [...] includes multiple minijet production, soft excitations, nuclear shadowing of parton distribution functions and jet interactions in dense matter [...].

In the following, I'll give a brief overview of the meaning of this rather concise statement.

Jets, hard and soft scatterings

One of the first essential features of HIJING is that it treats both hard and soft scatterings between partons[10]. Its treatment of the two is fundamentally different, and they are tied together into a total cross–section for nucleus–nucleus interaction via an eikonal function

$$\chi(b,s) = \frac{1}{2}\sigma_{soft}(s)T_N(b,s) + \frac{1}{2}\sigma_{jet}(s)T_N(b,s) \tag{3.20}$$

where $T_N(b,s)$ is again the nuclear overlap function and s is the center–of–mass energy. HIJING uses a three-parameter Woods–Saxon potential to calculate this.

A hard scattering is defined as a collision between two partons with a momentum transfer high enough that it is calculable in pQCD. A cutoff–parameter of $P_0 = 2$ GeV/c is introduced, marking the boundary between the hard and soft regimes. All parton scatterings of transverse momentum larger than P_0 are treated as hard, perturbative processes that each lead to a jet.

A jet is what results when one parton is knocked out of a participating nucleon and subsequently hadronizes. Very high E_T jets are individually reconstructible by summing the transverse mass seen in one shower of reaction products, but as E_T diminishes to below roughly 5 GeV they loose their identity and blend into the continuum of produced particles — socalled minijets. The assumption that some fraction of the parton–parton scatterings evolve this way still has important implications for the physical observables, shown to lead to correlations in multiplicity, strangeness, transverse momentum and fluctuations competing with expected signatures for a QGP. At RHIC, theoretical predictions for the fraction of p_T produced by minijets are of the order of 50%, and for LHC the number is as high as 80%. [26]

[10] Partons here include both valence– and seaquarks and gluons.

Soft interactions, not calculable in pQCD, are treated in a phenomenological way via a multiple string approach. The model lets multiple soft gluon exchanges between valence quarks lead to longitudinal string–like excitations, which then hadronize according to the JETSET fragmentation scheme[24, 23]. Soft gluon radiation is also allowed for these strings before fragmentation. The cross–section for such soft processes

$$\sigma_{soft}(s) = 57mb \tag{3.21}$$

is taken as a parameter in the model, chosen to fit experimental data and kept constant (independent of s).

Parton production

A central assumption in HIJING is that an AA collision initially can be decomposed into a number of binary nucleon–nucleon collisions. The number of such collisions at a given impact parameter is calculated via the Glauber model, and the ineracting partons (hard) or wounded nucleons (soft) are treated as excited strings in the beam direction. The main phenomenology is taken from the Lund string model[27]. For each such binary collision an eikonal formalism is used to determine the kind of interaction that occurs, its momentum transfer and the number of jets produced. Unlike FRITJOF, HIJING allows the excited strings to de–excite via subsequent interactions, treated like ordinary nucleon–nucleon collisions. The possibility that a single parton suffers multiple scatterings of high enough momentum transfer to be considered hard is seen as negligible and not included in the model, though several or all partons in a nucleon may suffer individual hard scatterings.

The cross–section for jet production in HIJING is modified by assuming an effect known as nuclear shadowing. This is based on the observation[28] that the effective number of quarks in a nucleus is reduced as seen by partons carrying small fractions of the nucleon momentum, or small values of the Bjorken fraction x_{Bj}. The observational evidence for this effect is yet limited, and even more so for the related phenomenon of gluon shadowing, but HIJING includes both of these using a theoretical parameterization given in [29]. The effect of nuclear shadowing is to modify the quark structure functions and in turn change the effective jet production cross section in binary nucleon–nucleon collisions. This basically means that there will be fewer partons avaliable for binary collisions.

The third essential physical assumption made in HIJING is that of jet quenching. It has been observed that if a state of dense nuclear matter with free color charge is indeed formed it may have a spatial extent of up to R_A, and jets with high p_T will have to traverse a length of this medium before reaching the outside. HIJING models this by assuming an average energy loss dE/dz for the partons traversing the medium in the transverse direction, interpreted as

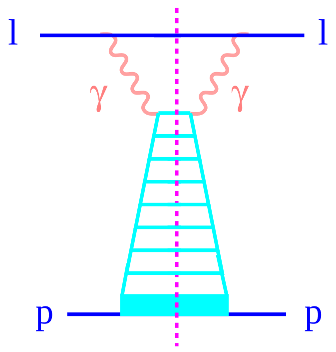

Figure 3.7: Deep inelastic lepton–proton scattering via a parton ladder. From [20].

induced gluon radiation. Interaction points are calculated by a simple mean–free-path assumption

$$dP = \frac{dl}{\lambda_s} e^{-l/\lambda_s} \tag{3.22}$$

where λ_s is the mean–free–path and l is the length traveled in the medium.

3.4.5 neXus

neXus[20] is one of the newest competitive models, only a few years old. It deserves mention because it is fundamentally different from the others in that it bases itself on the *universality hypothesis*. This states that the behavior of high energy interactions is universal, to that e.g. the hadronization of partons in nuclear interactions follows the same rules as the one in electron–positron annihilation. neXus expects the basic structure of nucleus–nucleus collisions to be elementary interactions between individual nucleons, realized via parton ladders (see fig. 3.7). The model also allows the same nucleon to participate in several interactions. This kind of framework creates interactions that are in principle calculable in perturbative QCD, but in practice the amount of tunable evolution parameters, couplings, cut–offs etc. make the theoretical uncertainties as great here as for all other models. Still, the universality approach is attractive if nothing else then for its internal consistency.

While neXus has only done a moderately good job of predicting the early systematics seen in the published RHIC data[30], details of the further performance of this relatively new approach is eagerly awaited.

3.4.6 UrQMD

UrQMD[21], which stands for *Ultrarelativistic Quantum Molecular Dynamics*, is a particular realization of the more general Quantum Molecular Dynamics (QMD) approach to calculating the outcome of heavy–ion collisions. QMD tries to treat the complex nucleus–nucleus system through proper quantum field theory, constructing a coherent state equation for each nucleon and relating them via a Lagrangian. Proper scattering theory is then used to calculate the outcome of collisions.

UrQMD is an extension of this approach to the ultrarelativistic energy regime. The projectile and target are treated as Fermi–gases of Gaussian–shaped density distributions (nucleons), for which equations of motion are calculated. A collision occurs if the distance between their centroids is smaller than some parameter related to the experimentally known cross–section, and if so a full QCD scattering calculation is carried out. 55 baryon and 32 meson species and resonances are included as final states in the scattering matrices, with cross–sections fitted to $p-p$ or $\pi-p$ data, and can be populated via string decays, s–channel collisions or resonance decays.

Also, this field–theoretic calculation is not cut off e.g. after the first interaction like in many other models, but allows for a thorough study of the later evolution of the system on an event–by–event basis. This makes the UrQMD approach very interesting, since new data clearly show the need to go beyond first–collision models and treat rescattering properly. [7]

3.4.7 EKRT

The EKRT model, so–named because of its makers Eskola, Kajantie, Ruuskanen and Touminen, was first proposed in [22] and recently expanded in [31]. It starts out with a standard pQCD computation[32] using standard parton distribution functions and nuclear effects[33, 34], and then makes the assumption that the particle production is reduced relative to a pure $p-p$ scaling because of QCD saturation.

Saturation occurs when the total geometric cross–section for minijet production from all the involved partons equals the transverse size of the nucleus, i.e. a saturation of the quark and gluon phase spaces:

$$N_{AA}(p_0, \sqrt{s}) \cdot \frac{\pi}{p_0^2} = \pi R_A^2 \tag{3.23}$$

Here, $p_0 \gg \Lambda_{QCD}$ is the transverse momentum scale, R_A is the nuclear radius and N_{AA} is the number of minijets produced into the central unit of rapidity for a collision of impact parameter $b = 0$. The conjecture is that if one can find the scale p_{sat} at which this happens, the amount of transverse energy produced at this scale is a good approximation of the total E_T produced in the reaction.

Numerical solutions to the equation above give estimates of this scale for different $\sqrt{s}$ energies, and having determined this the model uses a Glauber approach to select centrality and then assumes a hydrodynamical expansion of the fireball. Their Equation–of–State is taken from [35]. Details on their hadronization scheme has not yet been published, but it is essentially based on two– and three–body decays of hadron resonances.

This approach has so far lead to predictions of particle production and transverse flow effects at RHIC and LHC energies. At RHIC this approach is probably only valid for the most central events since it requires $p_0 \gg \Lambda_{QCD}$, but there its predictions are very close to the recently published $dN/d\eta$ values from PHOBOS[36] and PHENIX[37] and also to the ones I will show in chapter 8.

3.5 QGP signatures and current experimental status

The issue of whether or not a Quark–Gluon Plasma can actually be formed in nature is not yet settled. Most or all researchers in the field now agree that partonic degrees of freedom must be taken into account when describing high–energy collisions, but the term QGP involves more than this. Both a phase–transition from confined to deconfined matter and a complete thermalization of the QCD plasma are required before we can announce the discovery of a Quark–Gluon Plasma.

In addition, we have no simple way of checking the QGP hypothesis. A heavy–ion collision is over within a few $fm/c = 10^{-23}s$, so we need clear predictions on the effects of a QGP on the produced hadron spectra and other final–state observables and good experimental results to test them against. Unfortunately, since we also don't know the other reaction mechanisms at work in high–density nuclear matter or their relative significance the different models have huge theoretical uncertainties and almost all are capable of producing the same observables given enough parameter–tweaking.

Still, some experimental probes have survived as probable signals of QGP formation. I'll give a brief review of some of them, focusing on areas where there has been recent experimental progress[11]. Unless otherwise stated the information in this section is from [7], an excellent review of this subject by Bass, Guylassy, Stöcker and Greiner, and I refer the reader there for the gory details of QGP signatures.

[11] As of the QuarkMatter 2001 conference in Stony Brook, N.Y., Jan. 2001

3.5.1 Strangeness production

In a nucleus–nucleus collision the initial state is composed of gluons and a number of u and d quarks, and importantly no strange valence quarks. All net strangeness content of the reaction products must therefore have come from processes associated with the collision.

If a deconfined quark–gluon plasma is formed, an $s\bar{s}$ pair may be formed via $q\bar{q}$ annihilation, via interactions of two gluons or the thermal decay of a gluon. At the temperatures and densities where we expect a plasma to form the two latter are assumed to be fast processes because of the density of gluons. We get a high $s\bar{s}$ production, since the estimated critical temperature $T_C \approx 170 - 190MeV$ is of the same order as the strange quark mass ($m_s \approx 150 - 180MeV$). Hyperons[12] can then form at the hadronization stage simply by an s or $\bar{s}$ being close to other quarks in phase space (quark coalescence).

In a hadronic scenario on the other hand, where all color charge must be confined at all times, there are many factors that suppress strangeness production. Multistrange baryons will require multiple collision steps to form. Baryon number must also be conserved, so any antihyperon produced must see the simultaneous production of another baryon or vice–versa, or hyperons can be produced from existing baryons through hadronic collisions. The energy required to produce a $\Lambda\bar{\Lambda}$ pair is e.g. $2m_\Lambda \approx 2.2GeV$, i.e. an order of magnitude above T_C. On average, it will take a much longer time to produce a hyperon in this scenario than in a deconfined state and energy thresholds will be higher.

This leads to the prediction of an enhanced production of all hyperons if a deconfined state is reached, increasing with the strangeness content of the baryon. In particular, enhancement of antibaryon production ($\bar{\Lambda}$, $\bar{\Xi}$, $\bar{\Omega}$) is predicted to be a very strong signal. (See e.g. [38].)

Strangeness enhancement has been measured by many collaborations over the last years, both at the AGS and the SPS. A very interesting plot produced by the WA97/NA57 collaborations[13] is shown in fig. 3.8. It plots the net enhancement of strangeness production relative to $p - Be$ collisions versus the number of wounded, or participating, nucleons, proportional to the system size. It shows that at SPS energies there is an enhancement relative to data from $p - Be$ collisions, roughly proportional to the strangeness content of the baryon. By dividing out the dependency on the system size (number of participating nucleons) the data strongly indicate a threshold behavior at lower N_{Part}, as would be expected from a phase transition.

The NA57 collaboration is in the process of measuring more points for lower N_{Part} — preliminary data can be found in [40].

[12] A *hyperon* is a hadron containing at least one s or $\bar{s}$ quark.

[13] Two consecutive and mostly overlapping collaborations using the same experimental setup and hardware.

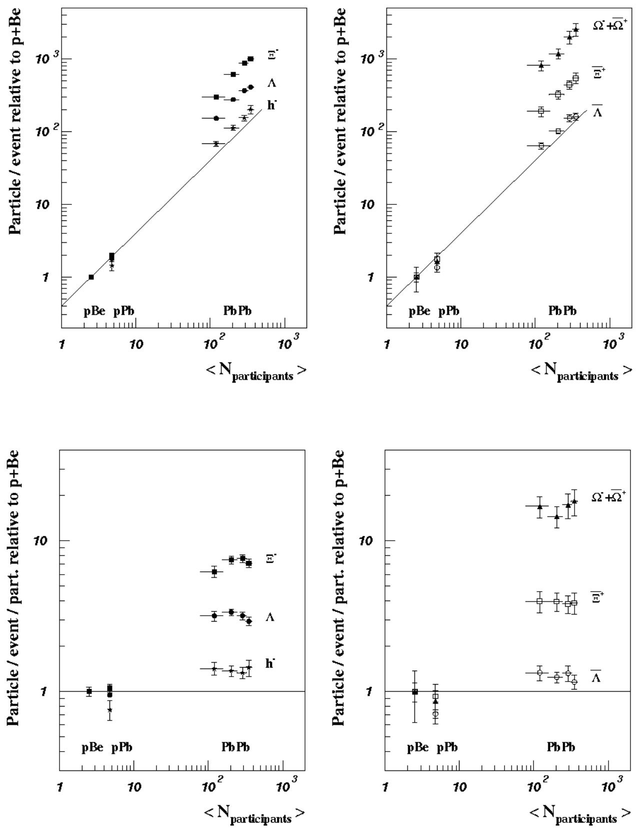

Figure 3.8: Strangeness production at SPS energies, measured by the WA97 collaboration.[39] The production is seen to be enhanced relative to $p - Be$ collisions (top) and also when the system size dependency is divided out (bottom).

3.5.2 J/ψ suppression

The production rate of charmonia, bound states of a c and a $\bar{c}$, is another predicted signal. It is related to the expectation of *color screening* in a deconfined QGP, a process analog to Debye screening in an electromagnetic plasma.

The interaction potential between two quarks can be written as[11]

$$V(r) = \sigma r - \frac{\alpha}{r} \tag{3.24}$$

where σ is the string tension responsible for confinement. The total energy of a $q\bar{q}$ system is then

$$E(r) = 2m + \frac{1}{2mr^2} + V(r) \tag{3.25}$$

and differentiating this expression one can find the bound states of the system, and their binding radii.

In a deconfined plasma $\sigma \to 0$ (deconfinement) and color charge will be screened by the surrounding, strongly coupling medium. The $q\bar{q}$ interaction then becomes

$$V(r) \to -\frac{\alpha}{r} e^{\frac{r}{r_D}} \tag{3.26}$$

where r_D is the *Debye radius* of deconfined QCD matter - the radius beyond which screening takes place. Plugging this into the equation for total energy we get a new spectrum of possible bound states and radii.

Inserting numerical values for the particle J/ψ ($c\bar{c}$) shows that for all reasonable values of the coupling constant α_s we get $r_{J/\psi} > r_D$, meaning that the c and $\bar{c}$ will be screened from each other and consequently cannot form a bound state. This leads us to expect a decline in the production rate of J/ψs if deconfined matter is formed.

To be able to use this signal one necessarily needs to know all possible production and decay mechanisms for the J/ψ extremely well, so that one can predict what number of particles one should observe due to "normal" hadronic processes. One can then plot the observed cross–section for J/ψ production divided by the expected one and check for any deviation.

The NA50 collaboration has studied this signal extensively at the SPS, and has very recently presented its results[41] — see figure 3.9. The solid line shows the expected production cross section divided by the Drell-Yan background contribution, and the points show an observed cross–section well below this value, the suppression increasing as a function of total transverse energy. In [41], they interpret the structure of this graph as the consecutive "melting" of the χ_c resonance (an excited $c\bar{c}$ system) at $E_T \approx 30 GeV$ and the more tightly bound J/ψ at $E_T \approx 90 GeV$, possibly indicating deconfined behavior. Though this interpretation is not yet fully accepted, the NA50 data are a very good indication that we have indeed formed a deconfined state of matter at SPS energies.

3.5.3 Direct signals

The postulated dense QCD matter of a fireball is a strongly interacting environment, meaning that everything that couples to color charge will have a very short mean–free–path. All hadronic signals that reach our detectors will probably have undergone multiple scatterings and so lost the information they held about the original collision, with the exception of conserved quantities like strangeness and entropy.

But this does not apply to electromagnetic probes — photons and leptons, which only interact via the electroweak couplings. If we could measure γs and leptons coming straight from the fireball we will get direct information on the conditions during early stages of the collision, and possibly a measure of its thermal radiation.

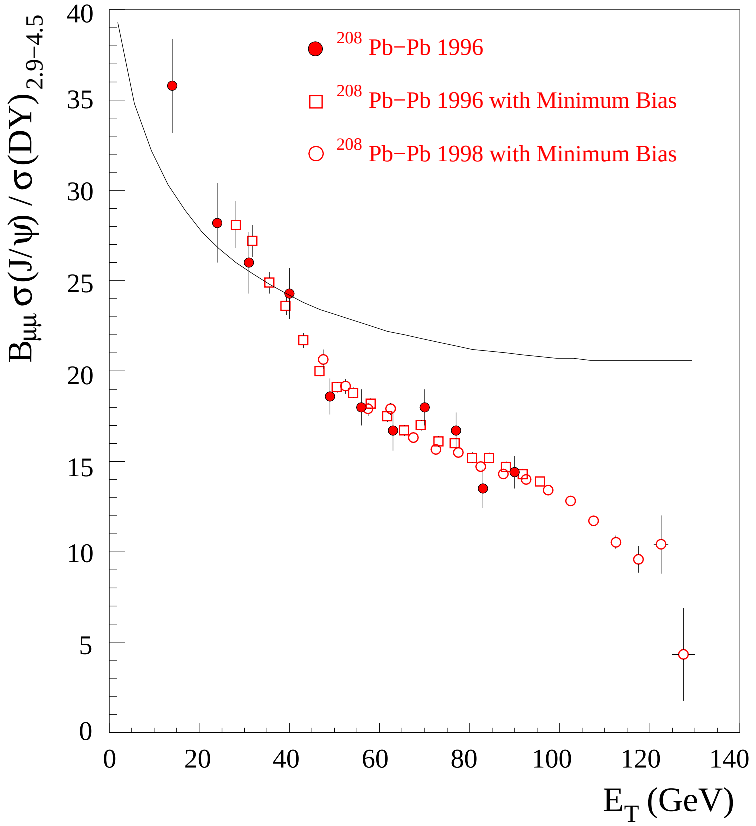

Figure 3.9: The expected hadronic production cross–section of J/ψ production divided by the Drell–Yan background (solid line), and data points by NA50[41]. The results show a clear suppression of the production rate of J/ψs for higher E_T.

Direct photons have two major production channels — $q\bar{q} \to \gamma\gamma$ and $qg \to q\gamma$ (or $\bar{q}g \to \bar{q}\gamma$), while lepton pairs are mainly produced in quark–antiquark annihilations $q\bar{q} \to l^+l^-$ or from the leptonic decays of fast–produced mesons.

The main idea behind the leptonic decay signal is that both due to possible in–medium effects and the possibility of chiral symmetry restoration in the plasma, the masses of the hadrons may change. One might e.g. see a double–peak in the invariant mass spectrum of a meson, indicating a long–lived mixed phase. Particularly the ρ mass is interesting, because it lies in an energy range where the background processes may not completely dominate. Background is a serious problem for this leptonic signal and there is still doubt about whether it can be measured at all, but for masses around $1-1.5GeV$ ($m_\rho = 769MeV$) there is at least a possibility to "outshine" the products of later hadronic decays, bremsstrahlung etc.

Many experiments have been designed to look for direct signals, and only

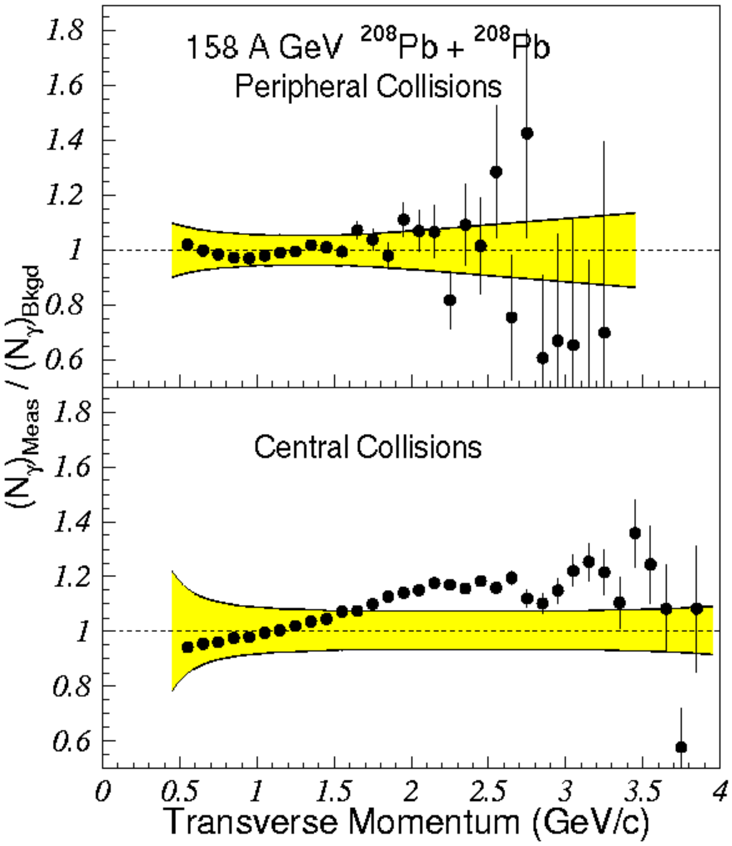

Figure 3.10: An excess of produced photons in central $Pb-Pb$ collisions at $158AGeV$, seen by the WA98 collaboration. Presented at QM2001 [43].

very lately have there been any results. At Quark Matter 2001 [42] the WA98 collaboration from CERN presented their latest figures (see figure 3.10), showing an excess of produced photons beyond the expected background, mostly coming from $\pi^0 \rightarrow \gamma\gamma$ decays, and also outside the estimated systematic errors. The excess is seen for central collisions and not for peripheral indicating that this may be related to a formed QGP, but rescatterings in a dense medium is also a possible explanation.

At any rate, the WA98 result shows the feasibility of measuring these difficult probes, and several experiments at higher energies (PHENIX@RHIC, ALICE@LHC) are planning to measure direct signals.

3.5.4 Other signals

Many other signals of a QCD phase transition have been predicted, and current experiments at the AGS, SPS and RHIC are working on detecting most of them.

Here is a quick list of other important signatures:

- **Baryon stopping.** The degree of stopping suffered by the colliding nucleons is sometimes considered a QGP probe, even though it gives no direct information about a plasma formation. It does, however, tell us what kind of system we are seeing the decaying remnants of, something which is imperative for the correct interpretation of most or all of the other proposed signals. See extended discussions on baryon stopping in sections 3.3.2 and 8.10.

- **Particle spectra.** The production rate of different particle species and their respective p and E_T distributions can tell us much about the reaction dynamics of the fireball, and whether or not we achieve kinetic equilibration.

- **Flow.** The flow, or current, of momentum in different directions out of the reaction zone is closely linked to the pressure in the fireball and thus to the Equation–of–State. For a first order phase transition the pressure will remain constant during a phase coexistence period, leading to a vanishing or strong reduction of the speed of sound in the medium. Known as a *softening* of the EoS, this may lead to a strong decrease in transverse flow for semi–peripheral collisions. Plotting the flow $< p_x >$ versus the beam energy should therefore give us information about this signature.

- **Source size.** Hanbury–Brown–Twiss (HBT) interferometry is a technique originally used to measure the transverse size of stars. By measuring the probability of detecting two photons in coincidence in two detectors, one can find a correlation to the radial size of the photon emitter. This can be extended to heavy–ion collisions, where we instead measure identical hadrons like pions or kaons. This can be used to measure the size of the emitting volume, i.e. the physical size of the reaction volume. The evolution of this observable with beam energy and system size may give us information about a possible QGP formation.

- **Strangelets and exotic matter.** The standard model does not forbid particles with a baryon number $|B| > 1$, but no such particle has ever been seen. An example of a particle which is being sought is the H_2 dibaryon, consisting of the quarks $uuddss$. The formation of such a particle is very heavily suppressed in a hadronic scenario, but may perhaps be formed in a deconfined state. Also, it is predicted that a system composed of u, d and s quarks may be more stable than "normal" ud matter — socalled *strange quark matter*. Such a configuration might arise from the freeze–out of deconfined matter, and should leave visible signatures. Both of these more exotic possibilities are being sought at todays experiments, but so far the search has been without result.

3.6 How we currently view a heavy–ion collision

Based on the above I can now briefly summarize what we *believe* occurs in an ultra–relativistic heavy–ion collision. See figure 3.11 for an illustration.

1. Two nuclei collide head–on ($b \approx 0$)

2. At the SPS energies there is still a significant fraction of incident baryons in the fireball (Landau picture), while at RHIC and LHC energies we approach the baryon–free Bjorken limit. The incoming partons undergo a mix of hard and soft scatterings, the first producing a minijet (high p_T) plasma and the second also contributing heavily to the transverse momentum production. Saturation effects may reduce the transverse energy produced. In any case, the excited QCD matter may or may not reinteract and have time to thermalize — the issue is not settled.

3. The fireball starts expanding, though not as explosively as once thought. Hadronization begins at the phase boundary.

4. At some stage, chiral symmetry is broken. This symmetry, which is proposed to exist between left– and right–handed fermions at higher energies, was restored in the initial collision and may cause observable effects when it is rebroken. [2]

5. The plasma hadronizes and continues to expand. It first undergoes chemical freezeout, meaning that the final state hadron ratios are reached, and then reaches thermal freezeout meaning that all the particles stop interacting and both particle species and momenta are "frozen".

This simplistic view, summarized by Hans Specht at Quark Matter 2001, is probably very incomplete and naive but it serves as a basic understanding for building and testing better models and experiments in this very exciting but difficult field. To quote Kristoffer Gjøtterud, a theorist at the University of Oslo:

"It is better to be wrong than to have no idea."

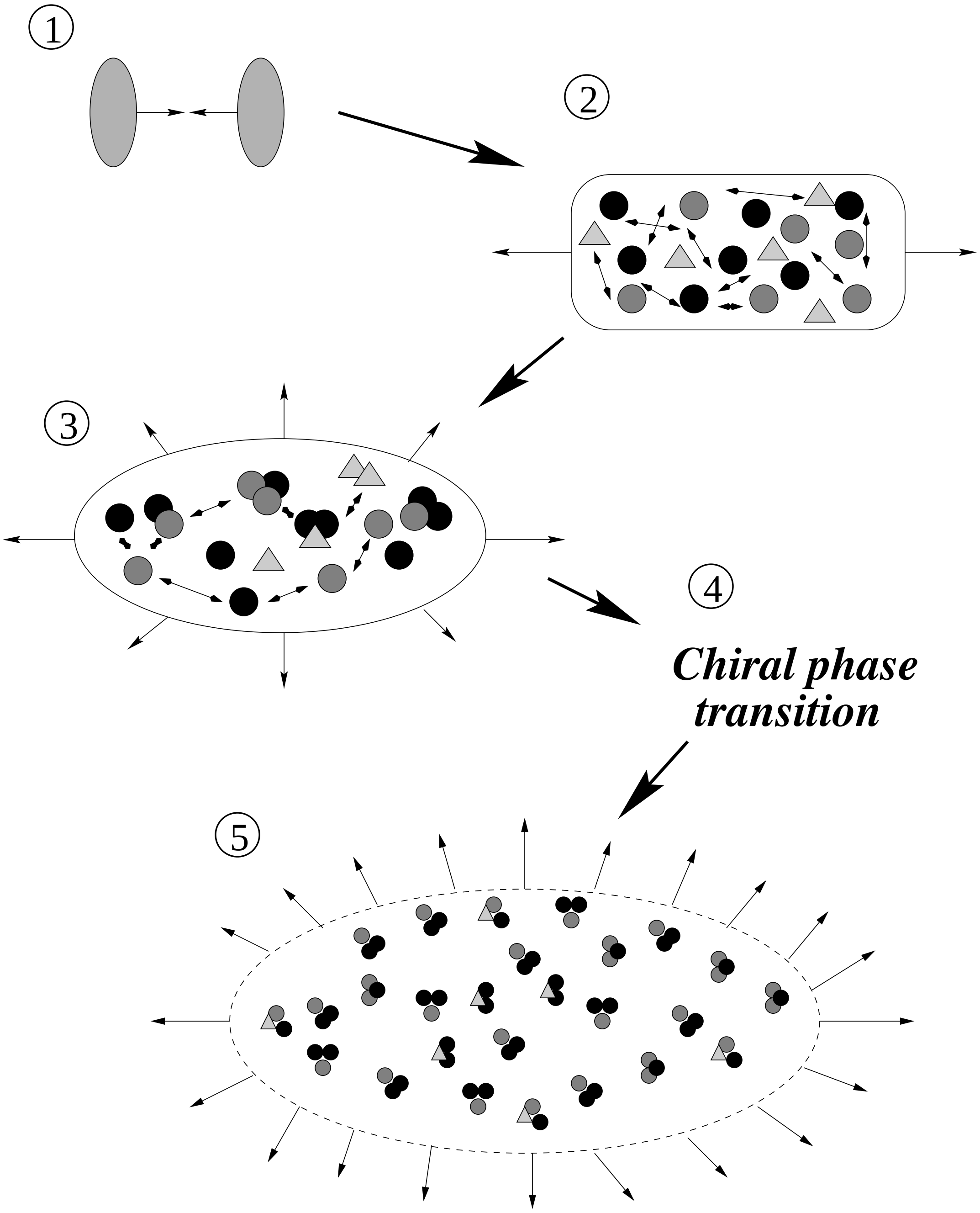

Figure 3.11: A schematic view of a heavy–ion collision. (1) A central collision between two nuclei. (2) The formation of deconfined quark matter. (3) Early expansion of the fireball, including hadronization a the phase boundary. (4) Chiral phase transition — the breaking of the symmetry between left– and right–handed fermions.[2] (5) Expansion of the fireball, now completely hadronized and re–confined. (This figure is inspired by Hans Spechts summary talk at QM2001. [44])

Chapter 4

RHIC and the BRAHMS experiment

In the summer of 2000 the first physics–run with the RHIC accelerator at Brookhaven National Laboratories (BNL) on Long Island, New York, started. RHIC, or *Relativistic Heavy Ion Collider*, then became the most powerful nucleus–nucleus collider ever built and will continue to be so until the LHC starts running in 2005/2006.

My work has been with the BRAHMS collaboration, which runs one of the four experiments at RHIC. This chapter will present the BRAHMS detector in detail, but first I'll briefly present RHIC itself. At the end of the chapter I also include a brief description of the other three experiments — STAR, PHENIX and PHOBOS.

4.1 RHIC

In the early 1980's BNL planned to build a $p-p$ collider named ISABELLE, and construction was well underway in 1983 when the project was suddenly dropped for political reasons. That left BNL with a 3.8 km long tunnel and some other infrastructure, unusable for anything else.

This quickly spawned different plans for other facilities that could make use of the existing construction, and eventually a proposal to build a heavy ion collider was accepted by the American Department of Energy. This project became RHIC, an accelerator capable of colliding all nuclear species from p to Au, and with a maximum center–of–mass energy for the heaviest ions of $\sqrt{s} = 200AGeV$[1] It can also collide asymmetric systems (e.g. $p-Au$ or $Cu-Au$), and do studies of collisions between polarized protons. A full scan of the nuclear phase space available at RHIC is expected to give detailed, continuous

[1] The notation $AGeV$ means GeV per nucleon.

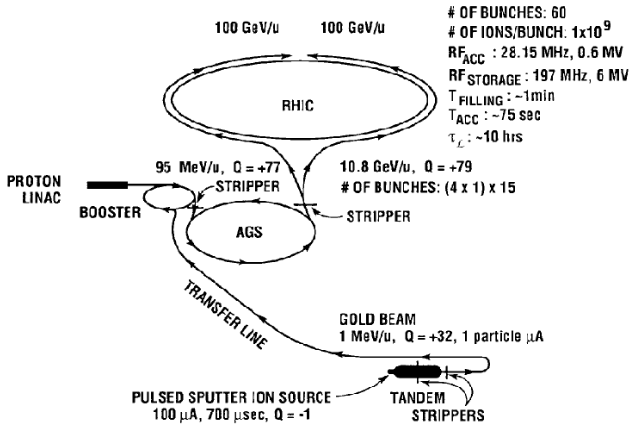

Figure 4.1: The BNL accelerator complex, including RHIC. [45]

information from the new high–energy regimes and down into the regions well–explored at AGS and SPS.

RHIC [45] utilizes most of the BNL accelerator facilities (see fig 4.1) to achieve the highest possible energies. For gold and other heavy nuclei, the first stage is acceleration through the existing Tandem Van der Graaf. They pass through a stripping foil, and typically exit this machine with a charge of $+12e$ and an energy of $1AMeV$. Then, after another stripping bringing them to $+32e$, they enter the Booster synchrotron where they are further accelerated to 95 $AMeV$. Yet another stripping follows, this time to $+77e$, and the ions are transfered into the AGS ring. This accelerates them up to its maximum energy of $10.8AGeV$, after which they are sent through a final stripper removing the last two electrons, and the now $+79e$ ions finally enter the RHIC ring.

Since RHIC is a collider, it has two separate rings known as *yellow* and *blue*. The ion beam is split into these two rings, and when the RHIC rings are fully injected[2] the superconducting magnets around the ring accelerate the beams up to their final energy.

The beams intersect in six regions around the ring, known as the *interaction regions*. Four of these are instrumented with the BRAHMS, PHOBOS, PHENIX and STAR detectors, and with RHICs design luminosity of

$$L_{Design}^{Au-Au} = \sim 2 \cdot 10^{26} cm^{-2} s^{-1} \tag{4.1}$$

for $Au - Au$ at $\sqrt{s} = 200AGeV$ each experiment should see collisions at around 200Hz.

[2] All the way from the Tandem Van der Graaf and up to RHIC, particles are accelerated in bunches. The initial bunches are merged along the route into bigger bunches, and in the end RHIC can take up to 60 bunches in each ring, each with an ion content of $\sim 10^9$.

4.2 BRAHMS - an overview

BRAHMS[46], or *Broad RAnge Hadron Magnetic Spectrometer*, is one of the two smaller experiments at RHIC. It is run by a collaboration of roughly 50 scientists from 10 institutions in the U.S. and Europe — see appendix D for details.

The main physics goal of the BRAHMS experiment is to measure inclusive and semi–inclusive charged hadron spectra over a wide range of rapidities and momenta. The detector, shown in figure 4.2, has a small solid angle coverage but consists of two separate arms that can be turned to cover

$$2.3^o < \theta_{FS} < 30^o \Leftrightarrow 1.3 < \eta_{FS} < 3.9 \tag{4.2}$$

$$30^o < \theta_{MRS} < 95^o \Leftrightarrow -0.1 < \eta_{MRS} < 1.3 \tag{4.3}$$

The two arms are the central part of the experiment, and give tracking information via time–projection chambers and multiwire drift chambers, and particle identification from a combination of bending through magnets and time–of–flight systems. We also have two Čherenkov counters. The quite different physics predicted at forward– and midrapidities lead naturally to different detector requirements in the two regions, and this has been the main motivation in the design of the detector.

The full integrated acceptance of BRAHMS can resolve $p^{\pm}$, $\pi^{\pm}$ and $K^{\pm}$ in the pseudorapidity range $0 \leq \eta \leq 4$, with transverse momenta up to 2.2 GeV/c (currently) at midrapidity and momenta up to 25 GeV/c at forward rapidities (see fig. 4.3). We also hope to measure Λs [47] and deuterons. This wide acceptance in both η and p_T is where BRAHMS has its strength over the other three RHIC experiments.

In addition to the spectrometer arms, BRAHMS has an array of global detectors that measure particle multiplicities, cross sections, event centrality and interaction points. One of these, the Zero Degree Calorimeter, is a detector common to all the four RHIC experiments that allows for easy comparisons between experimental results from the different collaborations.

4.3 The magnets

Since BRAHMS is a spectrometer, relying on tracking and momentum determination for precise particle identification, our magnets are very important. There are five magnets in BRAHMS, labeled D1 through D5 in figure 4.2. They are all dipoles, made mainly of iron and with copper conductor and epoxy/glass insulated coils. Their nominal maximum mid–gap field is 12 kG, enough to bend particles of up to 25 GeV/c through the whole forward arm.

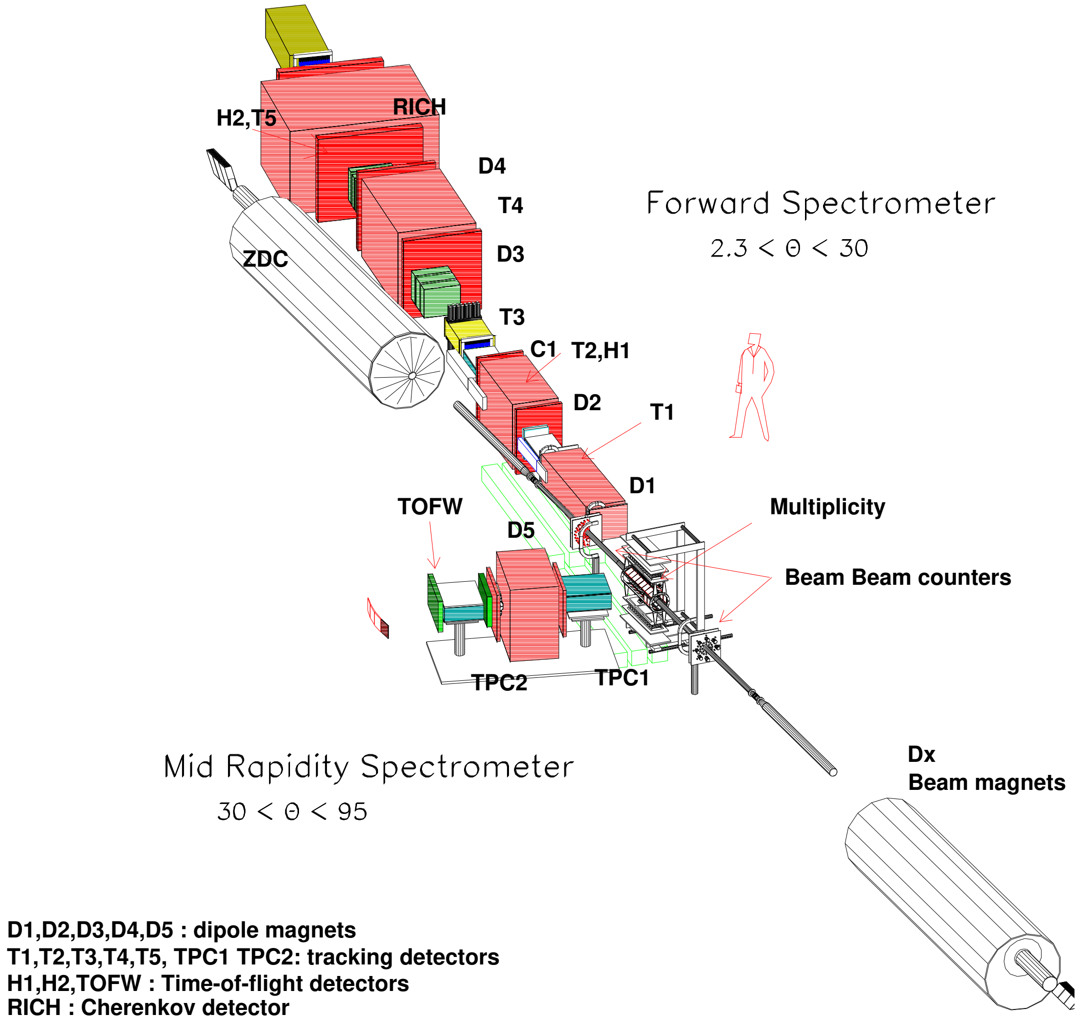

Figure 4.2: The BRAHMS detector. The detectors TPC1 and TPC2 will in the rest of the text be denoted TPM1 and TPM2.

The magnets have been modeled with the packages POISSON (part of the CernLIB package) and TOSCA (commercial software available from Vector Fields, see www.vectorfields.com) to investigate e.g. fringe fields and the effect of the magnet positions on the RHIC beam. The latter is seen to be roughly 7 G with the magnet at full current (see fig. 4.4), and this effect has to be compensated for by the main RHIC magnets when the front spectrometer is set at low angles.

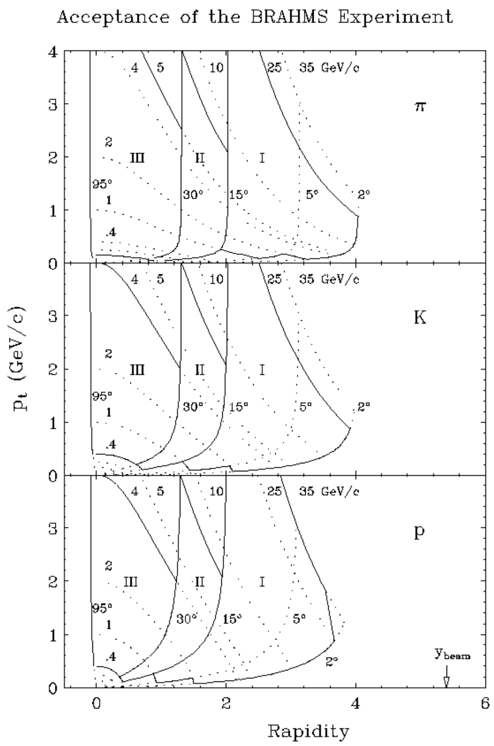

Figure 4.3: The acceptance of the BRAHMS spectrometer for p, K and π. Region I is the full forward spectrometer arm, II is the front forward spectrometer and III is the midrapidity arm.

4.4 The forward arm

The *forward spectrometer arm* (FS) is an array of separate detectors roughly 20 m in length. See figure 4.2 for detector names and details. Because of the layout of the detector and the size of the BRAHMS interaction hall, the FS is subdivided into two shorter components, the front– and back–forward spectrometers (FFS and BFS) mounted on separate platforms to allow independent rotation. The main reason for this is to further extend our acceptance towards lower transverse momenta and higher pseudorapidities. Using only the FFS is therefore denoted *low momentum mode*, while employing the BFS is called *high momentum mode*.

4.4.1 FFS

The FFS begins with the D1 magnet. The particles then pass through the time projection chamber T1, get bent again in the D2 magnet and then pass another TPC, T2. See section 6.2 for TPC details. This triple–system of tracking —

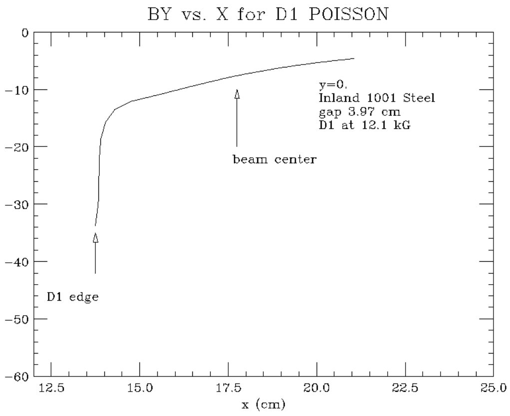

Figure 4.4: 2-D POISSON simulation of the fringe field of the D1 magnet. x is the distance from the magnet center.

bending — tracking gives the momentum of the particle, and a "swim–back" routine through D1 combined with information about the vertex (see chapter 7) tells us whether it is a primary particle or not. After T2 the particles pass a time–of–flight wall (H1) giving time–of–flight information, and a Čherenkov counter (C1) for particle identification.

H1 is made of 40 scintillating staves of about $1 \times 1 \times 25\ cm^3$, connected to fast photomultipliers at each end. They can read out both time and pulse height information, giving time–of–flight with picosecond resolution. See table 4.1 for details.

C1 is a segmented threshold Čherenkov counter using C_4F_{10} gas at 1 atm. pressure, and is expected to extend our pion identification up to 9 GeV/c. It is mounted on a movable platform, and is removed when the FS is used in high momentum mode.

An important part of the design considerations for a spectrometer is the particle multiplicities it will be expected to handle. GEANT simulations of $Au - Au$ collisions at $200GeV$ based on FRITJOF and VENUS (see chapter 2) have shown that T1 might have to handle up to 0.2 $particles/cm^2$ and T2 up to 0.05 $particles/cm^2$, and this has been incorporated into their design. Both TPCs have a two–particle resolution of less than 1 cm. The data from the first year of RHIC running have shown even lower multiplicities than expected (see e.g. my $dN/d\eta$ analysis in chapter 8), so T1 and T2 are not expected to have problems with too high occupancy.

Name	Distance from nominal vertex	Species separated	Maximum p (GeV/c) 3σ cut	Nominal time resolution
H1	9m	π/K	3.8	75 ps
		K/p	6.5	
H2	20m	π/K	5.8	75 ps
		K/p	9.7	
TOFW	4m	π/K	2.5	75 ps
		K/p	4.3	

Table 4.1: The BRAHMS time–of–flight systems. The time resolution achieved during year one is 120 ps.

4.4.2 BFS

With the spectrometer in high momentum mode, C1 is removed and the particles continue down the arm. They pass two more magnets, D3 and D4, and three drift chambers (DCs), named T3, T4 and T5. (Again, see fig. 4.2 for details.) After the last DC, there is another hodoscope (H2) for time–of–flight information, and a ring–imaging Čherenkov detector (RICH) for maximum particle species resolution.

The BRAHMS drift chambers are all identical segmented multiwire proportional chambers. [48] They each consist of three separate modules, again divided into several wire planes. The different planes have wires in both the horizontal and vertical directions, and in the two 45^o–tilt directions, giving a track position resolution down to $\sim$ 200-250 μm. The DCs were installed during the 2000 run, and commissioning and software development are currently in their final stages. They are expected to be fully operational for the year 2001 running period. [49]

H2 is made of 20 scintillating staves of about $1 \times 2 \times 40$ cm^3, again connected to fast photomultipliers at each end. See the description of H1 above, and table 4.1 for details.

The RICH is what gives us particle–identification up to very high momenta. It is designed to separate π/K up to 20 GeV/c and K/p up to 30 GeV/c. Like all detectors of this type, it uses a mirror system to focus the Čherenkov light from a particle onto a detector plane and the size of the ring is used to identify the particle species. It was commissioned during the 2000 RHIC running, and we were able both to see rings and do rough PID with it. See figure 4.5 for an example. More precise RICH data will come in year two of RHIC running.

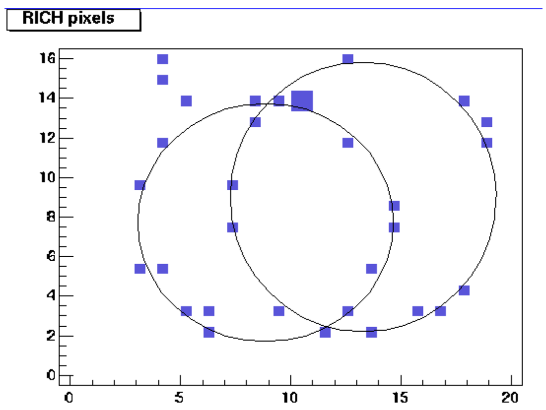

Figure 4.5: Rings seen in the RHIC detector. From an internal BRAHMS analysis note by Ramiro Debbe. [50]

4.5 The midrapidity arm

The BRAHMS midrapidity arm (MRS) can cover the angles $30^o \leq \theta \leq 95^o$ and is in design quite like the FFS except that it does not start with a magnet. The particles enter the time projection chamber TPM1, pass through the D5 magnet, the TPC TPM2 and end up in a time–of–flight wall (TOFW). Refer to tables 6.1 and 4.1 for details. The BRAHMS conceptual design report ([46]) also contains plans for a Čherenkov counter after the TOFW for better PID, but this plan was dropped for financial reasons. We still hope to implement this detector at a later stage, and are currently considering temporarily adding an older Čherenkov from the CERN-experiment NA44 to improve our species separation at midrapidity.

TPM1 is an important piece of the BRAHMS detector. It is our only tracking–device positioned before any magnetic field, so in addition to giving essential tracklets for the entire MRS, it also serves as a a $dN/d\eta$ detector, an estimator for the amount of background produced e.g. by the beampipe, and it is our most accurate vertex detector. I have done work on all of these points, and they will be discussed extensively in chapters 7 and 8.

GEANT studies indicated a probable upper limit of 0.3 $particles/cm^2$ for TPM1 at its most forward setting, and less than 0.01 $particles/cm^2$ for TPM2. This has contributed both to the design of the TPCs and their physical positioning in the BRAHMS hall.

Unfortunately, during year one data taking TPM1 was quite noisy. This was mostly due to diverse design and operating errors, and for year two the entire readout–plane of the detector will be rebuilt. This noise has made doing physics with TPM1 somewhat harder than necessary in this first year, and the results presented later on in this thesis will reflect this. TPM2 is in design very much like TPM1, but has worked very well during the first year.

The TOFW, when fully instrumented, will be a 160 m wide array of 22 cm high scintillating slats instrumented similarly to H1 and H2. During year 1 only the left part (as seen from the nominal vertex) was instrumented, and the rest will be put in place for year 2. Like the hodoscopes, it has been designed to give a timing–resolution better than $\sigma = 75ps$. During year one, it achieved a resolution of $\sigma = 120ps$.

4.6 The global detectors

While the spectrometer arms provide detailed track information for lengths of up to 20 meters, they need to be augmented by detectors that measure more global characteristics of an event. These include the centrality of each collision, the total cross–section seen by our detectors, the charged particle multiplicities and not least the start time for reading out our detector electronics. We have four separate global detector systems — Beam–Beam counters (BB), Zero–Degree Calorimeters (ZDC), a multiplicity tile array (TMA) and an array of silicon strip detectors (SMA). Again, please refer to figure 4.2.

4.6.1 BB

Our Beam-Beam Counters are two arrays of small and large tubes made of Čherenkov–radiating material and connected to photomultiplier tubes. They are designed to detect $\beta = 1$ charged particles[3], and are positioned around the beampipe at ±2.25 m from the nominal vertex so that they sample the region

$$3.0 \leq \eta_{BB} \leq 4.5 \tag{4.4}$$

If the vertex moves away from $z = 0$ this range can be extended to $\eta \sim 2.2$. The geometry of the left and right arrays differ slightly due to the space required by the FS — see figure 4.6.

During year one we have had some small problems with some of the small tubes saturating[4], but for the last part of the run they worked very well.

Our most used collision trigger[5] is defined as registered hits in two specific large BB tubes in each array within a narrow time interval ($\Delta t < 5ns$). In addition the BBs give primary vertex information from timing (see section 7.1.2), centrality information and sample the $dN/d\eta$ distribution at high η.

[3] $\beta = (\frac{v}{c})$

[4] A photomultiplier tube is said to saturate when its readout goes to the maximum. Any increase in the signal sent to the tube will then not be registered, and we lose information.

[5] The term *trigger* means a condition for starting the electronics readout, and therefore gives the start–time in TOF measurements.

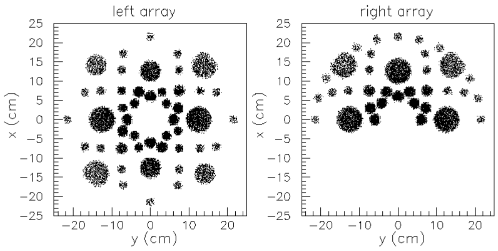

Figure 4.6: The BRAHMS BB arrays. The points are particles from GEANT simulations hitting the active detector volumes.

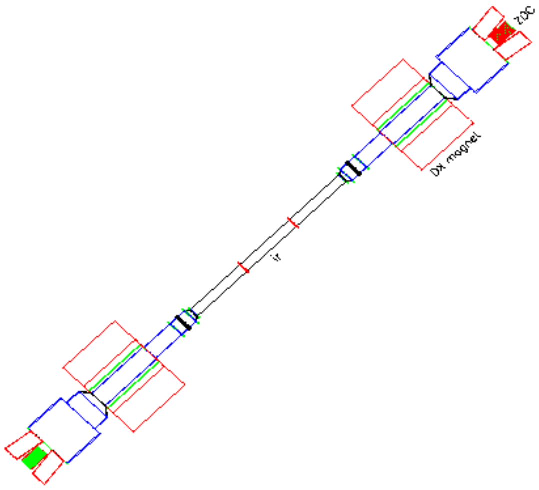

Figure 4.7: The positioning of the BRAHMS ZDCs, behind the DX magnets.

4.6.2 ZDC

The BRAHMS Zero–Degree Calorimeters are positioned ± 18 meters from the nominal vertex, behind the big DX magnets that combine and split the beams on each side of the interaction hall. See figure 4.7. The only particles reaching this far are straight–moving neutral particles, so the ZDCs are essentially devices for measuring energy deposited by spectator neutrons — i.e. neutrons that did not partake in the collision.

The energy deposited in the ZDCs is strongly correlated with the impact parameter, and this detector can therefore be used to complement the centrality detectors. E.g. the CERN–experiment NA49 has successfully used this technique [51].

Technically our ZDCs are divided in three sub–modules, each made of 29 layers of 5 mm tungsten and 0.5 mm PMMA Čherenkov radiating fiber to sample the hadronic shower. Each module is again connected to a photomultiplier tube

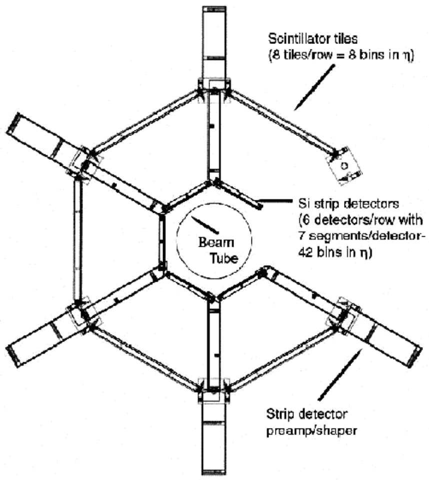

Figure 4.8: A cross–section of the BRAHMS multiplicity barrel, showing both the silicon strip detectors (SMA) and the plastic scintillator tiles (TMA).

for readout of the signal.

The main uses of the ZDCs, apart from centrality measurements, are rather similar to the BBs. They give information about the vertex position from timing (see section 7.1.2) and can also be used as a collision trigger by requiring a hit in both the left– and right ZDC within some time interval ($\Delta t < 18ns$ for year one).

As mentioned above, a final very important feature of the ZDCs at RHIC is that they are the same for all four experiments, allowing for very easy comparison of event selection and centrality cuts, cross–section and luminosity measurements between the collaborations.

4.6.3 Multiplicity barrel

The last important piece of detector hardware is the multiplicity barrel positioned around the beam–pipe. A cross–section is shown in figure 4.8. The mult array is a two–layer construction with the inner part consisting of silicon strip detectors (SMA, or Silicon Multiplicity Array) and the outer part of plastic scintillator tiles (TMA, or Tile Multiplicity Array).

As indicated by its name, the main purpose of this detector element is to give a measurement of the event centrality by measuring the multiplicity of produced particles. Also, for events close to the nominal vertex ($|z|<20$cm), the array covers several units of pseudorapidity and is therefore able to give a good $dN/d\eta$ measurement, resolving the detailed shape of the distribution. Its coverage in this area is complementary to that of the BB, and overlapping with that of TPM1 giving a good cross–check of our charged particle multipliticy measurement. (See chapter 8.)

An consideration when introducing any kind of material this close to the beam is the generation of secondary tracks in the spectrometer because of collisions with either the supports or with the detectors themselves. This possible contribution is included in our GEANT studies, and to minimize both the noise contribution and the decay rate due to interactions with material before the spectrometer arms, the mult barrel is not instrumented in the area directly between them and the beam.

The mult array was mostly instrumented during year one, and the two arrays are producing consistent results on multiplicity and centrality (see sec. 8.2.1).

4.7 The other RHIC experiments

To give a more complete picture of the physics that will be covered at RHIC, I give below a brief description of the design and goals of the other three experiments.

4.7.1 PHOBOS

PHOBOS, named simply for one of Mars' moons, is the other small RHIC experiment. In size it is essentially table–top, consisting mainly of two arms of silicon strip detectors and a vertex detector in a homogeneous magnetic field, plus two multiplicity detectors (*paddle counters*) at high rapidities. See figure 4.9. Its emphasis is on measuring low p_T charged hadrons *and* leptons at selected solid angles.

The PHOBOS collaboration published the first physics paper based on RHIC results — a $dN/d\eta$ measurement. See ref. [36].

4.7.2 PHENIX

PHENIX is a large, essentially 4π detector consisting mainly of two large muon detectors in an inhomogeneous magnetic field. See figure 4.10. Its focus is on rare processes, taking detailed event–by–event data from collisions selected by a complex triggering system. One of its unique research goals is to study the possible formation of a *disoriented chiral condensate.*

The PHENIX collaboration has also published a paper on $dN/d\eta$ from the first year RHIC data, and very recently submitted a preprint on transverse energy production — see refs. [37, 53].

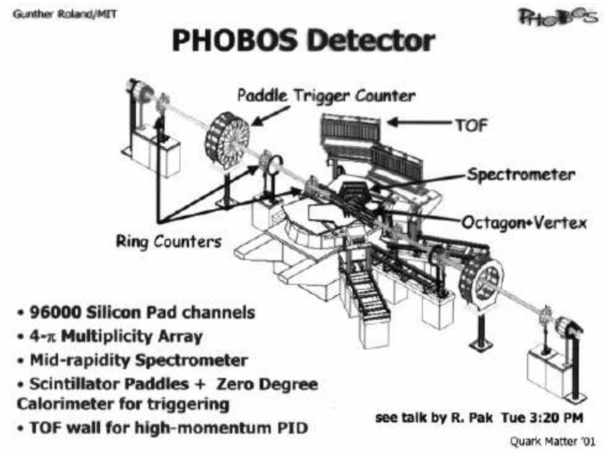

Figure 4.9: The PHOBOS detector ([52])

4.7.3 STAR

STAR is also a very large detector. Its main component is a very large barrel TPC in a homogeneous magnetic field, giving very good detailed event–by–event information about particle ratios, flow, fluctuations etc. in a limited η range around midrapitidy. To extend their η coverage, STAR will install additional forward TPCs during 2001.

STARs main physics emphasis is on the systematics and correlations of these observables. (See fig. 4.11.) This detector is also interesting because its design is very similar to that of the ALICE experiment under construction for the LHC at CERN. The success of the STAR collaboration gives hope that ALICE will also produce good, fast results when it comes on–line in 2006.

STAR has published a paper on elliptic flow based on the first year RHIC data, and also submitted a paper on the $\bar{p}$–to–p ratio at midrapidity — see refs. [55, 56].

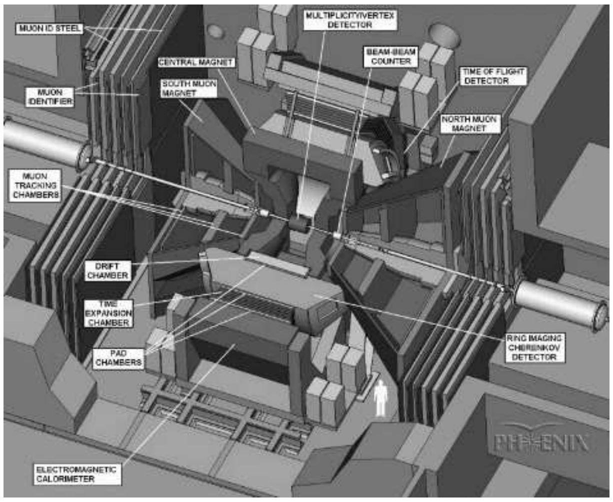

Figure 4.10: The PHENIX detector ([54])

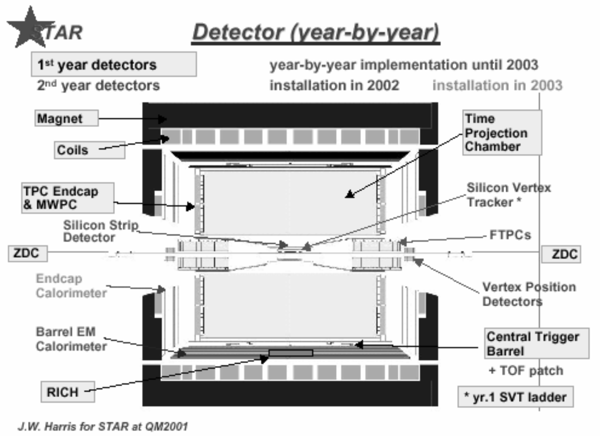

Figure 4.11: The STAR detector ([57])

Chapter 5

Software

This chapter gives a brief description of the diverse pieces of software relevant to this thesis — the simulation package GEANT, the high–energy physics class library ROOT, and our own ever–changing toolkit BRAT.

5.1 Event generators

Event generators, described in detail in section 3.4, are not only the link between our experimental data and testing of theory, but also indespensible tools in the design and testing of heavy ion experiments. The output from different event generators tell us roughly what particle densities we must design our detectors to handle, where in momentum and rapidity space we should place the detectors to best observe interesting physics etc.

The main output from an event generator is usually an array of particles and associated momentum vectors, frozen just after the collision is completed. To relate this output to an experimental setup, we need more software.

5.2 Geant

GEANT 3.21, part of the CERNLIB package freely available from CERN, is a tool in use by most of the heavy ion community. It simulates the interactions of elementary and composite particles with matter, and in particular the response of particle detectors to being hit by a particular particle with a given momentum.

The input to GEANT is either a starting point and momentum vector of a specific particle, or the output from an event generator detailing all produced particles from a collision. The given particles are then propagated through a description of an entire experimental setup which as closely as possible matches the true physical detector with respect to geometry and materials. The simulated output is stored as hit positions and associated energy deposits in the sensitive parts of the detectors, and in most cases an additional "slow simulation" mimicking the detectors response to these deposits must then be used to produce the same digitized output as from real data. (See e.g. [58].) This output can in turn be fed to the analysis tools used by experimenters, to produce predictions of the number of particles we expect to see per collision, the acceptance of our detectors and physical predictions like ratios of produced particles etc.

Often, this procedure is our only way of correcting experimental data for background from secondary particles or the effect of nearby dense material like magnets or detector stands. The combination of GEANT and the event generators is therefore a tool both for making predictions from theories, designing experiments, writing analysis software and understanding the output of detectors during real data taking.

BRAHMS has its own version of GEANT called GBRAHMS, where the parameters of our detectors are stored. This tool has been in use since the design stage of the BRAHMS experiment and is still widely used now for calculating our acceptance and the background contamination in our data. I used GBRAHMS in the development of the vertex classes presented in chapter 7, and I will use its output to test my results on charged particle production in chapter 8 against the HIJING model. I also use it to check the validity of some of the corrections imposed on my data.

5.3 ROOT

The ROOT package, written by Rene Brun and Fons Rademakers from CERN, is a C++ class library containing basic tools for handling and analyzing data — reading and writing data–objects from files, storing event–information in more accessible ways and displaying data in the form of histograms, scatter–plots etc.

ROOT has become the accepted replacement for the older package PAW, written in FORTRAN. PAW is still widely in use by older experiments since they do not want to (and should not) rewrite their software, but most younger experiments now use the ROOT package as a base toolkit for their own data analysis software. This includes BRAHMS, which has ROOT as the basis for our BRAT package — see next section. In its later versions, though, ROOT has grown beyond a simple "PAW for C++" into a much more ambitious project including tools for creating Graphical User Interfaces (GUIs) on many platforms, parallel processing, interacting with LaTeX for producing well typeset outputs, drawing Feynman diagrams, interacting with database packages like MySQL etc. ROOT is becoming a very flexible and also very reliable software package for uses ranging well beyond high energy experiments.

Like GEANT, ROOT can be freely obtained from the CERN web pages. Precompiled versions exits for several platforms, including Linux, Windows and even iPAQ pocket PCs! See appendix B for information on how to get and install ROOT.

5.4 BRAT

BRAT, the *Brahms Reconstruction and Analysis Toolkit*, is a collection of C++ classes and application packages for dealing with detectors and data in BRAHMS. This package contains most of our essential software, so any and all physics output from BRAHMS is computed in the BRAT framework. BRAT is based on the ROOT class library described above and so has all of its functionality, but is also contains its own interfaces to our Data Acquisition System (DAQ) and parameter and calibration databases written in MySQL.

The official BRAT version is kept in the BRAHMS CVS (Concurrent Version System) repository at BNL. See appendix B for information on how to download and compile BRAT.

The classes in BRAT are in theory divided into four categories: [1]

- *Data classes* that simply contain data and ways of getting and setting this information. This group contains all our Rdo classes, Dig classes, Geometry classes and Calibration classes. Examples: **BrVertex**, **BrRdoZDC**, **BrRdoTileCalibration**.

- *Modules* are the classes that actually do the work in BRAT. They all (should) contain an *Event(Inputnode, Outputnode)* procedure, where data is passed to the module in th Inputnode and new data is placed in the Outputnode. Examples: **BrTrackFollowFinderModule**, **BrTPMClusterVertexModule**, **BrTileCentModule**.

- *Managers* are classes that ensure correct reading of parameter files, calibrations etc. They are singletons, meaning that only one manager object of each type is allowed to exist at one time. Of one already exists, the new pointer will latch onto the old class instead of making a new one. Examples: **BrParameterElementManager**, **BrAppOptionManager**, **BrGeometryDbManager**.

- *Utility classes* are the final group, consisting of classes that don't fit into the other categories. This may be geometry objects like vectors and lines, ways of storing and using mathematical algorithms etc. Examples: **BrVector3D**, **BrUnits**, **BrMath**.

A typical BRAT reconstruction or analysis program then proceeds as follows:

[1] Thanks to C. H. Christensen for sending me a clear writeup of the BRAT philosophy.

1. Instantiate some managers and pass them the correct data files.
2. Create some modules that will do the work, including an IO module to read data from disk.
3. Open a data file.
4. For each event in the data file, call the Event(Inputnode, Outputnode) procedure of all the modules, hooking the newly generated information onto **BrEventNode**s. This must be done in the correct sequence, e.g. first producing clusters from raw TPC sequences, then using these for tracking through the spectrometer and finally doing PID on the completed tracks.
5. Either write the data from each event to a new file, or analyze the produced data further and fill histograms etc.

As you can see, BRAT is a very modular toolkit and it is very easy to add new functionality by e.g. wrapping it in the form of a new module class.

5.5 Changes introduced in BRAT

As a BRAHMS collaborator working with software, I have made both heavy use of the existing BRAT code and introduced several modifications and new classes. Here, for reference, is a list of the major changes I have made:

- My main work has been with the *vtx* directory, which contains all the classes for reconstructing the collision vertex. This work is documented in chapter 7. Of the classes in this directory *BrTPMTrackVertexModule* was originally written by J. H. Lee but has been modified by me. The classes *BrTPMClusterVertexModule*, *BrVertexModule* and *BrVertex* are all written and introduced by me.
- I have written a modified version of the monitoring program *BrNtuple*, originally made by Alv Kjetil Holme, which includes an extra branch for calculating the vertex position from TPM1. The original BrNtuple can be found in the BRAT directory *online/ntuple*, but because of incompatibilities with some of the existing TPC classes I have not yet included my addition in the official BRAT code.
- In the *TPC* directory I have together with my supervisor, Trine Tveter, written the class *BrTrackStringFinder* which is a tracking algorithm for the four BRAHMS TPCs.

- In collaboration with Michael Murray and Andrei Makeev of Texas A&M University, I have also made changes in the *zdc* directory. I have helped include in BRAT the slewing corrections for the ZDC photomultiplier tubes, and also included this change in the program *BrNtuple*.

- Under *base*, I have added the class *BrValueObject*. This is a class intended for development only, giving the capability to store a single integer, float, double or boolean in the form of a **BrDataObject**.

  BrValueObject has been slightly controversial. The argument against the class is that its usefulness does not match its size, but since I have been told that several people have found it useful I have not removed it from the official BRAT distribution.

Chapter 6

The time–projection chamber

Most of the work presented in this thesis is centered around one BRAHMS subdetector, namely the first TPC in the midrapidity arm (TPM1). It is therefore necessary first to give a short intro to TPC technology, and I will at the same time present the ideas behind our track reconstruction software.

6.1 Basic TPC technology

A time–projection chamber, or TPC, is a detector designed to give both a high position resolution, three dimensional measurement of the trajectories of charged particles and a measurement of their individual ionization energy loss dE/dx. Sometimes known as the "electronic bubble–chamber", it is one of the most common types of tracking device in modern particle physics experiments because of its flexible abilities and low cost and complexity. Several very large experiments, e.g. STAR@RHIC and ALICE@LHC, are essentially one big cylindric TPC covering 4π azimuthally around the collision point (low η).

The basic TPC design ([48], [59]) begins with a box filled with a gas that is easily ionized by passing charged particles, but that is chemically inert. Mixtures of Ar and CO_2 or Ne and CH_4 are common choices. Inside the box is a homogeneous electric field, so that when electrons are liberated from the gas by passing particles they drift in this field to a specified side of the box that is covered by readout pads and strung with anode wires (the *padplane*). See illustration in figure 6.1. The liberated electrons collect on the anode wires, inducing a charge signal. A mirror charge is also induced on the closest pads. TPCs are operated at electric fields such that the field gradients close to the anode wires accelerate the electrons enough to trigger electromagnetic avalanches. This amplifies the collected signal in a way proportional to the originally liberated charge, allowing for a precise measurement of the energy loss dE/dx of the passing particle.

The anode and fieldwires in fig. 6.1 are used to maintain the electric field.

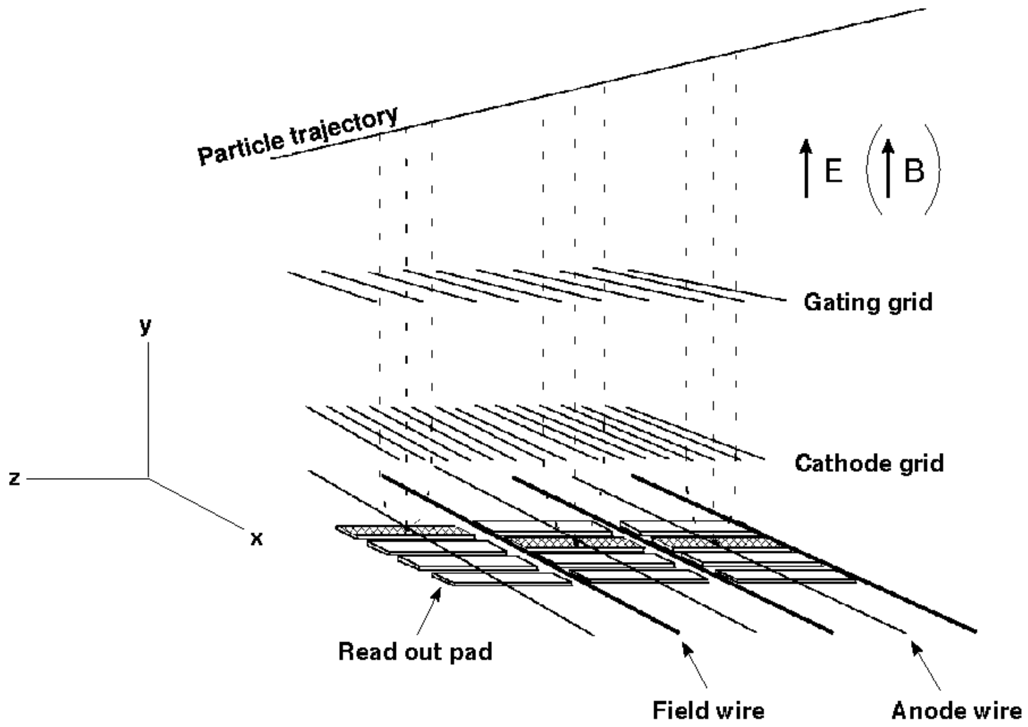

Figure 6.1: Schematic illustration of a TPC. Electrons are liberated from the chamber gas by passing charged particles, and drift in an electric field towards a plane of readout pads. A parallel magnetic field keep the charges from drifting too much in the transverse directions.

In addition, one usually creates a magnetic field parallel to the electric field, in order to keep the electrons spiraling around these lines as they drift towards the padplane. This reduces their drift in the transverse directions, allowing for longer drift distances without loss of position resolution.

The pads are where the main measurements of a TPC are read out. The readout process is started at some set time after the experimental trigger indicates that a collision has occurred, and at a series of specified times after this (timebins) the induced charge on each pad is read out as an ADC value. One such array of ADC values for a given pad is known as a *TPC sequence*.

Another important feature of a TPC is that the freed electrons traverse the gas at a roughly constant speed known as the *drift velocity*, usually on the order of $cm/\mu s$, and therefore knowing the time an electron hit a pad is equivalent to knowing how high above the padplane it was liberated. The two last coordinates are supplied by the position of the pad, and a three dimensional position can in principle be found for each ionization.

In practice a good deal more work has to be done on the raw data before they

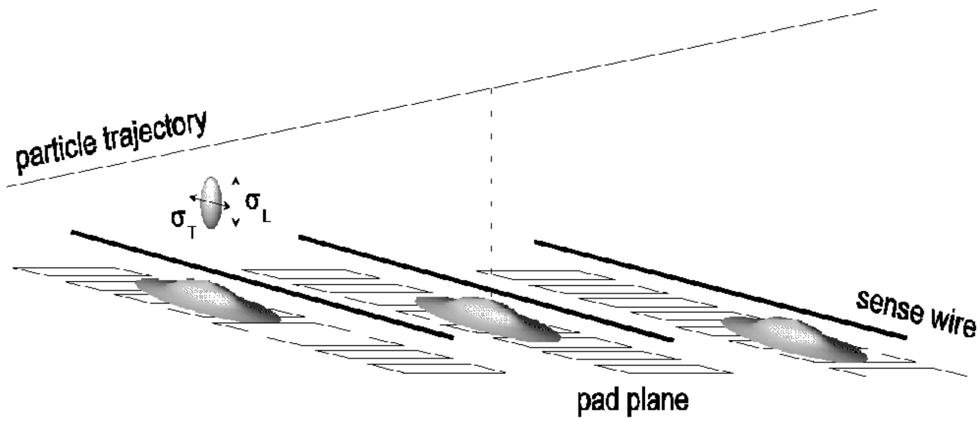

Figure 6.2: Charge smearing in a TPC. The charge from one avalanche will drift somewhat in the transverse directions and spread out over several pads. In the pad direction this distribution is fitted with the pad response function to give a precise position measurement.

can be used for trackfinding. Electronic noise and other non–physics effects are attempted removed and one has to compensate for the discrete and rather large size of the readout pads. Modern pads normally have a surface area around or below $1cm^2$, with a quadratic or rectangular shape. This is done by combining sequences into *clusters* or *hits*. A cluster is a combination of readouts overlapping in time and stretching over several pads in a row — see fig. 6.2. In the pad direction this distribution is fitted with a *pad response function* (PRF)[58] — the theoretical response of an anode wire to a point charge — folded with functions containing information about readout electronics, transverse diffusion velocities etc. In the time direction it is fitted with a *shaper response* (see [58]) folded with information on the expected longitudinal charge cloud distribution.

The result is approximately Gaussian, and the centroid of this distribution is taken as a measure of the position of the original ionization.

One last important piece of the TPC design, indicated in fig. 6.1, is the *gating grid*. This extra set of wires is included close to the anode wires to control the positive ions left by the freed electrons. When the gating grid is closed the drift field ends at the grid wires, preventing the ions from drifting into the active volume and distorting the field. The grid is opened to let electrons through only in some time interval after a valid collision trigger is set.

Name	Width (cm)	Height (cm)	Depth (cm)	Padrows	Pads/row
TPM1	38.40	20.00	36.60	12	96
TPM2	67.68	19.80	50.00	20	144
T1	33.60	19.80	56.00	14	96
T2	39.60	19.80	75.50	16	112

Table 6.1: The main parameters of the BRAHMS time projection chambers. The given size is the inner, active volume. In addition, they all flow a 90/10 $Ar - CO_2$-mixture.

6.2 The BRAHMS TPC design

The BRAHMS detector includes four TPCs, named T1, T2, TPM1 and TPM2 (see fig. 4.2 for an illustration of their sizes and positions). They are all of a basic "square–box" design, with parallel electric and internal magnetic fields and a single padplane. They are all positioned outside any external magnetic fields, so they will measure straight tracks. All the details in this section are from ref. [46].

6.2.1 General features

The sizes of the BRAHMS TPCs and their number of padrows and pads per row are given in table 6.1. They all flow a 90/10 % mixture of Ar/CO_2, and have drift distances of roughly $20cm$. The TPC boxes are made of plexi glass, and the entrance and exit windows are 25 μm mylar foils.

As mentioned in section 4.4 the TPCs have all been designed to give a two–particle separation of less than 1 cm, to cope with track densities of up to 0.2 $particles/cm^2$. The pads in all TPCs are 3 mm wide, and just below 3 cm long except for TPM2 where they are 2.4 cm. This is because that TPC will see the highest crossing angle of tracks and thus needs a better resolution also in direction away from the vertex.

Their nominal drift velocity is 1.3 — 2.0 $cm/\mu s$, so a time span of roughly 10 μs is needed to read out all the data from one collision.

6.2.2 TPM1

I wish to give a few special remarks about TPM1, the first TPC in the midrapidity arm. It is our only tracking detector placed before any magnetic field and therefore gives our only measurement of particle tracks leading straight back to the vertex. For this reason it is intended to perform as both a high–precision vertex detector and a multiplicity detector with the ability to separate primary from secondary tracks in addition to simply giving the first part of the complete midrapidity spectrometer tracks.

During year one of BRAHMS datataking, TPM1 did not function as well as hoped. It gave nice track resolution, but was also very noisy and would sometimes suffer enormous banana–shaped avalanches (internally known as "tsunami events") covering most or all of the TPC. This has caused problems for our trackfinding and vertexfinding software, mainly in increasing the CPU consumption of these algorithms because of the greater amount of data. Another problem has been that with so much data in the TPC our data–files become very large and take a long time to read and analyze. All the results presented in chapters 7 and 8 suffer from this effect.

To remove this problem, the entire readout–plane of TPM1 has been rebuilt for year two of RHIC running, and the anode– and field wires have been repositioned to better direct the incoming electrons. The number of anode wires is also increased. At the time of writing tests with cosmic rays have just been performed on the rebuilt chamber, and we now see clean tracks with no noise clusters. This hopefully means that for the next data–sets we can expect faster and cleaner reconstructions of TPM1, and an increase in the vertex precision and decrease in number of ghost tracks.

6.3 Clusterfinding

Clusterfinding in the BRAHMS TPCs is done via the BRAT class **BrTPC-ClusterFinder**. It is essentially an algorithm for reading through all the TPC sequences generated in an event, constructing islands in the pad vs. time plane — see fig. 6.3. The weighted average of each such island is calculated and taken as the centroid of the cluster, and together with the sample width, associated pad numbers etc. saved in the form of a **BrTPCCluster** object.

BrTPCClusterFinder also goes through all found clusters and tries to *deconvolute* so–called *multi–hit clusters*. If two tracks passed close to each other their associated peaks in the time versus pad plane may overlap somewhat, and this combined object should ideally be split into two separate clusters. This is a very difficult operation since it requires two well–separated maxima, but thanks to work by P. Christiansen, we are able to do a fairly good job of this. See [60] for a detailed description of the current BRAT deconvolution algorithm.

Finally, the clusters are converted to **BrDetectorHit**s, 3D points in TPC local coordinates. This is currently all the information that is passed to the track– and vertexfinder.

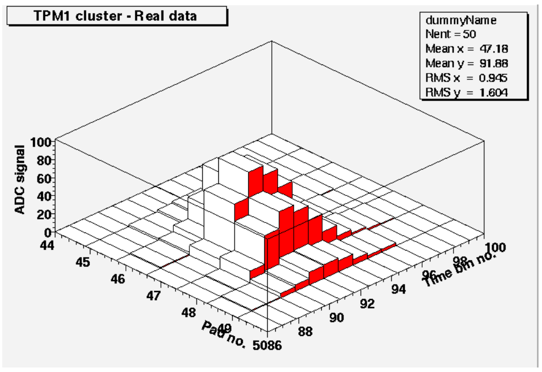

Figure 6.3: Raw data from a BRAHMS TPC. The plot shows the measured ADC value versus timebin and pad, and clearly shows a two–dimensional peak. This peak is fitted with a pad response function to form a cluster. Figure from [60].

6.4 Trackfinding

The located clusters represent a middle–step in the reconstruction, since what we really want is information on the exact trajectories that charged particles have followed through the TPC.

To make these trajectories, or tracks, we pass the clusters on to a tracking algorithm, or *tracker* for short. These are very basic pieces of pattern recognition software that look for straight lines in our three dimensional swarm of clusters.

In BRAHMS, we have two separate trackers known as **BrTrackFollowFinder** (TFF) and **BrTrackStringFinder** (TSF). The first one was originally written by F. Videbæk and has been greatly revised and improved by P. Christiansen. The second one is co–developed by myself and T. Tveter, as an alternative for events where the first runs into problems. I'll present the basic ideas behind both.

6.4.1 TrackFollowFinder

BrTrackFollowFinder, or TFF, is what is sometimes known as a "track snooper" or "follow your nose" algorithm. It finds a hit in the first padrow of a TPC and then looks within a predefined area on the next padrow (its *searchwidth*). If there is another hit within this area it goes on to the third padrow and so forth. See illustration in figure 6.4, which is a sketch of a TPC seen from the top. You can see one clear track where there is always a hit within the next search window, and a few noise clusters where the search window contains nothing. In cases where the search window contains more than

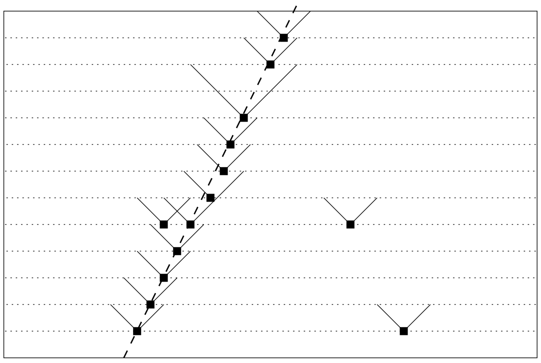

Figure 6.4: Illustration of **BrTrackFollowFinder**. Starting in the front of a TPC, it searches for a hit within a specified window in the next padrow. If it finds hits through the entire TPC, a track is made.

one hit, the track is "branched" into two track candidates sharing one or more hits, which are then treated as separate tracks.

After going through the entire dataset in this way, all instances where TFF was able to snoop through the entire TPC are fitted to straight lines and a **BrLocalTrack** object is created for each. This object retains memory of which clusters that created it, for easy calculation of goodness–of–fit tests etc.

As indicated in fig. 6.4, TFF also has the capability to skip a row where there for some reason is no hit and move on to the next, up until some setable number of rows are missed.

After completion of tracking, BRAT has a ghost–busting routine, located in **BrTrackFinderBase**, that checks to see if tracks have more than a certain number of clusters in common. If so, it keeps the one with the best straight–line fit (lowest χ^2) to its clusters. Track candidates with hits in too few padrows are discarded.

For tracks that pass this test, a **BrDetectorTrack** object is created, containing the original **BrLocalTrack** in addition to information on the χ^2 etc.

TFF performs very well, and is our primary tracker. We have measured its average tracking efficiency to be $\sim 95\%$ — see sec. 8.4.3. However for high–multiplicity events it until recently had a tendency to "give up" due to making too many "proto–tracks" before ghostbusting. This problem has now been fixed, but has for a long time been the main reason why we in some cases need another tracker.

6.4.2 TrackStringFinder

BrTrackStringFinder, or TSF, works on a completely different principle — see illustration in fig. 6.5. TSF combines all hits in a given number of front rows

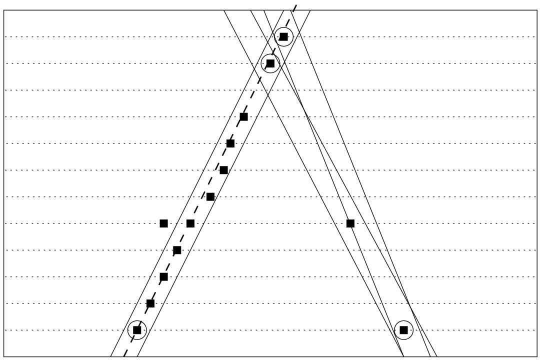

Figure 6.5: Illustration of **BrTrackStringFinder**. It combines hits in the front and back of a TPC with a cylinder, and checks whether enough padrows have hits within this area.

with all hits in the same number of back rows, and for each combination forms a straight cylinder between the two hits. Within this cylinder, of setable radius, it searches for hits and if it finds hits in more than some threshold number of padrows it creates a **BrDetectorTrack** for these hits.

Figure 6.5 shows the same dataset as for TFF. Now, one combination of hits produces a cylinder with many hits while two other combinations have at most three hits in total. TSF also has an internal ghostbusting routine for removing doubly found tracks, in addition to the one found in **BrTrackFinderBase**. TSF calculates the relative overlap between all tracks, and if this is above some cut value it removes the ones with the worst fit to its clusters. The advantage of this method over the common one is that it is not sensitive to "ghost clusters" — noise clusters or clusters that are erroneously split during deconvolution. A drawback is that it will also remove one out of a set of close–lying real tracks indiscriminately.

TSF has both a major advantage and a major drawback. The advantage is that unlike TFF it does not crash, but always produces a measurement of the number of tracks. Its drawback, though, is its speed. The CPU time needed by TSF goes as $N^2_{Clusters}$, and since there can sometimes be up to hundreds of clusters in the outer padrows and there is quite a lot of computing to do for each combination it is at times *very* slow. It takes on average between 10 and 20 times longer than TFF to reconstruct a datafile. This problem has been added to for the year one data by TPM1 being so noisy, effectively making TSF impossible to use for big analysis.

However, as mentioned above, up until recently TFF had a bad problem with "giving up" at high cluster multiplicities. For FFS tracking, especially in T1, this problem became insurmountable and in his recently published thesis [61] Claus E. Jørgensen uses TSF to produce $dN/d\eta$ from T1. This shows that with a little recoding and a less noisy TPC **BrTrackStringFinder** can provide us with a valuable double–check on our tracking–based physics.¨

Chapter 7

Vertex determination

An important prerequisite for most physics-measurements with a collider spectrometer like BRAHMS is knowing the *interaction point* or *vertex location*, the point in space where the two nuclei collide. This is not a trivial measurement, both since the collision necessarily occurs some distance away from the detectors and because in the direction of the beams the vertex can drift by up to several meters. On the other hand it is a very important measurement, necessary to determine track lengths, centrality calibrations, multiplicity corrections etc. For precise particle identification the uncertainty in the vertex position should be on the order of a few millimeters, so it also has to be very precise.

For year one of RHIC running, the vertex distribution (or *interaction diamond*) was very wide — see fig. 7.1. This will in any case reduce our data rate since some of the BRAHMS detectors require the primary vertex to lie within $\sim \pm 35cm$, and to minimize this problem we need a vertex determination that works well at least in this region.

Getting this measurement right with the detectors in BRAHMS has been a main part of my work. In this chapter I'll first present the three detectors in

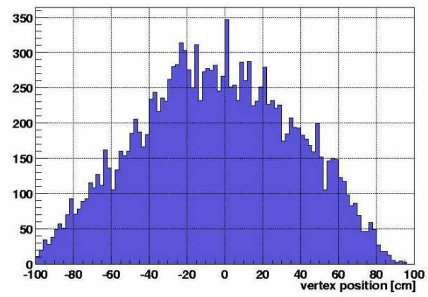

Figure 7.1: Full width of the vertex distribution in the beam direction during year 1, measured with the ZDCs.

BRAHMS capable of giving vertex information: BB, ZDC and TPM1.[1] Then I'll describe in detail the algorithms I have written for analyzing TPM1 data, document their performance and efficiencies on simulations and data, and show that they are correlated with the measurements from BB and ZDC.

The main results given in this chapter have also been presented in the poster *Interaction point determination in the BRAHMS experiment*, shown at the *Quark Matter 2001* conference.[42]

7.1 The BRAHMS vertex detectors

7.1.1 Zero–Degree Calorimeters

The Zero–Degree Calorimeters (ZDC — see section 4.6.2) can give information on the vertex z-coordinate from timing, since we know that the only thing that hits them are spectator neutrons moving at approximately the speed of light. By recording the times T_L and T_R when the energy deposited in the left and right calorimeters respectively goes over some threshold, the vertex z-coordinate can be calculated from the following formula:

$$z_{ZDC} = \frac{1}{2} \cdot (T_L - T_R) \cdot c + \Delta z_{ZDC} \tag{7.1}$$

where c is the speed of light and Δz_{ZDC} is an offset that must be determined from calibration (see below).

Since our ZDCs are basically blocks of Čherenkov radiating material connected to photo–multiplier tubes (PMTs), they suffer from a normal PMT problem — a constant rise–time. When energy is deposited in a PMT it always takes the same time for the induced signal to reach its maximum value. Therefore, when energy deposition is low and thus $Signal_{Max}$ is low, it takes a longer time for the ZDCs to reach their threshold value. This must be corrected for, a process known as a *slewing correction*. See illustration in figure 7.2.

Before slewing corrections, the timing resolution of our ZDCs has

$$\sigma_{ZDC}^{Uncorrected} \approx 9cm \tag{7.2}$$

The resolution is here determined by looking at the difference between z_{ZDC} and well determined vertices from TPM1 (see section 7.1.4).

After slewing corrections were done by Andrei Makeev from Texas A&M University, this resolution improved drastically:

$$\sigma_{ZDC}^{Corrected} \approx 3cm \tag{7.3}$$

[1]The Tile and Silicon multiplicity arrays are in principle also able to give vertex information. This capability is at the time of writing not included in BRAT, so I will not discuss it further.

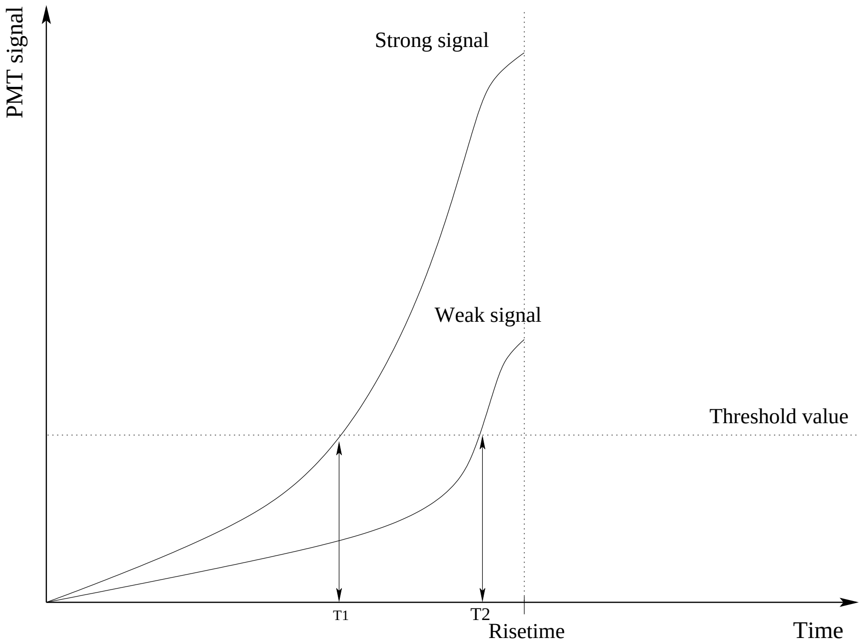

Figure 7.2: Schematic illustration of slewing corrections. A photomultiplier tube has a constant rise time, and a strong signal will therefore reach any set threshold voltage before a weak signal even if they start at the same time.

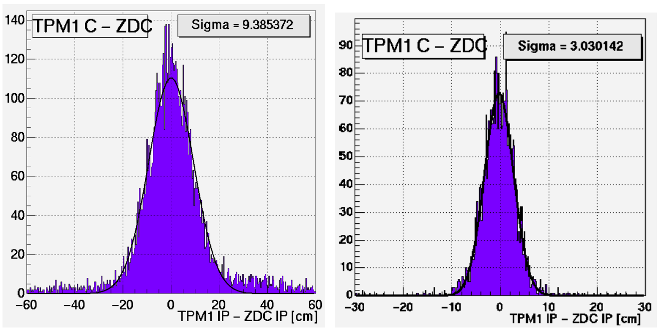

(a) Before (b) After

Figure 7.3: The vertex resolution of the ZDCs before (a) and after (b) slewing corrections.

See figure 7.3 for a comparison of the vertex resolution before and after the corrections were added. When calculating the global vertex in section 7.5, I input this value for all events to the weighted mean formula. The intrinsic timing resolution expected from the ZDCs is

$$\Delta t_{ZDC}^{intrinsic} \approx 115ps \Rightarrow \Delta z_{ZDC}^{intrinsic} \approx 3.5cm \tag{7.4}$$

so as figure 7.3 shows we are quite close to the expected ZDC performance.

The plot in figure 7.3 can also be used to determine Δz_{ZDC} in equation 7.1. Since z_{TPM1} is independent of timing the distribution of $z_{TPM1} - z_{ZDC}$ should be centered on $z = 0$ for correct Δz_{ZDC}, and so the mean of the Gaussian can be taken as a measurement of the offset. The reason there is an offset here at all, is that the cables between the physical location of the left and right ZDCs and the electronics readout point are not the same length. The signals therefore need different times to reach the DAQ.[2] In figure 7.4 I have plotted the ZDC resolution for four different runs taken on the same day, and the centroid is seen to drift with up to 25mm. This indicates that we may need to keep Δz_{ZDC} in our run database on a run–by–run basis to avoid any systematic errors in measurements based on ZDC timing. Since this problem has not been thoroughly investigated I'll ignore it in this thesis, and use the value

$$\Delta z_{ZDC} = 27.6cm \tag{7.5}$$

which I have measured to be the average offset over the runs that I will use in chapter 8. This value is also the current default value used in BRAT, introduced when I rewrote the BrRdoModuleZDC class.

7.1.2 Beam–Beam Counters

Our two arrays of Beam–Beam Counters (BB–see section 4.6.1) also give information on the vertex z–coordinate from timing. The principle is very similar to the ZDCs — we record the times when selected PMTs in the two arrays read out a signal above some threshold, and calculate the vertex z–coordinate from

$$z_{BB} = \frac{1}{2} \cdot (T_L - T_R) \cdot c + \Delta z_{BB} \tag{7.6}$$

The main differences from the ZDCs is the BBs much closer proximity to the nominal vertex, their sensitivity to participating or produced particles rather than spectator neutrons and their much better intrinsic time resolution:

$$\Delta t_{BB}^{intrinsic} \approx 70ps \Rightarrow \Delta z_{BB}^{intrinsic} \approx 2.1cm \tag{7.7}$$

[2] DAQ stands for *Data AQuisition*, and is the system that records all the data measured by our detectors.

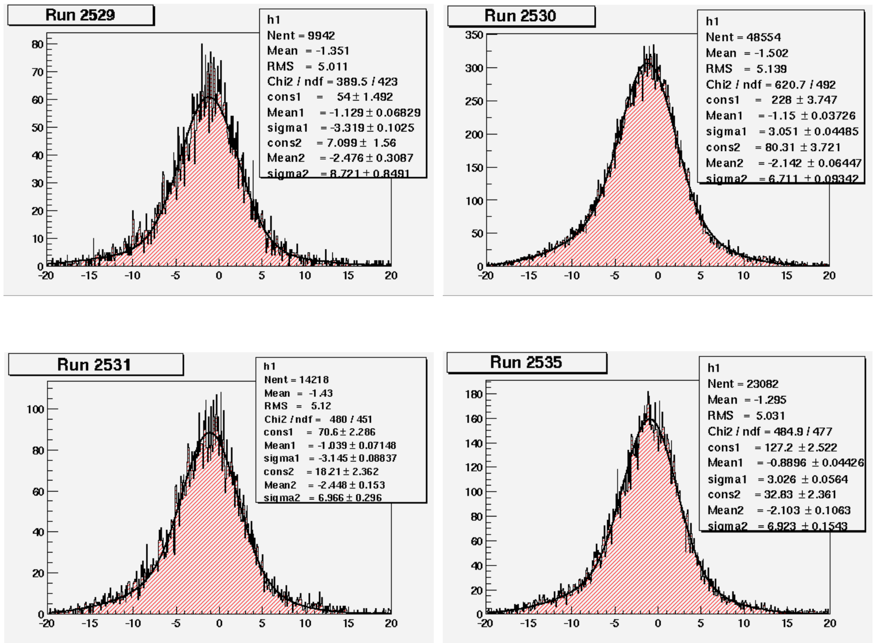

Figure 7.4: ZDC vertex resolution plots for four runs taken on the same day. As the centroid of the Gaussian shows, Δz_{ZDC} may drift somewhat with time.

They therefore give measurements for a slightly different (but mostly overlapping) set of events than what the ZDCs give, and should give vertex information with much better precision. Calibrations have been done for the BBs by Yury Blyakhman, BNL, and are incorporated in BRAT. Using the latest values of these calibrations, I find a vertex resolution of

$$\sigma_{BB}^{Corrected} \approx 2.6cm \tag{7.8}$$

(see figure 7.5), where again the resolution is defined as the width of the distribution of the difference between z_{BB} and z_{TPM1} for events with a well–fitted TPC vertex. Again, we are quite close to the expected vertex resolution.

The BBs may also have an offset Δz_{BB} e.g. from differences in the cable lengths that determine when the BB signals reach the DAQ, but this is taken care of in the calibrations included in BRAT. [3] I therefore assume in the rest of this thesis that

$$\Delta z_{BB} = 0cm \tag{7.9}$$

[3] The current BB calibration file can be found under /brat/params/bb/BrCalibrBB.dat

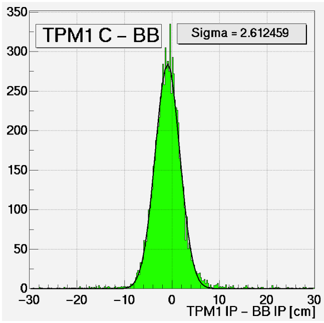

Figure 7.5: The vertex resolution of the BBs relative to well–determined TPC vertices

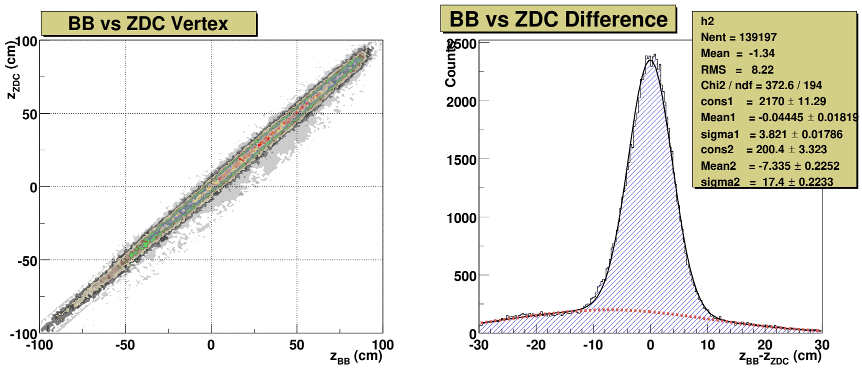

(a) Correlation (b) Difference

Figure 7.6: (a) The correlation between BB and ZDC vertices. (b) The difference between z_{BB} and z_{ZDC}, fit with a double–Gaussian.

7.1.3 Correlation between BB and ZDC

BB and ZDC give independent measurements of the vertex position, and so their results should be correlated. Figure 7.6 is a plot of BB vs ZDC vertex, showing that this is indeed the case. Also included is a plot of $|z_{BB} - z_{ZDC}|$ showing their relative resolution to be $\sim 3.8cm$. This is useful information to bear in mind when starting to look at a third, hopefully more precise measurement.

7.1.4 TPM1

The first TPC in the BRAHMS mid-rapidity spectrometer arm, called TPM1, is our most precise vertex detector. It is described in detail in section 6.2.2, but for reference table 7.1 summarizes the most relevant parameters.

Width (x)	Height (y)	Depth (z)	Radial distance from $x = y = z = 0$
36.6 cm	20 cm	38.4 cm	94.5 cm

Gas mixture	Drift velocity	Possible angular settings
90–10 $Ar - CO_2$	0.0013 $cm/\mu s$	30^o – 90^o

Table 7.1: Parameters of TPM1. All coordinates are in the global system.

TPM1 is an efficient vertex detector because of its high tracking precision, its close proximity to the beamline and the fact that it is positioned before any magnetic field. Therefore, while TPM1 will see tracks from different background sources, secondary produced particles from weakly decaying hadrons etc., it will have a main contribution of tracks with flight paths pointing straight back to a small region around the primary interaction point. The tracks from background and secondaries will have a much wider distribution of intersections with the beam plane, so for events with several tracks one can easily find the spatial point pointed to by most of the tracks and this will be the vertex. This is the basic idea behind all vertexing with tracking chambers.

An important shortcoming deserves early mention here. TPM1 was designed to give a precise vertex in three dimensions for events with several reconstructed tracks. As will be shown below it performs well for the global y and z coordinates, but for x — radially outwards from the beamline in the plane of the center of the TPC — we get no measurement. This is due to a problem with the BRAHMS and TPM1 geometric design. The center of TPM1 is 95 cm radially removed from the beamline, while the TPC itself is 40 cm deep. Tracks fitted to data inside this volume and then projected back to the beamline come in at very steep angles, and the uncertainty introduced by the track fitting blows up and destroys our resolution along this axis. TPM1 is therefore only capable of producing a y and z coordinate, and we must look to the Si/Tile mult barrel for the possibility of an x determination.

7.2 BrVertex — vertex data object in BRAT

Before moving on to software details, I have to mention the way vertex information is structured in BRAT. I have written a class called **BrVertex**, which is a data object for storing information about a reconstructed vertex and the measurement uncertainty if applicable. Currently both TPC vertex algorithms described below and **BrRdoModuleZDC** create **BrVertex**–objects, and one will probably be created by **BrRdoModuleBB** as well at a later time. Table 7.2 summarizes some of the important functions of this data object class.

Function	Description
GetX(), GetY(), GetZ()	Get the vertex x, y, z coordinate
VertexFound()	Returns 1 if a vertex has been successfully determined
GetVertexZSigma()	Returns the sigma of the ClusterVertex fit
GetVarianceZ()	Returns the error on the mean of the ClusterVertex fit
GetVertexChisq()	Returns the χ^2 of the TrackVertex fit
GetVertexMethodUsed()	Integer saying which detector made the measurement

Table 7.2: Some important functions of the **BrVertex** class. See text for details. GetVertexZSigma() and GetVarianceZ() also exist for Y.

7.3 The TPC algorithms — Technical details and performance

A TPC records data in the form of sequences of ADC values with associated timebin numbers. As explained in sections 6.3 and 6.4, we do *clustering* and *tracking* on these sequences to find, respectively, some space–points that the particles traversed (clusters) and the paths they followed through the detector volume (tracks).

Then, when we wish to find the vertex, we need a software algorithm that looks at this preprocessed data and returns a collision point. In BRAT there are now two such algorithms, each in the form of a **BrModule** class: **BrTPMClusterVertexModule** and **BrTPMTrackVertexModule**. The first one works on clusters from the TPC while the second works on tracks, so their main difference is in how refined the data they use is.

I will in the following describe both of these algorithms in detail, and show how they perform both in simulations and for real data.

7.3.1 BrTPMClusterVertexModule

This algorithm is completely written by me, after a suggestion from Professor Dieter Röhrich.[4] Its basic idea is that if you combine two and two clusters in the TPC volume and then project the line between them back to the x=0 plane, the intersection points should be Gaussian distributed around the y and z coordinates of the vertex. A fit to these distributions gives me both a vertex measurement in two dimensions, and an event–by–event uncertainty in the vertex position.

[4]The same basic idea is also used in the PHOBOS experiment.

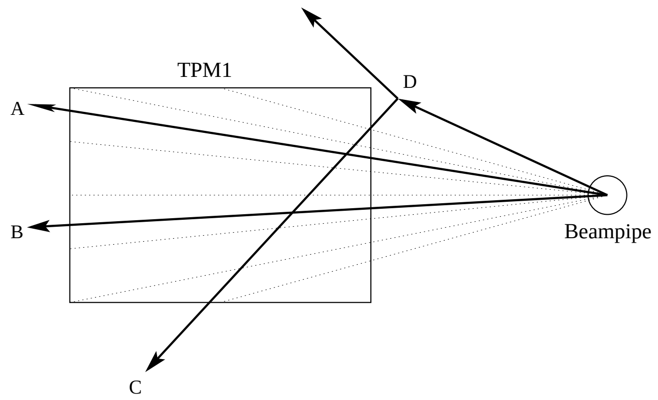

Figure 7.7: Illustration of slicing of TPM1. Assuming that the beam lies close to $y = 0$ primary particles (A and B) will make clusters in only one slice, while particles (D) from e.g. a weak decay (C) traverse several slices.

The algorithm in detail

BrTPMClusterVertexModule takes as input a list of clusters from TPM1, usually set by the commands[5]

```
ClusterVertexModule->
     SetDetectorHits(TpcClusterFinder->GetDetectorHits());
```

When the *Event()* call is given, the algorithm starts by dividing the TPC into a number of wedge–shaped slices pointing back to the assumed beamline — see figure 7.7. Each slice corresponds to an interval of $\frac{\Delta y}{\Delta x}$ from $x = y = 0$. This is done both to reduce background from combining unrelated clusters, and to reduce the CPU time used to produce a vertex. I have to assume here that the beam does not drift more than a few centimeters in the y direction — see sec. 7.3.1 Since TPM1 is placed before any magnetic field, we can assume that most primary particles will leave clusters within just one of these slices.

The number of slices must of course be tuned to get a maximum peak to background ratio, and based on GEANT simulations I have set a default value of 16 slices. When looking at real data it is clear that this value is too high — I will discuss this further in section 7.3.1. The number of slices to be used is setable by the command

```
ClusterVertexModule->SetVertexNumberOfSlices(integer);
```

[5]This breaks a central part of the BRAT philosophy — that modules should only receive data through a **BrEventNode** passed in the *Event()* call. It has not been changed, as I have not wanted to break existing analysis code in a time when so much analysis is being performed.

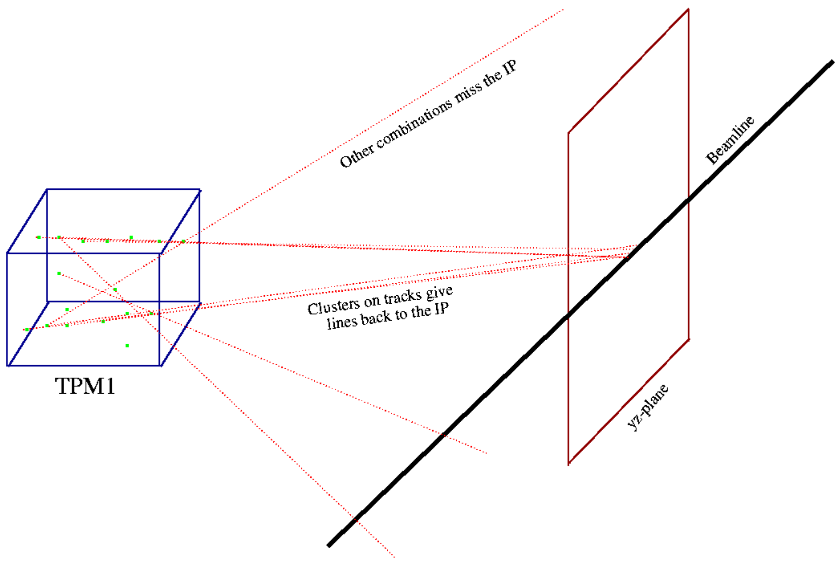

Figure 7.8: Schematic illustration of the **BrTPMClusterVertexModule** algorithm

The algorithm then assigns each of the clusters to one of these slices, and decides whether it is located in front of or behind the middle of the TPC.

Then, for each of the slices, the algorithm one by one combines all hits in the front half with all hits in the back half and for each combination makes a line in 3D space between them. These lines are projected back to $x = 0$, and the intersection points with this plane are put in two histograms — one for y and one for z. Figures 7.8 and 7.9 illustrate this process.

In the final step, a Gaussian is fitted to each of these histograms. The y coordinate is found directly as the mean of the fit to this first histogram, and I also determine the variance of the distribution and thus the error on the mean. For z, the original histogram is too coarse because of the wide spread of possible vertex locations. I therefore use this first histogram only to find the highest histogram channel, and then go through the combination sequence again in a narrow region around this position.[6] The zoomed histogram is then fitted with a Gaussian, and the mean and variance of this fit is taken as the position and uncertainty of the z coordinate.

After completing the vertex determination, a BrVertex object named *Cluster VtxData* is filled with the data from the fit and placed in the OutputNode supplied to *Event()*.

An important issue with this algorithm is its CPU usage. Especially for central event where there are many clusters to combine, it can get very slow since

[6]Essentially a rebinning of the histogram.

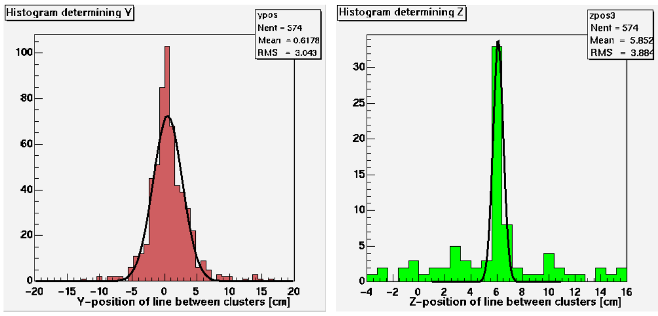

Figure 7.9: The histograms used by **BrTPMClusterVertexModule** to determine the y–and z–coordinate of the vertex. These pictures are from experimental data, and also show the Gaussian fit used to estimate the event–by–event uncertainty.

Parameter	Getter command	Cut value
Sigma of z histogram	GetVertexZSigma()	$<$ 2.0 cm
Error on the mean	sqrt(GetVarianceZ())	$<$ 0.8 cm
χ^2 of Least–squares fit	GetVertexChisq()	$<$ 5

Table 7.3: Cut parameters for well determined vertices from **BrTPMCluster-VertexModule** (two top rows) and **BrTPMTrackVertexModule** (bottom row)

the computing time goes roughly as $N^2_{Clusters}$. This makes the ClusterVertex impractical to use for e.g. fast multiplicity analyzes with the global detectors, but for precise PID which also needs time–consuming tracking algorithms the relative increase in CPU time is not that large.

Criteria for a well determined vertex

If the algorithm has a minimum number of clusters to work with and is able to fit a Gaussian to both histograms, it returns a flag saying it has found some vertex. This fit may still be very poor, so extra cuts must be imposed on the found vertices to keep only the good fits. Table 7.3 summarizes these cuts with my suggested values and how to get them from the BrVertex object. The exact values are chosen by analyzing both simulations and data to maximize the efficiency and precision while minimizing the background of uncorrelated events.

The variables I cut on are the following:

- The error on the mean of the z histogram, calculated as

$$\sigma(\bar{z}) = \frac{\sigma_{fit}}{\sqrt{N_{entries}}} \tag{7.10}$$

where σ_{fit} is from the fit to the data and $N_{entries}$ is the number of entries in the histogram within $\pm 3\sigma_{fit}$ of the fit mean. This procedure of mixing fit and measured values was derived from GEANT testing, and has proven to be the most effective way of cutting away bad fits.

- σ_z^{fit}, the sigma of the Gaussian fit to the histogram in the z direction. This extra cut is necessary to remove a class of events that have many noise clusters, making a wide distribution centered on 0 and drowning out the real signal.

Important setable parameters

Below is a list of some important setable parameters of **BrTPMClusterVertexModule**.

- SetVertexNoSlices(Int_t value) sets the number of $\frac{\Delta y}{\Delta x}$ slices. Default is 16.

- SetVertexMinNoPoints(Int_t value) sets the minimum number of clusters required in TPM1 to try to do vertexing. Default is 50.

- SetDrawHistogram(Int_t value) Set to 1 to draw the histograms used to determine y and z. Default is 0.

- SetRemoveBackgroundsOn() turns on functionality to subtract a linear background from the histograms before determining y and z. Default is false.

Simulations

My most important tool in creating and testing this algorithm has been simulations of collisions, starting with data from an event generator, propagating it through our detector setup using Geant 3.21 and then analyzing the result with ROOT and BRAT (see chapter 5).

I have mostly used the event generator FRITJOF 7.02, since most of our premade simulation files were made with this program. FRITJOF predicts very high particle densities at RHIC energies, much higher than the first RHIC data (see discussion in chapter 8), but since the issue here is the performance of a technical algorithm and not physical observables this does not cause a problem. It may actually be an advantage since this allows "worst–case" testing of the software, in the sense that it should work for our highest possible track densities.

A more serious problem is that simulations can never truly reproduce the response of a detector, since they are really tools for understanding the hardware before data are available. In my case the problem is that the simulation lacks the difficulties of an unknown or non–constant drift velocity, edge effects in the TPC and detector noise. Detector noise, here appearing as clusters not belonging to tracks, can of course be simulated, but since it has turned out that TPM1 was much more noisy than expected during year one of data taking this was not taken properly into account during the development of **BrTPMClusterVertexModule**.

These problems are luckily still minor when it comes to testing that the algorithm works, causing problems only for testing absolute efficiency and acceptance. To test my algorithm, I ran the standard clusterfinding algorithm on digitized data from Geant and passed the output to the module. After running the vertex finder, I compared the determined vertex to the "true", simulated vertex which I also get from Geant.

The upper row of figure 7.10 shows the distance in y and z between the vertex determined by **BrTPMClusterVertexModule** and the simulated GEANT vertex for central events[7] with the angle of the midrapidity spectrometer $\theta_{MRS} = 90^o$. The cuts on well–determinedness mentioned above have been included. As you can see the determination is very good for both coordinates, and fitting the histograms I estimate

$$\sigma_y^{ClusterVertex} = 0.17cm \tag{7.11}$$

$$\sigma_z^{ClusterVertex} = 0.11cm \tag{7.12}$$

i.e. of the order of a few millimeters. This is an order of magnitude better than the precision obtained by BB timing.

The efficiency of the algorithm, simply defined as

$$\varepsilon^{VertexFinder} = \frac{N_{OKvertex}^{Events}}{N_{Input}^{Events}} \tag{7.13}$$

is

$$\varepsilon_{Sim,Central}^{ClusterVertex} = 99.5\% \tag{7.14}$$

Of course these figures, being obtained for clean simulations and central events — which means lots of statistics — are not realistic, but can be considered an extreme upper limit to the precision that is achievable with this algorithm.

Since TPM1 moves with the midrapidity arm, the vertex algorithm must also be tested for any angle dependencies. I have done so for $\theta_{MRS} = 90^o$, 60^o and 35^o, and the results can be seen in table 7.4 and figure 7.10.

[7]Central here means an impact parameter of $b < 2fm$.

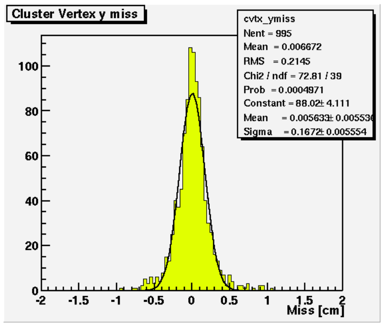

(a) y, 90^o

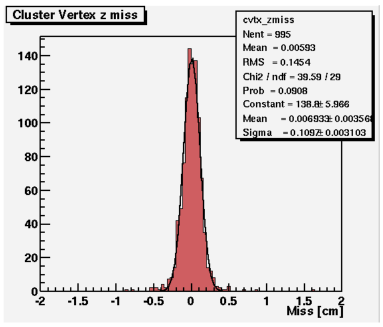

(b) z, 90^o

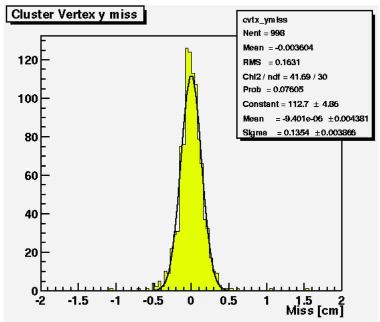

(c) y, 60^o

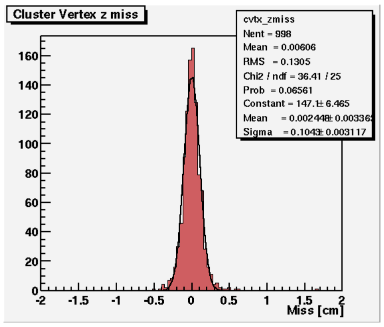

(d) z, 60^o

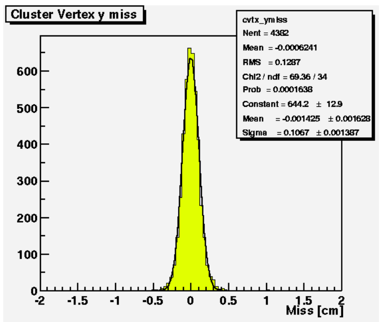

(e) y, 35^o

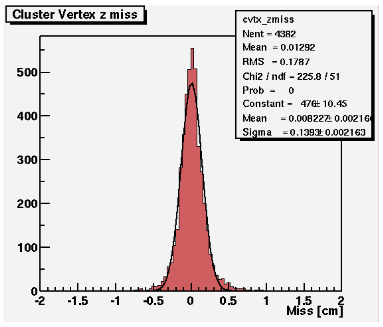

(f) z, 35^o

Figure 7.10: The “vertex miss” distributions of **BrTPMClusterVertexModule** in y (left column) and z (right column).

θ_{MRS}	σ_y (cm)	σ_z (cm)	Efficiency ε (%)
90	0.17	0.11	> 99
60	0.14	0.10	> 99
35	0.11	0.14	> 99

Table 7.4: Summary of the simulation performance of **BrTPMClusterVertexModule**.

The conclusion is that **BrTPMClusterVertexModule** works well on simulated data at all spectrometer angles, giving a precision on the order of a few millimeter in y and z and an efficiency of $\sim 99\%$ for central events.

Data

For real data, it is not so easy to estimate the performance of the vertexfinders. The main reason is of course that the vertex is unknown so that the precision cannot be calculated absolutely, and in addition noise and hardware problems cause unpredictable effects.

What can be measured is the efficiency of the vertex algorithms both as a function of θ_{MRS} and centrality, and its correlation with the global detectors. To do this, I first need to determine the vertex interval over which I trust the algorithm, since the geometry of TPM1 is such that it cannot possibly work well for all z–values. Figure 7.11 shows the total distribution of determined ClusterVertices after the cuts mentioned above are applied, for three spectrometer angles. See also fig. 7.22. It is clear that **BrTPMClusterVertexModule** has an optimal area centered on $z = 0$, and for consistency with other analyzes done in BRAHMS I restrict my further testing to $z = \pm 35cm$. This excludes any possible problems with a vertex dependent multiplicity — see sec. 8.3.2.

Figure 7.12 shows the correlation of the ClusterVertex with the BB determination. For all three angles there is a clear, sharp dependence with little noise. The width of the $|z_{BB} - z_{ClusterVertex}|$ distribution is shown in the lower row. It is this plot that was used in section 7.1.2 to determine the resolution of the BB vertex measurement.

Similarly, figure 7.13 shows the width and correlation with the ZDC measurement. There is still a sharp correlation at all angles, but here it is much wider and with more noise. This comes from the lower intrinsic timing resolution of the ZDCs relative to the BB counters.

In figure 7.14 I show the measured efficiency of **BrTPMClusterVertexModule**, subject to the cuts in fit sigma and error–on–the–mean. The symbols are circles for $\theta_{MRS} = 90^o$, squares for 60^o and triangles for 40^o. The x–axis corresponds to cuts in % of central collisions — see table 8.1 on page 103 for my definition of the centrality classes. For 90 and 60 degrees there is a maxi-

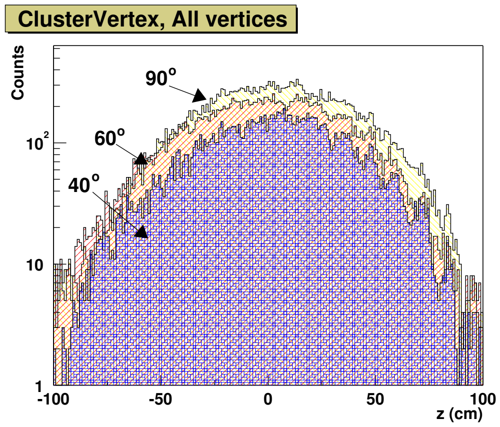

Figure 7.11: The full distribution of well–determined ClusterVertices for three spectrometer angles.

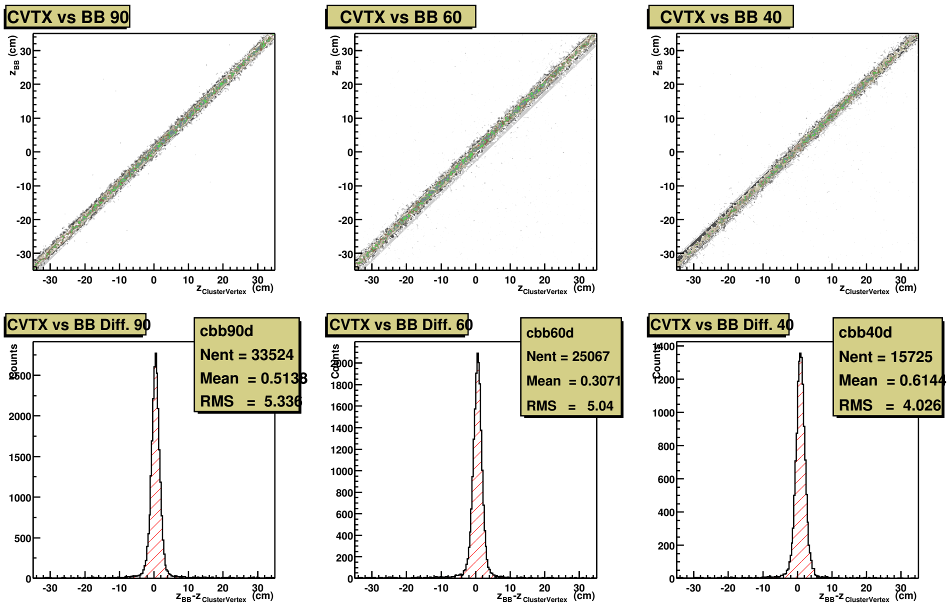

Figure 7.12: Upper row: The correlation of **BrTPMClusterVertexModule** and BB vertices for three spectrometer angles. Lower row: The difference between the two measurements.

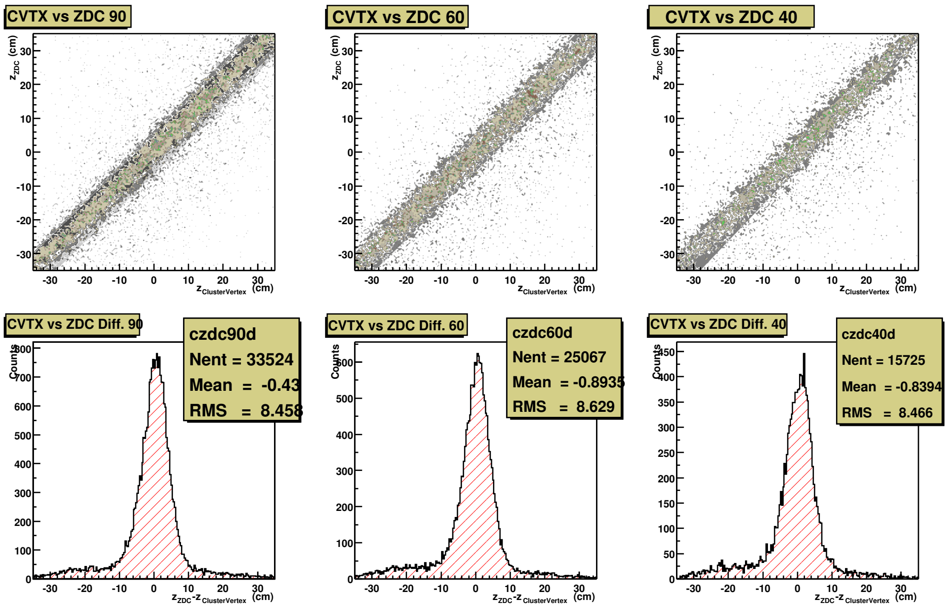

Figure 7.13: Upper row: The correlation of **BrTPMClusterVertexModule** and ZDC vertices for three spectrometer angles. Lower row: The difference between the two measurements.

mum for semi–peripheral events and lower efficiency for central and peripheral. This is because for peripheral events there are simply not enough clusters in the TPC to make a good determination, while for central collision there are so many clusters that no clear signal peak stands out of the background.

Compared with simulations, this efficiency is surprisingly low. One reason for this is of course the huge amount of noise clusters we saw in TPM1 during year one, but the main reason is probably another problem that was not detected until a short time ago — the beam y position:

A problem with the y determination

During the analysis of data from year one, a problem with the y–determination in **BrTPMClusterVertexModule** was discovered. See figure 7.15. From projecting tracks back to the beamplane it is clear the average beam y–position for the runs analyzed here[8] is at $\hat{y}_{Beam} \approx 1.5cm$, while the ClusterVertex places the distribution at $\hat{y}_{ClusterVertex} \approx 0cm$. This is an effect of the slicing of the TPC discussed above. It was designed to accept a beam–drift of up to $\pm 2cm$ in y since that was what the RHIC design crew said was probable, but the difference between simulations and real data has clearly invalidated this design. The effect

[8] Runs 2529–2531 and 2535.

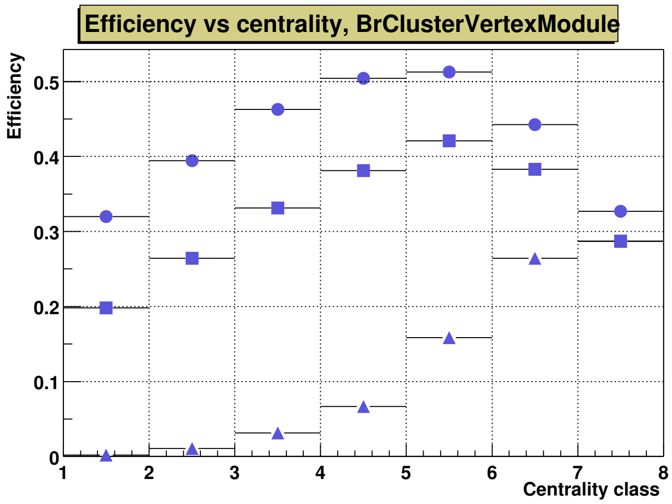

Figure 7.14: The efficiency of **BrTPMClusterVertexModule** for three spectrometer angles. Symbols: circles 90^o, squares 60^o and triangles 40^o.

of this problem is that tracks deposit clusters in several slices, probably causing a drastic reduction in the efficiency of the algorithm. This is the reason for the low numbers shown in figure 7.14.

The problem is easy to fix. One can for instance

- Reduce the amount of slices so that most tracks still fall within one regardless of y_{Beam}. This will increase the CPU–time consumed by the algorithm and possibly also reduce its precision.
- Feed the average y–position of the beam to the algorithm. This information should in any case be part of the BRAHMS run database, so this is probably the preferred solution since it involves no loss of precision.

Unfortunately, the problem was found too late for me to implement any of the above suggestions.[9]. It should be easy for any experienced BRAT programmer to do so, and if I get to go on to a PhD in the BRAHMS collaboration I will do so myself.

Once this problem is cleared up and TPM1 is rebuilt so that it is less noisy, I expect a drastic increase in the efficiency of **BrTPMClusterVertexModule**. Until then, it is still our most precise vertex finder independent of spectrometer angle, and should be used for all precision physics like calibrations etc. that is not too dependent on efficiency.

[9]After a discussion with F. Videbæk it was decided that I should rather concentrate on the analysis presented in chapter 8

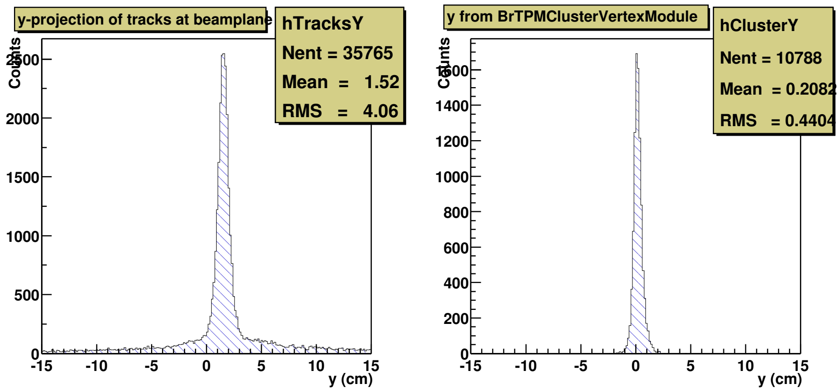

Figure 7.15: The effect of the y–determination problem. The tracks point back to an average $\hat{y}_{Tracks} \approx 1.5cm$, while **BrTPMClusterVertexModule** has a $\hat{y}_{CVtx} \approx 0.2cm$.

7.3.2 BrTPMTrackVertexModule

Our second algorithm works instead on complete tracks in TPM1, letting other parts of the reconstruction chain refine the data more before trying to locate the vertex. This has the advantage of greater speed, but as I will show below it reduces both efficiency and precision and also leaves us without the option of including the vertex location in the local tracking algorithms. Still, for central events or data taken with MRS at lower angles — i.e. when there is high occupancy in TPM1 — **BrTPMTrackVertexModule** works very well and is nicely complementary to **BrTPMClusterVertexModule**.

This algorithm was part of the software for the E866 fixed–target experiment at the AGS, and was originally adapted for BRAHMS by J.H.Lee. I have since heavily modified the actual code and some of the functionality, but the essence of the algorithm remains the same.

The algorithm in detail

BrTPMTrackVertexModule takes the output from either **BrTrackFollowFinder** or **BrTrackStringFinder**, e.g. by the command

```
TrackVertexModule-->
   SetDetectorTracks(TpcTrackFinder->GetDetectorTracks());
```

When the *Event()* routine is called, the algorithm first loops through all the tracks and projects them onto the x=0 plane. The intersections with this plane are given as input to a Least–Squares fitting algorithm and the three–dimensional point with the least distance to all the tracks is found. The χ^2 of

Setter command	Description
SetVertexCdaCut	Distance from vertex allowed before track is removed from list

Table 7.5: The setable parameters for **BrTPMTrackVertexModule**

this fit is also calculated, defined as

$$\chi^2 = \frac{\sum_i DCA_i^2}{\sum_j w_j} \tag{7.15}$$

where DCA_i is the distance of closest approach between the track and the proposed vertex, the sum going over x, y and z. w_j is a weight–factor associated with each track, and j runs over all tracks.

Then, for each track the algorithm checks if the point of closest approach to the determined vertex is outside some cut (see table 7.3.2 for a summary of the setable parameters), and if so removes the track from the list. Accepted tracks receive weight factors equal to the inverse of their closest distance of approach. The Least–Squares fitting is rerun, and new closest approach distances and χ^2 are calculated. This process is looped until either the χ^2 stops reducing or the number of tracks still within the cut is less than some setable cut. This cut is the only major setable parameter in this algorithm.

After completing the vertex determination, a BrVertex object called *Track VtxData* is filled with the data from the fit and placed in the OutputNode supplied to *Event()*.

Criteria for a well–determined vertex

To be able to reconstruct a vertex, **BrTPMTrackVertexModule** of course needs a minimum of two tracks in TPM1. There is no upper cut to the number of tracks that can be used. The other parameter that can be used to determine if a TrackVertex is "well–determined" is the χ^2 from the Least–Squares fit. The better this fit the better the precision of the algorithm in simulations and the better its correlation with the global detectors. For my analysis, I have set a value of

$$\chi^2_{Cut} = 5 \tag{7.16}$$

chosen by analyzing both data and simulations and trying to maximize the algorithm's precision and efficiency while minimizing the background of uncorrelated events. See table 7.3.

Simulations

As with **BrTPMClusterVertexModule**, I have used simulations of collisions from FRITJOF 7.02 and Geant to test how well this algorithm works. The

θ_{MRS}	σ_y (cm)	σ_z (cm)	Efficiency ε (%)
90	0.12	0.17	92
60	0.10	0.52	93
35	0.08	0.75	92

Table 7.6: Summary of the simulation performance of **BrTPMTrackVertex-Module**.

same problems as mentioned above exist here, but in addition any problems with the track finding software will propagate to the vertex determination. During the course of my work our tracking classes have continually improved, and consequently the accuracy and efficiency of **BrTPMTrackVertexModule** has kept improving. The results below are obtained with latest tracking software at the time of writing.[10]

Figure 7.16 shows the "vertex miss" distributions for **BrTPMTrackVertex-Module** at three spectrometer angles, central events. Unlike the ClusterVertex, the TrackVertex precision is clearly dependent on θ_{MRS}, getting very wide at 40 degrees. The reason for this is the uncertainty that comes from the track fit to the clusters. Because TPM1 is quite far away from the beampipe a small change in the track angle will cause a large change in where the track intersects the beamplane. The 3–D Least–Squares fit then runs into problems since it looks for the point in space closest to all tracks. For $\theta_{MRS} = 90^o$ this problem lies only in the global x coordinate and does not much affect the z measurement, but for lower spectrometer angles the problem starts affecting z too and results in the observed loss of precision. This problem is a general feature of this algorithm, and cannot be avoided without fundamental changes.

Table 7.6 summarizes the simulation precision of the TrackVertex, and also shows its average efficiency for central events. Notice that while the z precision sinks with the angle, the y precision increases as the algorithm gets more tracks to work with. The efficiency is $> 90\%$ for all angles.

Data

Figure 7.17 shows the total distribution of determined TrackVertices after the χ^2 cut is applied, for three spectrometer angles. See also fig. 7.22. Again the optimal area is centered on $z = 0$, and is somewhat smaller than for the ClusterVertex. Still, for consistency, I restrict my further analysis to $z = \pm 35cm$ even though this is probably too wide to assume a z–independent efficiency.

Figures 7.18 and 7.19 show the widths and correlations of the TrackVertex with the BB and ZDC. The correlation is again seen to be good for all three an-

[10]Including a crash–free version of **BrTrackFollowFinder** that is not yet included in BRAT.

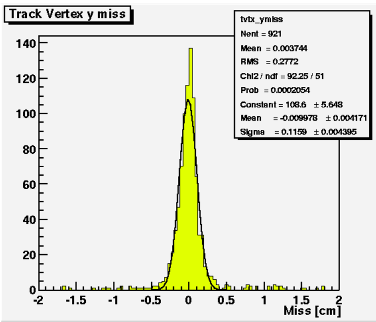

(a) y, 90^o

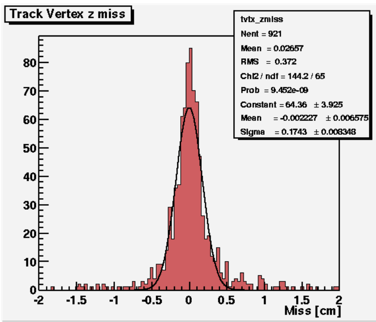

(b) z, 90^o

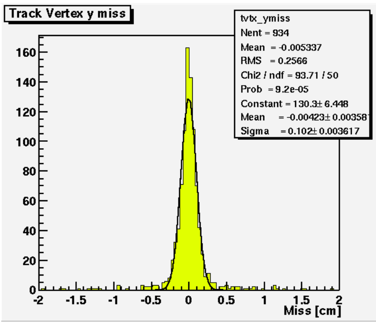

(c) y, 60^o

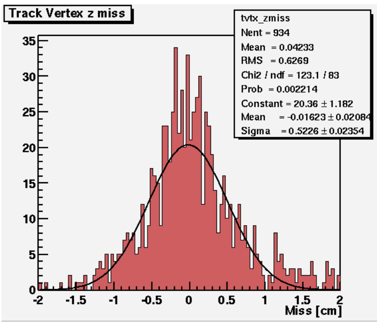

(d) z, 60^o

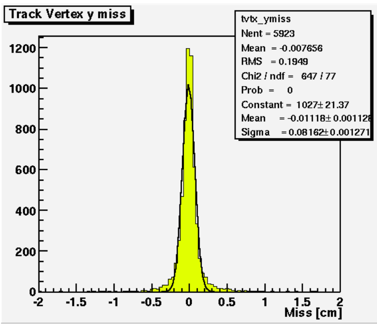

(e) y, 35^o

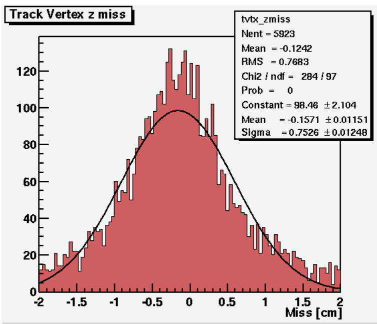

(f) z, 35^o

Figure 7.16: The “vertex miss” distributions of **BrTPMTrackVertexModule** in y (left column) and z (right column).

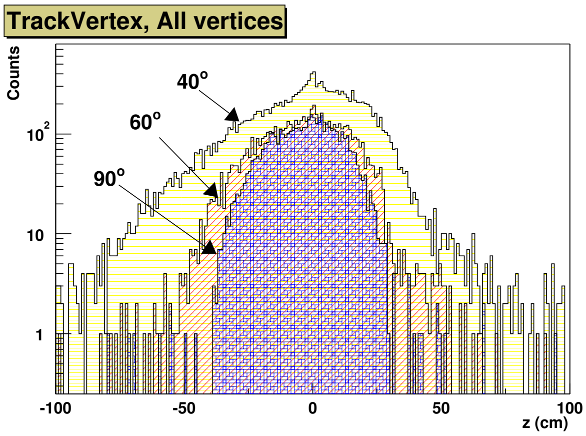

Figure 7.17: The full distribution of well–determined TrackVertices for three spectrometer angles.

gles, but here there is a slight angle–dependence of the width. Since the BB and ZDC work under the same conditions for the three runs I interpret this as the precision problem mentioned above — the 3–D Least–Squares fit has problems determining the z coordinate precisely at sharp spectrometer angles. Also, the width is at all times seen to be greater than the corresponding one for the ClusterVertex. Based on this, I conclude that **BrTPMClusterVertexModule** is the more precise of the two at all angles.

For efficiency, **BrTPMTrackVertexModule** works a lot better than **BrTPMClusterVertexModule** for central events — see figure 7.20, where the x–axis is again the centrality class to be described in section 8.3.2. For intermediate and peripheral events it is slightly less efficient. This is not surprising, since the main difference between the algorithms is that the TrackVertex works on further–refined data (tracks) and consequently needs more statistics to work well. On the other hand, it is free of the noise–problem that plagues the ClusterVertex at central events and low spectrometer–angles. Figure 7.20 also shows that the TrackVertex is most efficient at $\theta_{MRS} = 40^o$, where the ClusterVertex is at its worst. For all angles we see a smooth drop in efficiency with centrality, as expected since centrality is on the average proportional to statistics (i.e. number of tracks).

7.4 Combining the TPC algorithms

All in all it is clear that we are able to extract precise vertices from TPM1 that are well correlated with the global detectors, and that we have two vertex algorithms that have somewhat complementary properties. We can take advantage of this to increase the overall performance of TPM1 vertexing by running

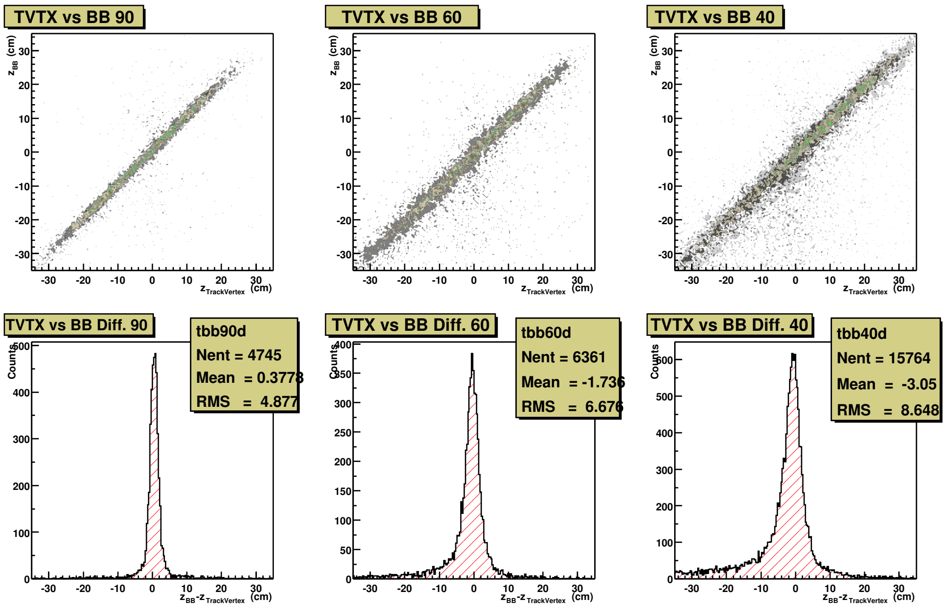

Figure 7.18: Upper row: The correlation of **BrTPMTrackVertexModule** and BB vertices for three spectrometer angles. Lower row: The difference between the two measurements.

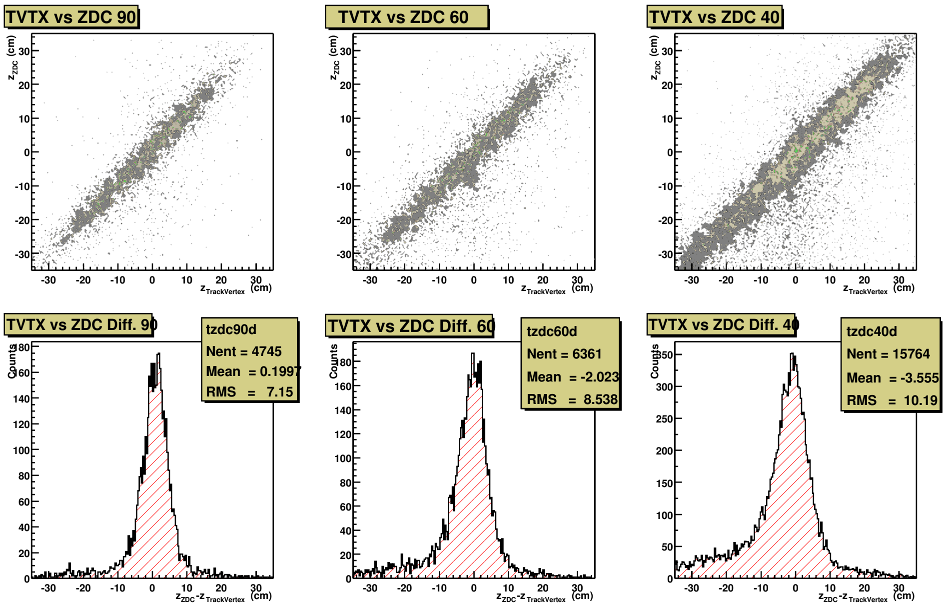

Figure 7.19: Upper row: The correlation of **BrTPMTrackVertexModule** and ZDC vertices for three spectrometer angles. Lower row: The difference between the two measurements.

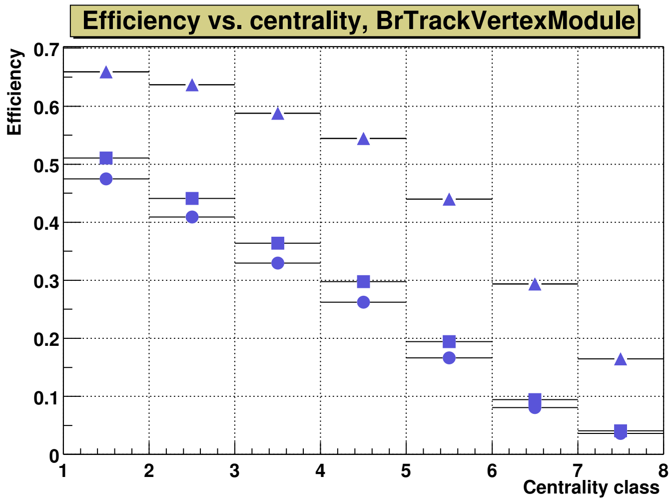

Figure 7.20: The efficiency of **BrTPMTrackVertexModule** for three spectrometer angles. Symbols: circles 90^o, squares 60^o and triangles 40^o.

both algorithms and then requiring only that either of the two fulfills its cut parameters. I have done this in figure 7.21 which shows the resulting efficiency for three spectrometer angles.

From this plot it is clear just how complementary the algorithms are — the ClusterVertex inefficiency for central events is compensated by TrackVertex and vice versa. In total we see the same functional dependence of efficiency on centrality for all spectrometer angles and achieve a total efficiency for TPM1 vertexing of

$$\varepsilon^{TPM1}_{Central} \approx 60\% \tag{7.17}$$

$$\varepsilon^{TPM1}_{Peripheral} \approx 45\% \tag{7.18}$$

As mentioned at the end of section 7.3.1, once TPM1 is rebuilt and the y–problem is sorted out the efficiency of **BrTPMClusterVertexModule** is expected to increase greatly and subsequently the total TPM1 vertexing efficiency will increase also.

Another interesting comparison is the z dependence of the efficiency of the algorithms versus the BB and ZDC. This is shown for $\theta_{MRS} = 90^o$ in figure 7.22, and it is clear that while the distributions shown in figures 7.11 and 7.17 extend almost all the way to $\pm 100cm$ the algorithms are not really efficient beyond $|z| \sim \pm 35cm$.

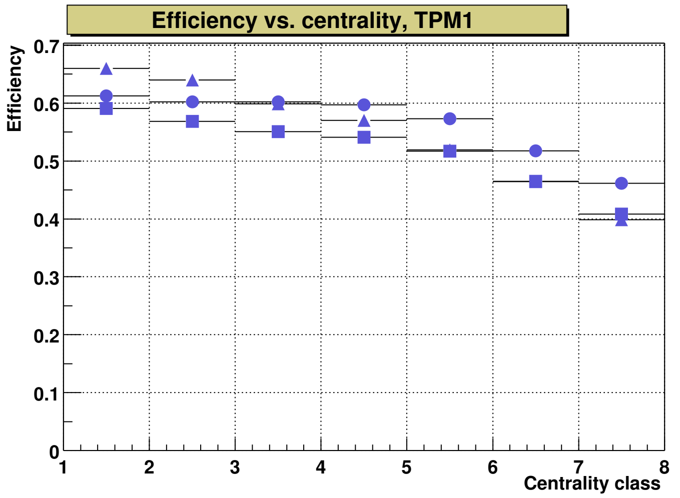

Figure 7.21: The total efficiency of TPM1 vertexing for three spectrometer angles. Symbols: circles 90^o, squares 60^o and triangles 40^o.

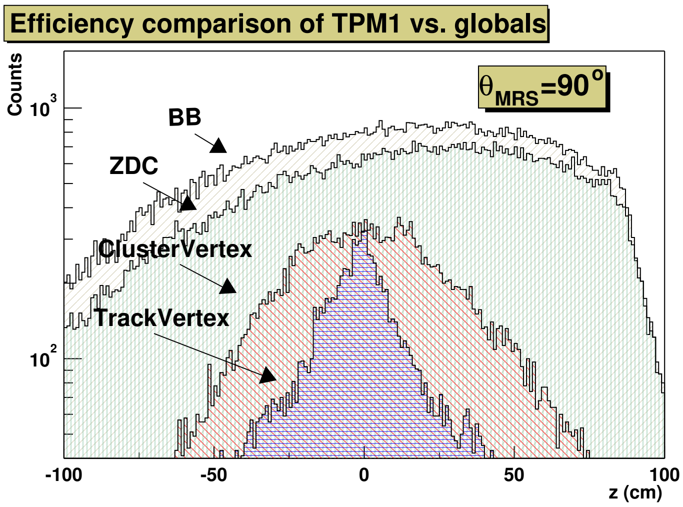

Figure 7.22: Distributions of well–determined TPC vertices and ZDC and BB measurements.

7.5 Global vertex — combining the measurements

Finally, I wish to mention the BRAT–class **BrVertexModule**. It is still under construction, but is intended to be a tool for combining all available vertex information into a single, global vertex. It currently does the following:

1. Look for vertex information from BB and ZDC timing, and assign to them an uncertainty equal to the sigma of the resolution vs TPM1 plots shown above. If no information is found, look for raw BB or ZDC data and calculate the vertex position.

2. Look for TPM1 clusters and run both Cluster– and Track–algorithms. Do tracking if necessary. If one of the measurements meets its requirements use that, if both do use the ClusterVertex since it is in general more precise. Currently assigns an uncertainty from the error–on–the–mean for a ClusterVertex or a constant determined from a resolution plot versus well–determined ClusterVertices for a TrackVertex.

3. Calculate a weighted mean of position and uncertainty, using all available data. Return a BrVertex–object with the new information.

This procedure is still rather rough and should probably be amended in many regions. Suggestions or plans that were not realized due to time shortage are

- Demand a certain consistency between the measurements before they are included. Use BB as a basis, since it seems to be the most reliable.

- Calculate a better event–by–event precision from the two TPM1 algorithms.

- Include data from the Tile– and Silicon Multiplicity arrays, which can also give vertex information.

The completion of **BrVertexModule** is left to any interested BRAT programmer, or possibly myself if I continue to work in BRAHMS.

Chapter 8

$dN/d\eta$ measured with TPM1

A central measurement for any heavy ion experiment is the number of charged particles produced per collision, or multiplicity. This number, and how it varies with pseudorapidity (η) and the centrality of the collision can tell us much about the dynamics of the nucleus–nucleus collision and about QCD phenomenology.

In this chapter, I will present a measurement of the charged particle production per unit rapidity (denoted $dN/d\eta$) using the BRAHMS time–projection chamber TPM1. I'll first give a brief summary of the physics that can be derived from this measurement, then present the different sub–detectors in BRAHMS sensitive to the charged particle density and finally present the analysis itself. I will compare my numbers to other measurements and model predictions, and finally use them to estimate the scaling of $dN/d\eta$ with the number of binary collisions. I will also employ both this fit and an eikonal formalism to extract an estimate of the percentage of the charged hadron production at midrapidity that is due to "hard", or perturbative, processes.

At the BRAHMS collaboration meeting in April 2001, it was decided that the official centrality classes for use in our publications should be 0–5%, 5–10%, 10–20%, 20–30%, 30–40% and 40–50%. Since most of this thesis was by then ready I will keep my seven planned classes (see tab. 8.1) in this presentation, but I give the numbers for the above classes in appendix A.

8.1 The physics of $dN/d\eta$

Related physical quantities

$dN/d\eta$, the average number of charged particles produced per unit of pseudorapidity and per collision, is linked to many physical observables. How it varies with η gives us information both on the NN cross–section [7] through

$$\sigma_{NN} \propto [\Gamma(\frac{dN}{d\eta})]^{-1} \tag{8.1}$$

where $\Gamma(\frac{dN}{d\eta})$ is the width of the distribution, and on the degree of stopping experienced by the colliding nuclei. It also gives us an estimate of the initially produced energy density, through

$$\epsilon_0 = \frac{m_T}{\tau_0 A}\frac{dN}{dy}|_{y=y_{CM}} \tag{8.2}$$

as derived by Bjorken [62].[1] How ϵ_0 varies with the system size (number of participants) and $\sqrt{s}$ energy is a sensitive probe of the onset of new physics, e.g. the formation of a Quark–Gluon Plasma.

$dN/d\eta$ is also related to the entropy production in a heavy–ion collision[63]. By integrating over a small region around midrapidity we can find the total multiplicity of produced particles

$$n = \int_{-y_0}^{y_0} (dN/dy)dy \tag{8.3}$$

where this central multiplicity can be assumed to go as $n \sim \sigma V$. Here σ is the average entropy density and V is the system volume. Any increase in n must mean an increase in σ and/or V. Similarly, the transverse momentum p_T is related to the temperature T of the system, and in a phase transition we expect the entropy to increase while T remains constant. A plot of dN/dy versus the transverse momentum p_T should therefore show a plateau or a region of smaller slope if a phase transition of first or second order respectively occurs.

See section 8.10 for further discussions of physics related to $dN/d\eta$.

A few comments on interpretation

I need to make a few remarks about the observable I am about to present a measurement of.

First of all, what I will below call $dN/d\eta$ is in reality $\frac{dN_{Charged}}{d\eta}$, since charged particles are all we can measure with a TPC. A common assumption is that most produced hadrons are pions, and they come in two charged versions and one uncharged: π^+, π^0 and π^-. If one also assumes that they are produced in roughly equal numbers, we get the relation

$$\frac{dN}{d\eta} \approx \frac{3}{2}\frac{dN_{Charged}}{d\eta} \tag{8.4}$$

This is a common way of estimating the total number of produced particles. I will below use $dN/d\eta$ for simplicity, but I return to this point in section 8.10.

[1] Note that at central rapidities the rapidity y and pseudorapidity η are not equal, but they are easily convertible into each other. A commonly used assumption for $y < \eta$ is $dN/dy \approx 1.1 \cdot dN/d\eta$.

8.2 $dN/d\eta$ in BRAHMS

To measure $dN/d\eta$, a detector needs to be able to determine the number of particles hitting it after one collision event. Some way of determining how many of these are primary particles is also desirable to help in removing the background of e.g. decay products, but this can also be done from GEANT simulations.

The BRAHMS experiment has five sub–detectors capable of multiplicity measurements. The most obvious ones are the Tile and Silicon multiplicity array situated around the beampipe at z=0 and the beam–beam counters, and in addition the first TPC in the midrapidity arm (TPM1) can give a more precise multiplicity measurement from tracking at $0 < \eta < 1.3$ and T1 in the forward arm can do the same at $1.3 < \eta < 3$.

8.2.1 Mult and BB

The BRAHMS multiplicity barrel (see sec. 4.6.3), was built to measure the event centrality, which is derived from a careful measurement of the multiplicity. This subdetector is therefore ideally suited for precise $dN/d\eta$-measurements.

Each of the tiles and Si–strips measures an ADC signal induced by the energy deposited by passing charged particles, and since we can assume that all particles at this energy scale are near–MIPs [2] the ADC signal will be roughly proportional to the number of particles. A conversion factor based on GEANT simulations is used to correct for any non–proportionality — see [64]. Combining this with the vertex location and correcting for

- the different lengths that the particles have to travel in the detector material (see fig. 8.1)
- the acceptance of the TMA and SMA
- the fact that for most particles $< \frac{dE}{dx} >>< \frac{dE}{dx}_{MIP} >$, if we believe the particle species and momenta generated by e.g. HIJING

gives a $dN/d\eta$ measurement.

The BRAHMS multiplicity barrel nominally covers an η range of $\sim \pm 2.1$ for the tiles and $\sim \pm 1.9$ for the Si–strips, and can resolve the $dN/d\eta$ structure within this area.

The second $dN/d\eta$ detector system in BRAHMS are the two Beam–Beam arrays. Like the tiles, the Čherenkov material that is the essential part of each tube gives a signal to the photomultipliers (PMTs) that is proportional to the number of particles hitting the tube. Here also, corrections related to both the PMTs and the background of non–primary particles have to be made, but after

[2] MIP = Minimum Ionizing Particle. See e.g. [48] p. 27.

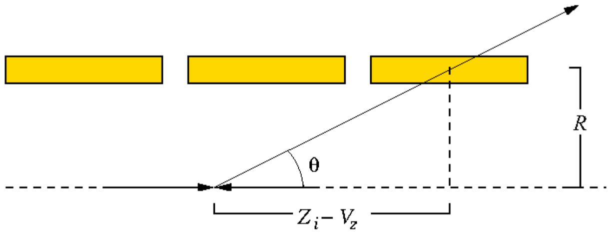

Figure 8.1: Geometric correction for the length of material traversed by the particles, as function of the vertex location. Taken from [65].

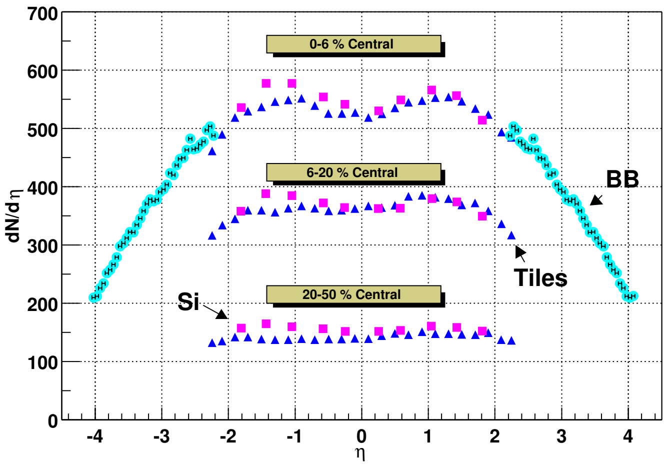

Figure 8.2: $dN/d\eta$ measurements from the global detectors for three centrality classes. No systematic errors are included.

this is done we can extract a $dN/d\eta$ from the BBs in a pseudorapidity range of $\sim \pm(2.1 - 4.0)$. See [66] for the details of this analysis.

Figure 8.2 shows the latest $dN/d\eta$ values from the global detectors. Their complementarity in η coverage gives a nice, continuous measurement, and their measured values are all consistent with each other. Systematic errors are not yet included. I will return to this measurement in section 8.9.

8.2.2 The tracking chambers

The TPCs are the third set of BRAHMS subdetectors that can produce multiplicity information, unique because here we can employ pure track counting. No estimate of any average energy deposit is needed. TPM1 is especially well suited since it is positioned before any magnetic field and can therefore select primary particles by demanding that the straight–line extrapolations of the tracks point back to the vertex. TPM1 covers an η-range of roughly 0 to 1.3, depending on the MRS angle θ_{MRS}.

For runs with no magnetic field, T1 can also easily be used to measure $dN/d\eta$ at more forward rapidities. Its performance is mostly limited by its small acceptance due to the size of the magnet gap, but given enough statistics T1 can produce data in the η-range 1.5 to 3 depending on the FFS angle θ_{FFS}. Claus E. Jørgensen, NBI, has recently done an analysis with $\theta_{FFS} = 4^o$ — see [61] and sec. 8.9.

It is also possible to measure $dN/d\eta$ with T1 with the magnetic field on, but then the acceptance and background corrections become very complicated, and we may lose the low–p part of the particle distribution.

8.3 Centrality selection

To measure anything as a function of centrality, one must of course first have some way of determining the centrality on an event–by–event basis. This is a highly non–trivial task in any heavy ion experiment, and at the time of writing there is no clear consensus in BRAHMS on how to do this best. What I present below is the method that most people in the collaboration currently trust, and that is likely to be at least a close predecessor of the final method that we will use. I'll only give a brief outline of the method - for details, please refer to [64].

To recapitulate, the event centrality is a measure of how large the impact parameter is. The most central events are the ones with an impact parameter of 0, while the most peripheral events will have an impact parameter of roughly

$$b_{max} = r_T + r_P \tag{8.5}$$

where r_T is the target radius and r_P is the projectile radius. For all data in this thesis the two are equal:

$$r_T = r_P = r_{Au} \approx 7fm \tag{8.6}$$

The main difficulties are the following:

1. Find some minimal detector response that clearly separates a nuclear interaction from peripheral electromagnetic dissociation events[67] or junk events like beam–gas interactions.

2. Determine the corrected response of different detectors to a sample of events, and check that they consistently select the same fraction of the min. bias distribution.

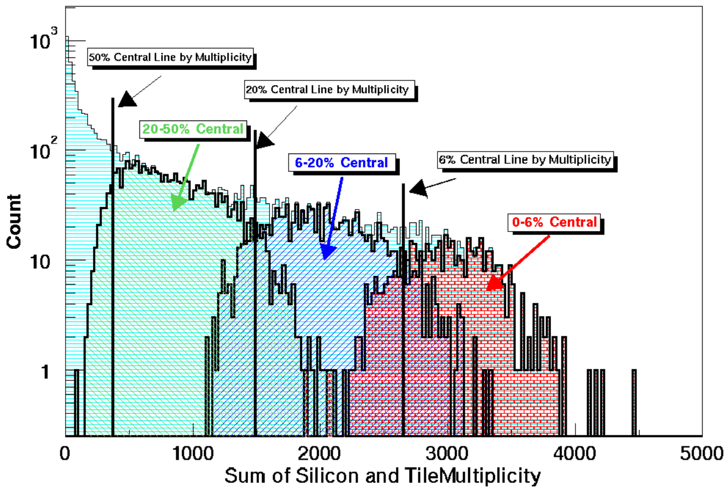

Figure 8.3: Minimum bias distribution from a GEANT simulation of the tile and Si arrays. The continuous distribution is the measured tile multiplicity, and the black lines correspond to the events with 6%, 20% and 50% highest multiplicity respectively. The three superimposed distributions show the response of the Si strips for events within a given range of impact parameters as given by HIJING, determined by the Tile+Si cut. Taken from [64].

8.3.1 The minimum bias distribution

If we assume that we have correctly selected all and only nuclear events and then plot the response of a multiplicity detector for all of these, the result is known as a *minimum bias distribution*. Its shape is closely related to the nuclear density distribution, and largely known from theory. A good indication of whether or not we understand our centrality is our ability to reproduce the expected min–bias.

Figure 8.3, taken from [64], shows the min–bias from a GEANT simulation of our tile and Si arrays. The continuous distribution is the simulated sum of Tile+Si multiplicity, and the black lines correspond to the events with 6%, 20% and 50% highest multiplicities respectively. The three superimposed distributions show the response of the Si strips for events within a given range of impact parameters as given by HIJING, determined by the Tile+Si cut.

This simulation shows that we can place reasonable trust in the output from the tile and Si array, provided that we can somehow select collision events.

In ref. [64], this is done by first plotting the response of the ZDCs versus the multiplicity measured by the big BB tubes while requiring that the vertex determined by the two be within ±15 cm of each other. See figure 8.4. In this plot a cut can easily be made that removes events with uncorrelated responses.

In ref. [64] it is shown that this cut almost reproduces the simulated min–

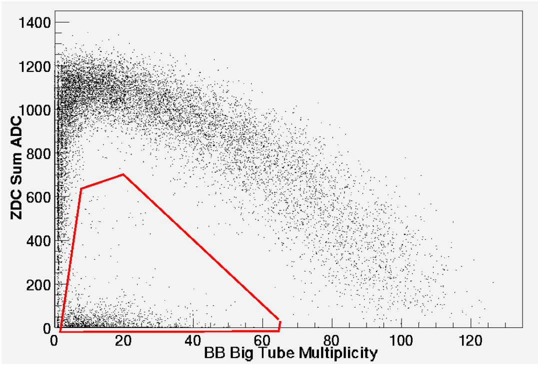

Figure 8.4: BB big tube multiplicity vs. ZDC sum ADC. The enclosed area corresponds to background or non–collision events. Taken from [64].

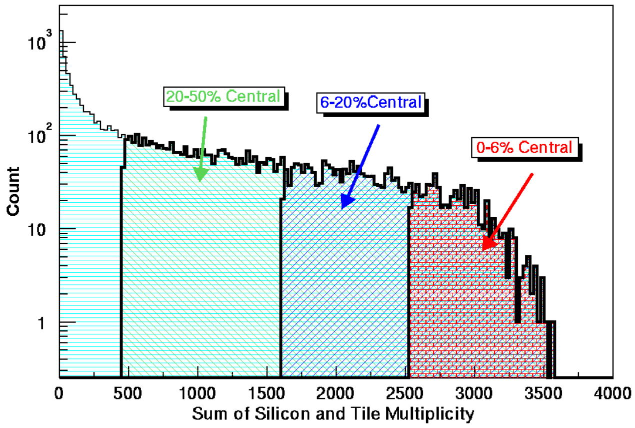

Figure 8.5: The experimental min-bias distribution, measured by the Tile and Si arrays. Taken from [64].

bias shown in figure 8.3, deviating only in the most peripheral bins. Some additional cuts in the correlation between the multiplicity seen by the tiles and the Si-strips are imposed to eliminate this problem (again, please refer to ref. [64] for details), and finally the spectrum shown in fig. 8.5 is obtained.

8.3.2 Centrality selection in BRAHMS

As hinted at in figure 8.5, we select centrality by making cuts in the experimental distribution of the multiplicity sum from the tile and Si arrays. This method requires careful calibration of the detectors on a run–for–run basis, and at the time of writing this data is being prepared for the BRAHMS run database.

There is also an issue of the vertex dependence of the centrality cuts. Figure

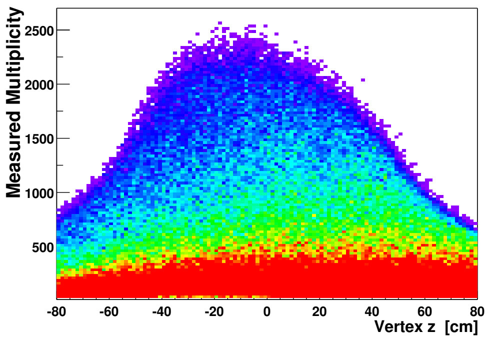

Figure 8.6: The response of the Tile Multiplicity Array versus the vertex position. Figure taken from [61].

8.6 shows the response of the Tile Multiplicity Array versus the vertex position, and there is clearly a large dependence. Since the Tiles are essential to the centrality selection I use, my analysis can only be made in a certain limited vertex region. Below, I will restrict my reconstruction to events that have

$$|z_{BB}| < 35cm \tag{8.7}$$

in response to this problem.

The analysis presented below uses the centrality determined by **BrMultCentModule** from BRAT-1-15-7, the version thought to be final by Steve Sanders who wrote it. The calibration files I have used are listed in table 8.2.

I will divide the min–bias distribution into seven centrality classes. This number is chosen to balance the need for statistics against the wish for a detailed $dN/d\eta$ vs. centrality plot. Table 8.1 shows my naming–convention and what the classes correspond to in percent of most central collisions. The runs I use for my analysis have trigger 4 downscaled, meaning that we have elected not to record all the peripheral collisions. This means that I do not see a full min–bias in my analysis, but since **BrMultCentModule** is calibrated with a complete min–bias run this does not affect my centrality selection.[3] Figure 8.7 shows the multiplicity distribution from my 90^0 analysis[4], together with the seven centrality classes defined in table 8.1.

For a more detailed description of **BrMultCentModule**, see [64]. (This writeup refers to **BrRdoModuleMult**, a predecessor of the current classes that contains the same physics.)

[3]This in turn means that the calibrations I use are not from my data–runs. This adds to my systematic errors, but since all the calibrations are virtually identical I will ignore this effect for the rest of this analysis. From the calibration files I estimate this effect to be on the 0.1% level.

[4]See table 8.2.

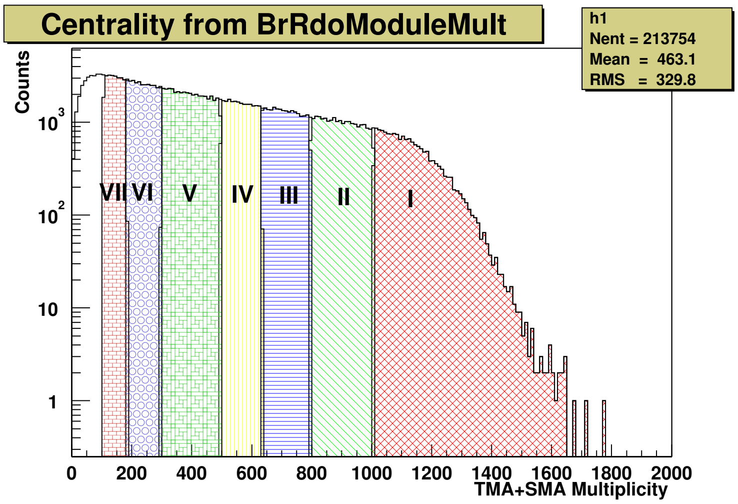

Figure 8.7: The TMA+SMA multiplicity as calculated by **BrRdoModule-Mult**, and my centrality classes, for runs 2529–2531 and 2535. This module is the immediate predecessor of **BrMultCentModule**, and produces the same output.

8.4 Measuring $dN/d\eta$ with TPM1

While TPM1 is a detector with a very limited geometric acceptance, its tracking precision and ability to select tracks that actually point back to the vertex make it an ideal multiplicity detector close to midrapidity. Given an ideal detector and ideal software, you would simply count the number of tracks that point to the vertex, average over all events in one centrality class and multiply by a geometry factor to get $dN/d\eta$. In the real world, however, things are not as easy. We have to take into account problems with the reconstruction of the

Cent. class	Centrality region (%)
1	0-5
2	5-10
3	10-15
4	15-20
5	20-30
6	30-40
7	40-50

Table 8.1: The centrality classes used in my analysis. The regions are given in % of most central events.

events, noise in the TPC and related problems with the tracking software, the background of secondary particles that still point back to the vertex etc.

In the following sections I present a thorough analysis of TPM1 data from the summer of 2000 RHIC run (year 1) taking these effects into account, leading up to a $dN/d\eta$ measurement over a wide centrality range at three η-points from 0 to 1. I will show that my numbers are consistent both with the numbers from the BRAHMS mult–barrel and with similar measurements published by the PHOBOS and PHENIX collaborations.

8.4.1 Event reconstruction

The first step in the analysis is to reconstruct tracks in TPM1. The analysis chain proceeds as follows:

1. Use the classes **BrRdoBB** and **BrRdoZDC** to find the vertex determined by the BB's and ZDC's and require that they agree to within ± 15 cm.

2. Use **BrTPCPreProcess** to clean up the data in TPM1. The main reason for this is that we know that TPM1 has a lot of noise in its early time-bins, and that the raw data will contain negative ADC values because of pedestal subtraction.

3. Use **BrTPCClusterFinder** to find the hits in the detector.

4. Use **BrTrackFollowFinder** to find the tracks in the detector.

Please refer to chapter 6 for a more detailed description of each step in the analysis.

There are a lot of tunable software parameters in this procedure that can influence the result. In appendix C I give a list of the parameters I have used, and section 8.7 gives a discussion of their systematic effects on the result. These parameters are probably not optimal in reducing the amount of background and ghost tracks, both since **BrTrackFollowFinder** operates with very wide search windows and the *MaxPixelCutoff* of the ClusterFinder is set very low. I have kept them since they were used in the analysis presented by F. Videbæk at QM2001 [68], to retain consistency. I will show in section 8.7 that this choice has a minimal impact on the end result.

I have reconstructed from raw data several runs at three different MRS angles, totaling $\sim 200k$ events at $\theta_{MRS} = 90^o, 40^o$ and $\sim 60k$ events at $\theta_{MRS} = 60^o$ where there is only one long run available. See table 8.2 for details. This sample contains events with all centralities, subject only to the requirements

$$|z_{BB}| < 35cm \tag{8.8}$$

$$|z_{BB} - z_{ZDC}| < 15cm \tag{8.9}$$

MRS angle	Runs	N_{Events} accepted	Calibration run
90	2529, 2530, 2531, 2535	213k	2530
60	2523	60k	2521
40	2516, 2517, 2518	125k	2517

Table 8.2: The data–runs and calibrations used in this analysis.

8.4.2 Extracting the number of tracks per event

The next step is to divide the events into centrality classes as described in section 8.3.2, impose any additional vertex cuts and count the number of "good" (see below) tracks per event.

Vertex cut

A problem with the centrality selection that I have used is that it has a slight dependence on the vertex position for a large vertex range. Also, since the TPC acceptance is approximately constant while the vertex is moving, a wide vertex range will widen the pseudorapidity range of the reconstructed tracks. For these reasons I have imposed a vertex cut of

$$|z_{BB}| \leq 15cm \tag{8.10}$$

This drastically reduces my event sample, but not so much that it seriously increases my statistical error.

Cuts on the track position

An additional problem is the possibility of unpredicted effects near the edges of the TPC, and to avoid this I also impose a cut on which tracks to count based on the position where they cross the midplane of the TPC. Because of my vertex cut, the only adverse effect this has is to further reduce the geometric acceptance of TPM1.

The cuts I have imposed, in the local coordinates of TPM1, are shown in table 8.3. Figure 8.8 shows the plots I have used to determine this acceptance. At 90^o and 60^o I could have extended the region towards higher values of x, but I chose not to in order to be more or less consistent with a similar analysis made by F. Videbæk [68]. At 40^o one half of the TPC shows large efficiency problems, so I have removed this region from my analysis.

A cut on the distance from the vertex

One of the advantages of using a tracking detector for this measurement is that we can see the particles flight path in three dimensions. This allows me to

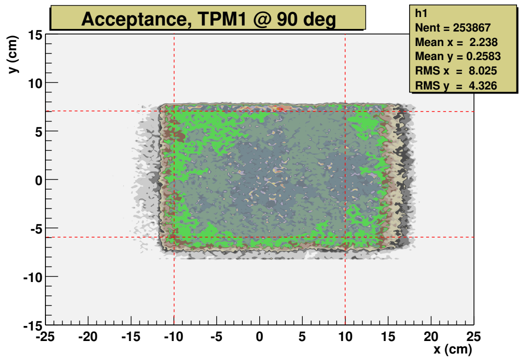

(a) $\theta_{MRS} = 90^o$

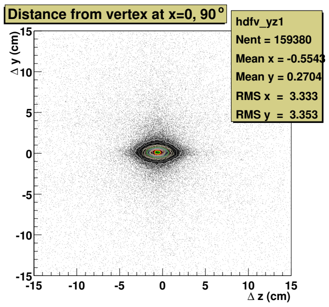

(b) $\theta_{MRS} = 90^o$

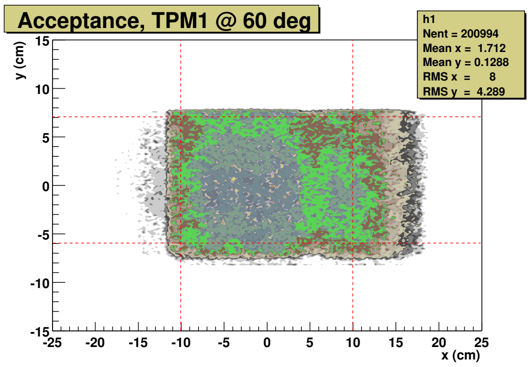

(c) $\theta_{MRS} = 60^o$

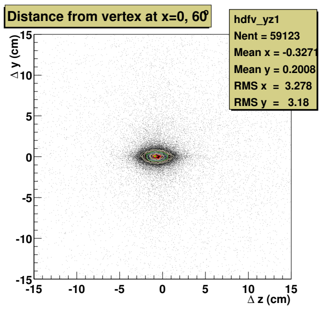

(d) $\theta_{MRS} = 60^o$

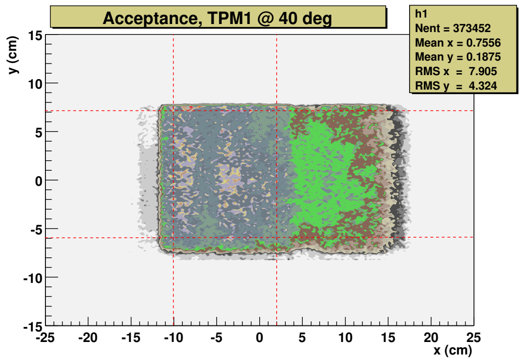

(e) $\theta_{MRS} = 40^o$

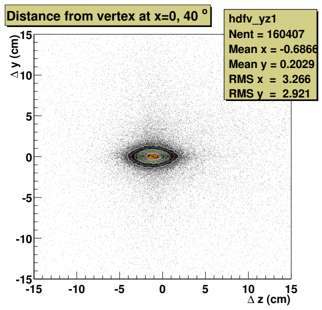

(f) $\theta_{MRS} = 40^o$

Figure 8.8: Left: The density of tracks crossing the midplane of TPM1 and my imposed cuts. Right: The distance from the vertex of tracks projected to $x = 0$. An offset of $y = -2cm$ has been imposed because of the beam being located at $y = 2cm$.

θ_{MRS}	$x_{Track}^{Midplane}$ cut	$y_{Track}^{Midplane}$ cut
90	-10<x<10	-6<y<7
60	-10<x<10	-6<y<7
40	-10<x<2	-6<y<7

Table 8.3: Cuts imposed on the track position at the midplane of TPM1.

impose an extra cut on the track position when projected back to the beamline to get rid of tracks that are clearly not relevant to my analysis. See figure 8.8.

In my N_{Tracks} distribution, I ideally wish to include only primary particles. Because many secondary hadrons and delta electrons from the beamline will have the same characteristics as primaries this is not possible, so I will have to subtract the background from these particles later on (see sec. 8.4.4). I will show below that this background can be assumed to be double–Gaussian, with the signal of primaries forming a third, sharp Gaussian peak. I fit this signal peak, and require of my tracks that they have

$$D_y < 3 \cdot \sigma_y^{Signal} \tag{8.11}$$

where D_y is the distance from the vertex in y,[5] in order to be classified as a primary. See sec. 8.4.4 for a further discussion of this. I will take the effect of this cut into my systematic uncertainty in sec. 8.7.

Results

Having made all these cuts, I can extract $< \frac{N_{Tracks}}{N_{Events}} >$ for my seven centrality classes at the three MRS angles. Examples of two N_{TPM1}^{Tracks} distributions from my 90^o dataset are shown in figure 8.9, and the mean values are also shown in table 8.4.

8.4.3 Efficiency corrections as a function of the number of clusters

The next problem to deal with is determining our absolute tracking efficiency. Many factors can cause problems for the trackfinders:

- Hardware problems can cause clusters to be lost in one or more padrows
- Close–lying clusters may not be correctly resolved and deconvoluted by our software
- Noise in the TPC may confuse our pattern–recognition software

[5]The y coordinate is perpendicular to the floor in the BRAHMS IR.

	$<\frac{N_{Tracks}}{N_{Events}}>$		
Cent. Class	90^o	60^o	40^o
1	2.52±0.02	3.35±0.04	3.97±0.03
2	2.03±0.01	2.75±0.03	3.29±0.02
3	1.63±0.01	2.18±0.03	2.68±0.02
4	1.31±0.01	1.76±0.03	2.22±0.02
5	0.940±0.007	1.23±0.02	1.62±0.01
6	0.576±0.006	0.79±0.01	1.04±0.01
7	0.349±0.006	0.46±0.01	0.64±0.01

Table 8.4: The uncorrected number of accepted tracks per event for each centrality class, after cuts on midplane position and distance from vertex in y.

- The tracking–software itself may have bugs or inefficiencies

These and other things may cause us to lose tracks from in principle reconstructible particles.

To deal with this, we need a measure of the number of tracks we lose *on the average* as a function of the amount of data in the TPC. I will describe here the procedure we have used in Oslo to estimate this functional dependence. This work has been done mostly by Truls M. Larsen and Trine Tveter, with a little help from myself.

The efficiency algorithm

We have used a simple technique, inserting simulated tracks into real events on the raw data level. The procedure is as follows:

1. Use GEANT to simulate single particles of known species and momentum flying at different angles through the active volume of the TPC.

2. Digitize these simulated tracks using **BrDigitizeTPC** [6] to simulate our detector response.

3. Reconstruct raw data events and save the track information.

4. Reconstruct the digitized GEANT tracks using standard tracking software to make sure it is possible to find it in the absence of background and other tracks.

5. For each reconstructible simulated track, add the digitized TPC sequences of this track to the raw data sequences using **BrTPCSequenceAdder**[7].

[6] Trine Tveter has done a lot of work on the functional form of the digitization functions. For details, please refer to [69] and [58]

[7] BRAT class recently written by Truls M. Larsen

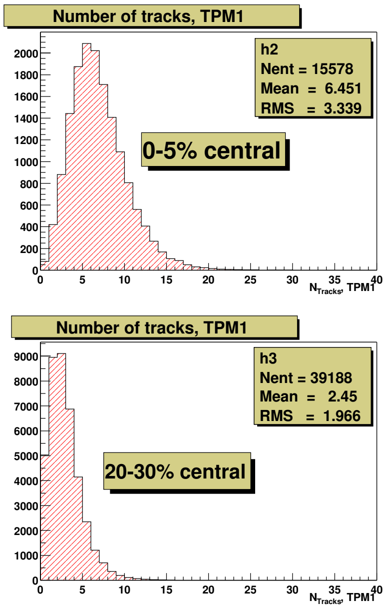

Figure 8.9: Distribution of N^{Tracks}_{TPM1} for two centrality classes, with $\theta_{MRS} = 90^o$

6. Reconstruct the combined event, and see if the added track is reconstructed.
7. Do this for a variety of test particle species and momenta.

Our tracking efficiency is then simply the ratio of the number of events where the inserted track was found to the total number of events reconstructed after track insertion.

To begin with we calculated the efficiency as a function of the number of tracks originally found. However, we soon saw that this gave a non–linear multiplicity dependence of the efficiency that changed as a function of centrality. We therefore tried to plot the same quantity versus the number of original clusters in the TPC, and this time the dependence was smooth and centrality independent. See figure 8.10, which shows efficiency versus tracks in the left column and versus clusters in the right column, for three different centrality classes.

Average efficiency versus $N_{Clusters}$

Since particles of different momentum will deposit different amounts of energy in the TPC, the average tracking efficiency is correlated with the momentum distribution of our particle spectrum. For one momentum and particle species,

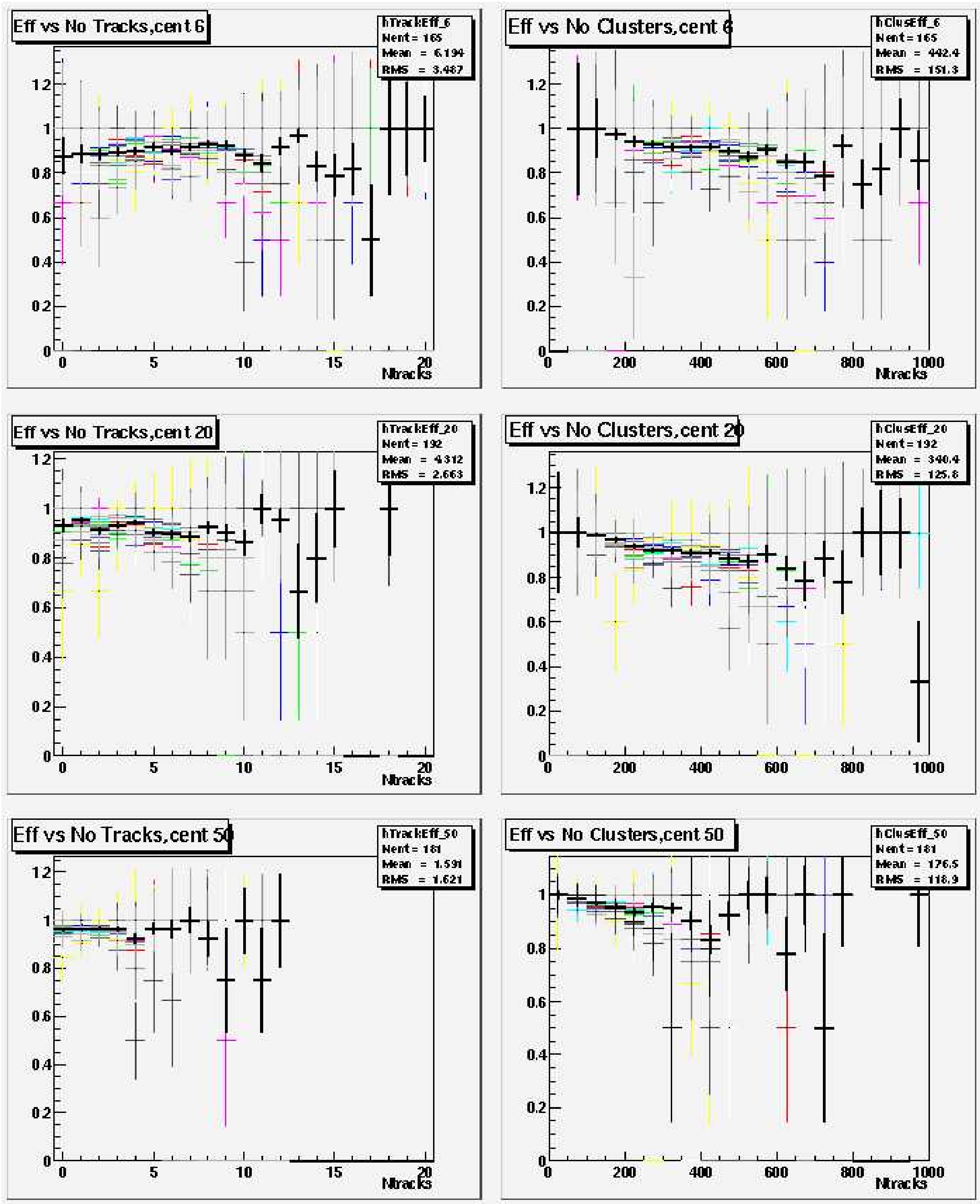

Figure 8.10: Efficiencies as a function of number of tracks and clusters for three centrality bins. The black points are the sums of the other points, which come from different sequences of run 2530. The left column shows the efficiency as function of the number of tracks, and the right as a function of the number of clusters in TPM1. See [69].

Pion energy (GeV)	Slope a
0.1	$0.9 \cdot 10^{-4}$
0.2	$1.3 \cdot 10^{-4}$
0.5	$1.5 \cdot 10^{-4}$
1.0	$1.5 \cdot 10^{-4}$
4.0	$1.3 \cdot 10^{-4}$

Table 8.5: The slopes of a linear fit to the measured tracking efficiency vs. $N_{Clusters}$ for different pion energies. $\theta MRS = 90^o$

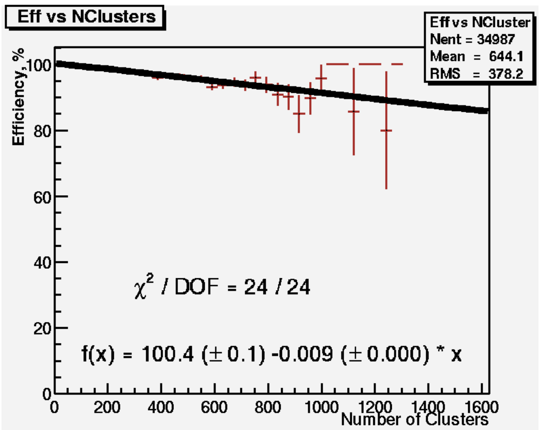

Figure 8.11: Tracking efficiency versus $N_{Clusters}$ for 0.1 GeV pions, measured for TPM1 at 90^o.

we have

$$\epsilon(N_{Clusters}, p, i) = 1 - a(p, i) \cdot N_{Clusters} \tag{8.12}$$

where i is the particle species and p is the momentum.

Using the algorithm just described and data generated by Truls M. Larsen, I can find the slope a of efficiency versus $N_{Clusters}$ for pions at four different energies — see table 8.5 and a sample dependency in figure 8.11.

Making the assumption that the source is a thermal emitter of pions, I can then calculate the average slope $\hat{a}$ from

$$\frac{1}{p_T}\frac{dN}{dp_T} \approx \frac{k}{T}\sqrt{m_T}e^{-\frac{m_T}{T}} \tag{8.13}$$

where k is some constant. (See [11], eq. (4.17).) I also assume

$$T = 565MeV[70] \tag{8.14}$$

$$m_T = \sqrt{m_\pi^2 + p_T^2} \tag{8.15}$$

Inserting the values from table 8.5 and assuming a linear dependence between my data points I get out an average slope of

$$\hat{a} = 1.45 \cdot 10^{-4} \tag{8.16}$$

This gives me an average tracking efficiency versus $N_{Clusters}$ of

$$\epsilon_{TFF}^{TPM1,90^o}(N_{clusters}) = 1 - 1.45 \cdot 10^{-4} \cdot N_{clusters} \tag{8.17}$$

Note that this dependence is calculated for TPM1 with the MRS at 90^o. It will be different for all other TPCs and also for lower spectrometer angles, but since this study has not yet been done[8] I will use the above formula at all angles. I take the error introduced by this into my systematic uncertainty in section 8.7. Another difference is that it is calculated for a version of TFF that was prone to "giving up" at high cluster multiplicities, but I assume that since the basic algorithm is the same the effects of this will be much smaller than the systematic error I arrive at in section 8.7.

Calculating the corrected $< \frac{N_{Tracks}}{N_{Events}} >$

I can now use what I know about tracking efficiency and the distribution of N_{Tracks} and $N_{Clusters}$ to calculate the corrected $< \frac{N_{Tracks}}{N_{Events}} >$ for each centrality bin. I use the formula

$$N_{Tracks}^{Total} = \sum_{N_{Tracks}} N_{Tracks} \sum_{N_{Clusters}} \frac{N_{Events}(N_{Tracks}, N_{Clusters})}{\epsilon_{TFF}} \tag{8.18}$$

to get the estimated number of tracks observed after the corrections, and divide this number by

$$\sum_{N_{Tracks}} \sum_{N_{Clusters}} N_{Events}(N_{Tracks}, N_{Clusters}) \tag{8.19}$$

which is the total number of events in each centrality class.

The statistical uncertainty is calculated by varying each of the entries in $N_{Events}(N_{Tracks}, N_{Clusters})$ and by its square root and then recalculating $< \frac{N_{Tracks}}{N_{Events}} >$ in each case. The uncertainty is then

$$\delta < \frac{N_{Tracks}}{N_{Events}} >^{Stat} = \sqrt{\sum_i [< \frac{N_{Tracks}}{N_{Events}} > (N_i = N + \sqrt{N}) - < \frac{N_{Tracks}}{N_{Events}} > (N_i = N)]^2} \tag{8.20}$$

where N_i are the entries in the matrices above.

The results of this analysis are shown in table 8.6.

[8]The results will probably be included in the master thesis of Truls M. Larsen

	$< \frac{N_{Tracks}}{N_{Events}} >_{Corrected}$		
Cent. Class	90^o	60^o	40^o
1	2.71±0.02	3.68±0.04	4.67±0.03
2	2.16±0.02	2.99±0.04	3.78±0.03
3	1.72±0.01	2.33±0.03	3.01±0.02
4	1.37±0.01	1.86±0.03	2.45±0.02
5	0.974±0.008	1.30±0.02	1.75±0.01
6	0.591±0.007	0.82±0.01	1.10±0.01
7	0.357±0.006	0.48±0.01	0.67±0.01

Table 8.6: The efficiency corrected number of tracks per event in the accepted TPC volume for each centrality class.

8.4.4 Subtracting the background of secondary particles

So far I have not made any requirement that the particle be a primary, e.g. emanate from the vertex, other than the 3σ cut in the track distance from the beam y (see sec. 8.4.2). Therefore the numbers in table 8.6 also include unwanted contributions from secondary decay products, rebounding products of interactions with magnets or other material, delta electrons from the beampipe etc.

To remove this contribution, I plot the y–projection of all the tracks at global x=0, i.e. in the middle of the beampipe. Primary tracks should form a peak around the beam y–position while all unwanted tracks should form a wide background, possibly with some substructure. Fitting and subtracting this background should give a measure of the ratio of primaries to secondaries in my selected track sample.

In figure 8.12 I show an example histogram of the y–projections of all tracks from events in one centrality class. It is fitted with the sum of three Gaussians (solid line):

1. The narrow signal peak.
2. A smaller distribution around the signal, probably due to delta electrons from the beampipe and possibly slow protons.
3. A wide background from decays, interactions with magnet material, ghost tracks etc.

My assumption that all contributions are Gaussian seems consistent with the distribution.

To estimate the background ratio I integrate the distribution inside $\pm 3\sigma$ of the signal peak, and the sum of the two background contributions in the same

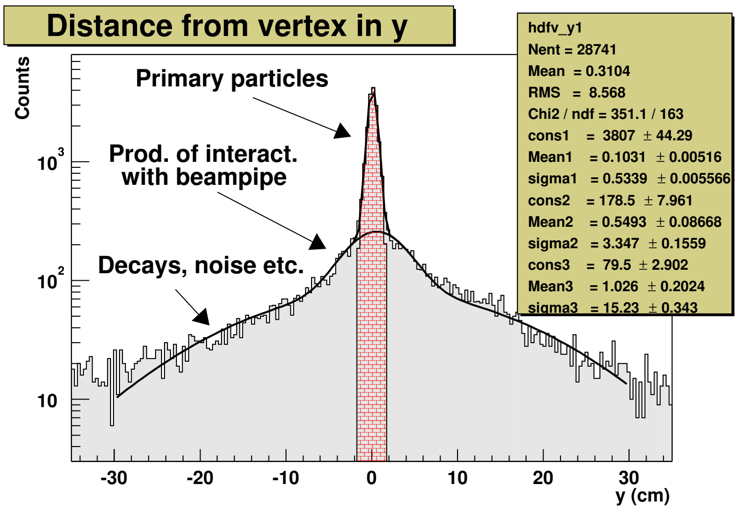

Figure 8.12: The y projection at the beamline of all tracks from events within one centrality class at $\theta_{MRS} = 90^o$. The fit is the sum of three Gaussians, and the background is computed as the ratio between the two background fits and the histogram contents within 3σ of the mean of the signal peak.

area. My assumption is that

$$< \frac{N_{Primaries}}{N_{Tracks}} >= 1 - \frac{I_{Background}}{I_{SignalPeak}} \tag{8.21}$$

Table 8.7 shows the result of this procedure for three spectrometer angles.

8.4.5 Ghostbusting

Ghost–tracks, tracks found by the tracking algorithms that do not correspond to the path of a charged particle, are always a possible problem for tracking chambers. They may be caused by noise clusters that line up to look like a track, by the cluster deconvolution routine splitting of fluctuations at the edge of real clusters and thus forming two parallel tracks etc. In my analysis so far I have not made any attempt to deal with this problem.

In his thesis[61], Claus E. Jørgensen presents a ghost–busting analysis based on a mixed–event principle. He looks through a reconstructed data file and histograms the spacing between tracks in an event at the backplane of TPM1. Then he makes a sample of "mixed events", combining a random set of tracks from different events into one event, to remove any possible correlations that may come from e.g. single tracks splitting into two parallel ones. The spacings between tracks at the backplane is again histogrammed. The first histogram is divided by the second, and if there is no correlation in track separation the result should be one over the entire histogram range.

	$< \frac{N_{Primaries}}{N_{Tracks}} >$		
Cent. Class	90^o	60^o	40^o
1	$4.50 \cdot 10^{-2}$	$5.10 \cdot 10^{-2}$	$5.65 \cdot 10^{-2}$
2	$4.87 \cdot 10^{-2}$	$5.31 \cdot 10^{-2}$	$4.81 \cdot 10^{-2}$
3	$4.84 \cdot 10^{-2}$	$4.65 \cdot 10^{-2}$	$4.70 \cdot 10^{-2}$
4	$4.75 \cdot 10^{-2}$	$4.96 \cdot 10^{-2}$	$4.46 \cdot 10^{-2}$
5	$4.42 \cdot 10^{-2}$	$4.97 \cdot 10^{-2}$	$4.49 \cdot 10^{-2}$
6	$5.46 \cdot 10^{-2}$	$5.02 \cdot 10^{-2}$	$5.09 \cdot 10^{-2}$
7	$4.34 \cdot 10^{-2}$	$5.17 \cdot 10^{-2}$	$5.21 \cdot 10^{-2}$

Table 8.7: The percentage of background tracks within the 3σ peak for three MRS angles and seven centrality classes.

Figure 8.13 shows his output for TPM1 at 90^o, 40^o and 4^o. The two upper panels are of interest to my analysis — they both show an increased probability of low track spacings relative to the mixed events.[9] Some of this increase may be due to the decay of particles close to the TPC with a small opening angle, but most of the drastic increase seen for low separations is probably due to our clusterfinder splitting single clusters and thus making two parallel tracks.

I have used this plot to find an estimate of the ghost–to–real ratio in my reconstructed files. Like Claus (see [61]) I look at the space between the tracks at the backplane of TPM1 (see fig. 8.14), and assume that tracks closer than 1.5 cm *may* be ghosts. From fig. 8.13 I get the probability that each one is a ghost, assuming that the ratio should have been one. This gives me a "worst case" estimate of

$$N_{Ghosts} = \sum_{i=1-3} N^i_{Spacings} \cdot \frac{1}{H(i)} \tag{8.22}$$

where i is the histogram bin and $H(i)$ is the histogram value for the i'th bin.

To correct my $dN/d\eta$ numbers for the ghost presence, I multiply them by

$$f_{GhostCorrection} = 1 - \frac{N_{Ghosts}}{N^{Total}_{Tracks}} \tag{8.23}$$

where N^{Total}_{Tracks} is the total number of accepted tracks.

I assume that $f_{GhostCorrection}$ is independent of vertex position, at least within my $|z| < \pm 15cm$ cut, but not independent of centrality. Table 8.8 shows the values of $1 - \frac{N_{Ghosts}}{N^{Total}_{Tracks}}$ I get for my analysis, i.e. the percentage of the total number of tracks that are probably ghosts. The 90^o and 40^o numbers are calculated from figure 8.13, while for 60^o I have interpolated between these two values.

[9]The bottom panel behaves differently. This is because here he has used **BrTrack-StringFinder** which has an internal ghost–busting routine that removes closely separated tracks. The plot shows that this routine may be somewhat overefficient.

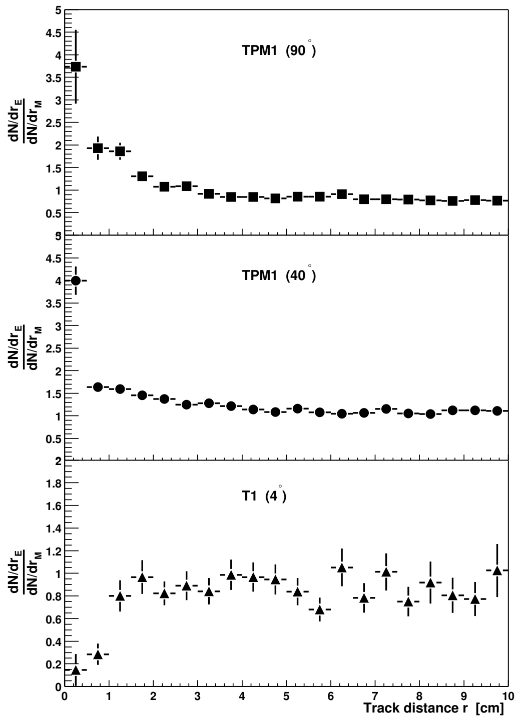

Figure 8.13: Ratio between track distance distribution of tracks from the same event dN/dr_E and tracks from different events dN/dr_M (mixed tracks). Taken from Claus E. Jørgensens thesis — see [61] for details and analysis.

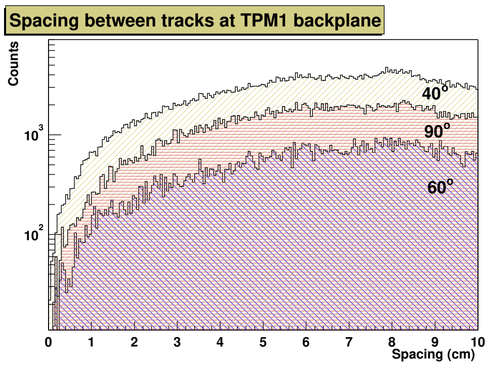

Figure 8.14: Separations between tracks at the backplane of TPM1.

	$<\frac{N_{Primaries}}{N_{Tracks}}>$		
Cent. Class	90^o	60^o	40^o
1	$1.01 \cdot 10^{-2}$	$2.04 \cdot 10^{-2}$	$2.73 \cdot 10^{-2}$
2	$9.92 \cdot 10^{-3}$	$1.72 \cdot 10^{-2}$	$2.20 \cdot 10^{-2}$
3	$8.22 \cdot 10^{-3}$	$1.42 \cdot 10^{-2}$	$1.82 \cdot 10^{-2}$
4	$6.04 \cdot 10^{-3}$	$1.13 \cdot 10^{-2}$	$1.48 \cdot 10^{-2}$
5	$4.92 \cdot 10^{-3}$	$8.87 \cdot 10^{-3}$	$1.15 \cdot 10^{-2}$
6	$4.65 \cdot 10^{-3}$	$5.51 \cdot 10^{-3}$	$6.09 \cdot 10^{-3}$
7	$2.79 \cdot 10^{-3}$	$5.87 \cdot 10^{-3}$	$7.92 \cdot 10^{-3}$

Table 8.8: The percentage of the total number of tracks in my analysis that are estimated to be ghosts, as a function of θ_{MRS}. The number for 60^o is interpolated between the two others. The analysis is based on numbers presented in [61].

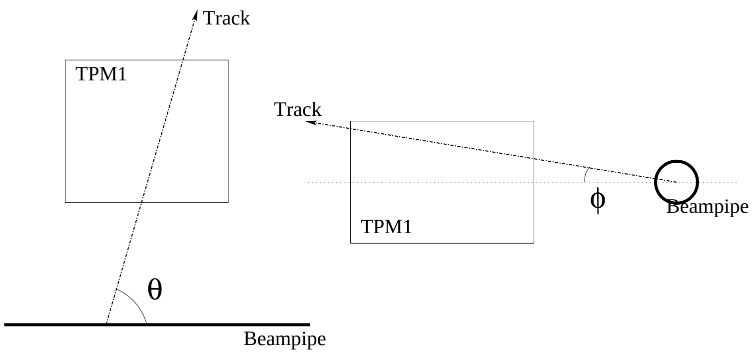

Figure 8.15: Definition of the angles used in section 8.4.6. θ is the angle between the track and the beam axis, while ϕ is the track's elevation from the xz–plane.

8.4.6 The geometric acceptance of TPM1

The last thing that must be known to calculate $dN/d\eta$ is the geometric coverage of TPM1, since what we measure is of course only a small part of phase space. We need the acceptance in ϕ (refer to figure 8.15 for definitions of the angles used in this section) and in θ, which will in turn give the acceptance in pseudorapidity or η.

η correction

The correction in θ (or η) is complex, since a moving vertex will change the η acceptance of TPM1. Especially at lower MRS angles this becomes a problem.

I make the approximation that θ is the angle of the track with respect to the beam axis *in the xz–plane*, since this will simplify the following calculations.

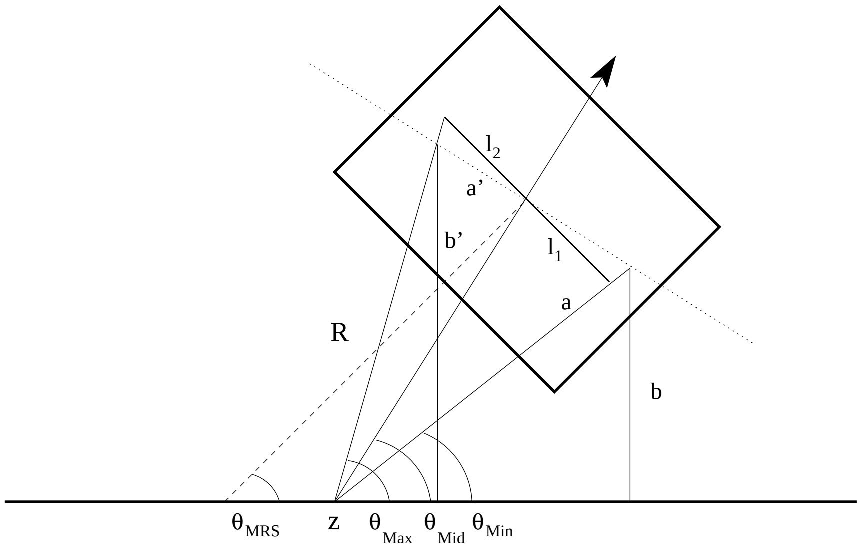

Figure 8.16: Definition of the variables used in calculating the η-acceptance of TPM1.

My track elevation will at most be 7 cm out of the xz–plane at the midplane of TPM1, and I get

$$r_{Track} = \sqrt{r_{xz}^2 + r_y^2} = \sqrt{95^2 + 7^2}cm = 95.26cm \approx 95cm \tag{8.24}$$

justifying this approximation.[10]

The analytical expressions for the maximum and minimum accepted track angles for a given vertex position z then become (see fig. 8.16):

$$\theta_{min} = tan^{-1}(\frac{b}{a}) \tag{8.25}$$

where

$$a = R \cdot cos(\theta_{MRS}) - z + l_1 \cdot sin(\theta_{MRS}) \tag{8.26}$$

$$b = R \cdot sin(\theta_{MRS}) - l_1 \cdot cos(\theta_{MRS}) \tag{8.27}$$

and

$$\theta_{max} = tan^{-1}(\frac{b'}{a'}) \tag{8.28}$$

[10]The effect of this approximation will in any case drown in the other systematic errors to be discussed in section 8.7.

θ_{MRS}	$\eta_{min}^{z=-15cm}$	$\eta_{max}^{z=-15cm}$	$\eta_{min}^{z=0cm}$	$\eta_{max}^{z=0cm}$	$\eta_{min}^{z=15cm}$	$\eta_{max}^{z=15cm}$
90	0.0517	0.2645	-0.1051	0.1051	-0.2645	-0.0517
60	0.5829	0.8280	0.4315	0.6745	0.2655	0.5109
40	1.1271	1.3359	0.9783	1.1854	0.8102	1.0173

θ_{MRS}	$\hat{\eta}$	$\hat{\Delta\eta}$
90	0	0.2119
60	0.5489	0.2445
40	1.0757	0.2077

Table 8.9: The η acceptance at different MRS angles θ_{MRS}

where

$$a' = R \cdot cos(\theta_{MRS}) - z - l_2 \cdot sin(\theta_{MRS}) \tag{8.29}$$

$$b' = R \cdot sin(\theta_{MRS}) + l_2 \cdot cos(\theta_{MRS}) \tag{8.30}$$

Here R=95cm, θ_{MRS} is the angle of the midrapidity spectrometer and

$$\theta_{mid} = tan^{-1}(\frac{R \cdot sin(\theta_{MRS})}{R \cdot cos(\theta_{MRS}) - z}) \tag{8.31}$$

As indicated in figure 8.16 and discussed in section 8.4.2 I impose a cut on the track position at the midplane of the TPC (l_1 and l_2 in the above equations) to avoid low–efficiency regions of the detector. The values are given in table 8.3, where l_1 and l_2 are the lower and upper x cuts respectively.

In my analysis I have accepted events with vertices within $z = \pm 15cm$, so this is the region I must calculate over. Table 8.9 shows the results for my three spectrometer angles, as well as the resulting average η interval for each setting. The variation in $\Delta\eta$ for different vertex positions is seen to be <1%.

A possible problem here is that a track coming from the vertex and crossing the midplane might be too steep to exit the backplane. This would be another vertex–dependent correction to the η acceptance. I have calculated this analytically, and for $\theta_{MRS} = 40^o$ the critical vertex position for this problem is around $z = 35cm$. For $\theta_{MRS} = 60^o$ it will naturally be even higher. Consequently, this is not a problem for my analysis.

ϕ correction

ϕ is defined as the azimuthal angle of the track at the z coordinate (along the beam) where it intersects the track midplane. This is different from the track's elevation from the x–z plane, an angle which I call α. I need ϕ since $dN/d\eta$

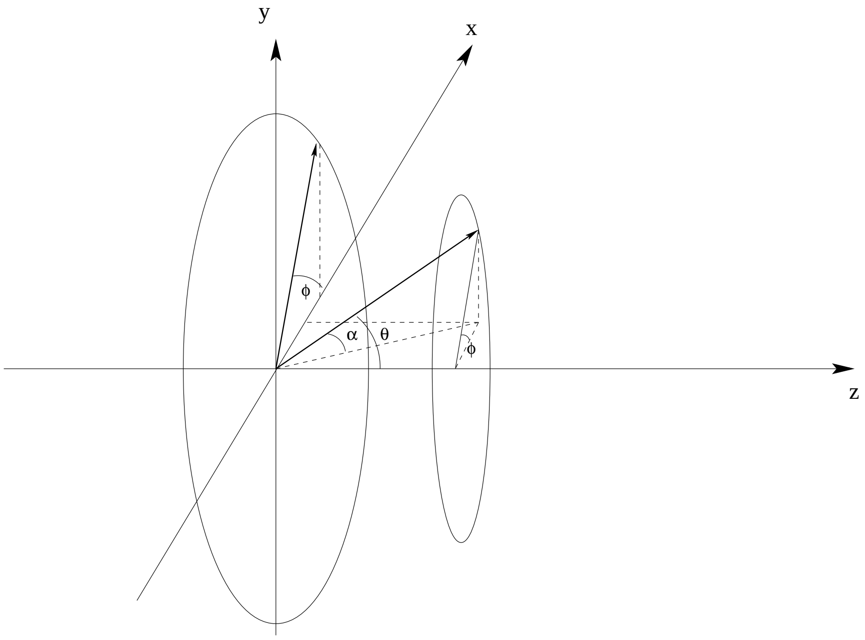

Figure 8.17: Definition of the variables used in calculating the ϕ-acceptance of TPM1. Notice that for $\theta = 90^o$ we get $\phi = \alpha$.

should be normalized to a circular region around the beam with a width of one unit of pseudorapidity. Simple geometry gives me that

$$\phi = tan^{-1}(\frac{tan(\alpha)}{sin(\theta)}) \tag{8.32}$$

where θ is the tracks polar angle angle (equivalent to the pseudorapidity, see eq. 3.13). See fig. 8.17.

The midplane of TPM1 is positioned at global $x = 95cm$ and the fiducial area of my tracks (see section 8.4.2) is $^{+7}_{-6}cm$. The acceptance in ϕ will depend on θ_{MRS}, but not on the position of the vertex. See table 8.10 for my calculated $\Delta\phi$ numbers, where I have used $\theta_{Min,Mid,Max}$ as calculated from eq. 8.25 – 8.31.

The total geometry correction factor

The total geometric acceptance factor, normalizing to one unit of pseudorapidity, can now be approximated as

$$f_{Geometry} = \frac{1}{\hat{\Delta\eta}} \cdot \frac{360}{\hat{\Delta\phi}} \tag{8.33}$$

I can do this since I can assume that $dN/d\eta$ is approximately constant over the cross–section of TPM1.

θ_{MRS}	$\Delta\phi_{\theta_{min}}$	$\Delta\phi_{\theta_{mid}}$	$\Delta\phi_{\theta_{max}}$	$\hat{\Delta\phi}$
90	7.8702	7.8702	7.8702	7.8702
60	9.6162	9.0344	8.5188	9.0565
40	13.8777	12.7877	11.8558	12.8404

Table 8.10: The ϕ acceptance at different MRS angles θ_{MRS}. All $\Delta\phi$ entries are in degrees. Note that θ_{mid} is different at 40^o because the cuts on the midplane are different (see tab. 8.3).

θ_{MRS}	$f_{Geometry}$
90	215.87
60	162.58
40	134.99

Table 8.11: The total geometric correction factor for TPM1, normalized to one unit of pseudorapidity, for the given θ_{MRS} and assuming a vertex fiducial area of $z = \pm 15cm$.

Table 8.11 gives the resulting $f_{Geometry}$ for the three MRS angles, assuming a vertex fiducial interval of $z = \pm 15cm$. See also figure 8.18, which is the total η vs. ϕ acceptance of TPM1 for $z = \pm 15cm$.

8.4.7 Centrality–dependent $dN/d\eta$

I can now calculate the corrected $dN/d\eta$ for each centrality bin and spectrometer angle. The resulting numbers are given in table 8.12 and plotted in figure 8.19.

We see a smooth decline in the amount of produced particles with centrality,

	$dN/d\eta$ per unit of η		
Cent. Class	90^o	60^o	40^o
1	553±4	557±6	579±4
2	438±3	452±5	475±4
3	350±3	358±5	381±3
4	281±3	285±4	311±3
5	200±2	198±3	223±3
6	120±1	126±2	140±2
7	73±1	73±2	85±1

Table 8.12: Charged particle production ($dN/d\eta$) normalized to one unit of pseudorapidity. The errors are statistical.

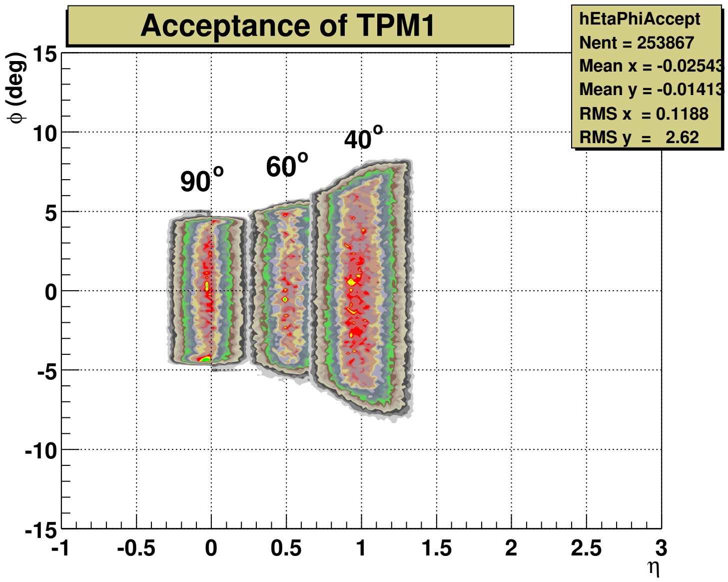

Figure 8.18: The measured acceptance of TPM1 in η and ϕ at $\theta_{MRS} = 90^o$, 60^o and 40^o.

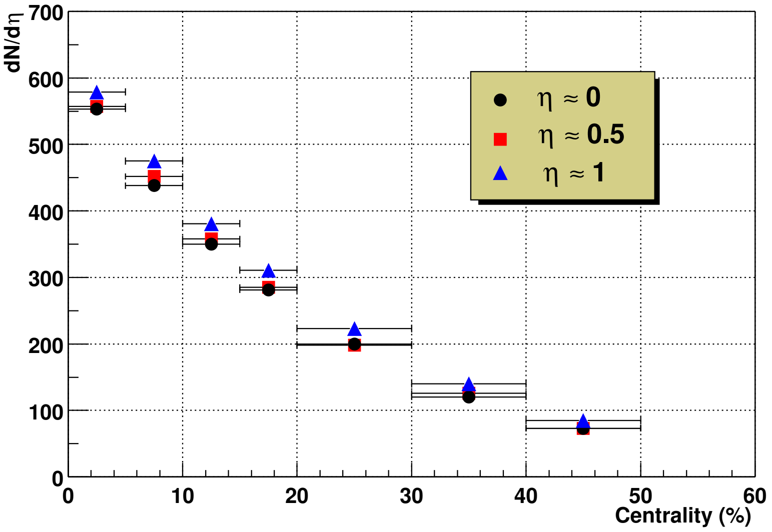

Figure 8.19: Centrality dependent $dN/d\eta$ at three spectrometer angles. The horizontal error bars indicate the size of the centrality classes. The statistical error bars are within the points.

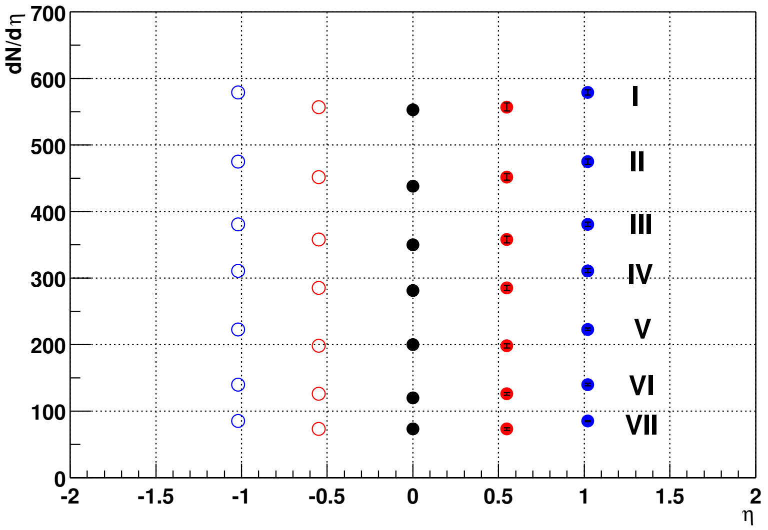

Figure 8.20: $dN/d\eta$ versus η from TPM1, for the seven centrality classes defined in table 8.1. The transparent points are reflected about $\eta = 0$. Statistical errors are within the points.

roughly equal for all three η values. This is natural since the system size and hence the amount of matter/energy in the collision decreases with centrality. To investigate this further I will below remove the dependency on system size by dividing out the number of participating nucleons.

Another, more interesting plot is shown in figure 8.20. Here we see the variation of $dN/d\eta$ with η for my seven centrality classes, and they all show a dip at midrapidity. I will discuss this further below, but for now I note that this is consistent with the behavior seen by the TMA and SMA as shown in fig. 8.2.

8.5 Estimating the number of participating nucleons

In addition to plotting $dN/d\eta$ versus centrality, one usually looks at $dN/d\eta$ per participant pair plotted versus the number of participating nucleons. The reason for this is that the wounded nucleon model predicts a particle production that scales only with $N_{Participants}$, so any deviation from this indicates physics beyond this simple picture.

To do this, I first need an estimate of the average number of participating nucleons in each of our centrality classes. There have been several calculations

Cent. class	$< N_{Part} >$
1	338
2	289
3	239
4	201
5	154
6	103
7	66

Table 8.13: The average number of participating nucleons in each centrality class. Numbers from ref. [64].

of this by different people in BRAHMS based on varying principles. I have chosen to use the numbers presented by H. Ito in ref. [64], since they are very closely connected with the centrality classes used above. However, the centrality selection algorithms have changed slightly since they were calculated, so these numbers may well be changed in the near future.

To calculate his numbers, H. Ito has first made a complete simulation of the Tile and Si-arrays using GEANT and particle data from HIJING. He then used cuts on the extracted multiplicity in Si+Tile, using the experimental analysis chain, on the output of the simulation to group the events in the different centrality classes, and calculates $< N_{Part} >$ for each class from the HIJING output. The results are shown in table 8.13.

I note that these numbers, at least for the most central bins, are lower than the ones used by Claus E. Jørgensen in his thesis[61]. I will take this into account in my calculation of systematic uncertainties below.

8.6 $dN/d\eta$ per number of participant pairs

In table 8.14, I have divided my $dN/d\eta$ numbers from table 8.12 by the number of participant pairs to remove the dependence on the system size. The results are also plotted in figure 8.21.

It is clear that there is an increase in the number of produced charged particles with the system size beyond a simple scaling with the number of wounded nucleons. The dependence seems to be the same for all my three η values. I will discuss this result further in section 8.10.

8.7 Systematic uncertainties

All the uncertainties presented above have been purely statistical. However, I also need to investigate several possible sources of systematic errors in my

	$\frac{dN}{d\eta}/\frac{1}{2}N_{Part}$		
Cent. Class	90^o	60^o	40^o
1	3.27±0.02	3.29±0.04	3.43±0.03
2	3.03±0.02	3.13±0.04	3.28±0.02
3	2.93±0.02	2.99±0.04	3.19±0.03
4	2.79±0.03	2.83±0.04	3.10±0.03
5	2.60±0.02	2.58±0.03	2.89±0.02
6	2.33±0.03	2.45±0.04	2.72±0.03
7	2.23±0.04	2.22±0.06	2.58±0.04

Table 8.14: $dN/d\eta$ normalized to one unit of pseudorapidity, per number of participant pairs. The errors are statistical.

measurements. A systematic error is an uncertainty in the bias of my data, such as those introduced by using a specific set of tracking parameters or using a specific cut on event selection.

Below, I will deal with the following sources of systematic errors:

- Tracking efficiency
- Tracking parameters
- Ghost correction
- Background subtraction
- Calculation of the number of participating nucleons
- Uncertainty in the measurement of the min. bias distribution

Other sources surely exist, but I believe these to be the major ones.

8.7.1 Tracking efficiency

The systematic error in the tracking efficiency has been estimated by varying the straight–line fit to the efficiency vs $N_{Clusters}$ plots discussed in sec. 8.4.3 within reasonable limits by visual inspection. See also fig. 8.11. By adjusting the fit within the error bars on the points I get the changes in efficiency shown in table 8.15, and inserting these values in my $dN/d\eta$ analysis gives me an estimated systematic error from tracking efficiency ranging from $\sim 5\%$ for central collisions to $\sim 1\%$ for peripheral. See table 8.17 for the exact values.

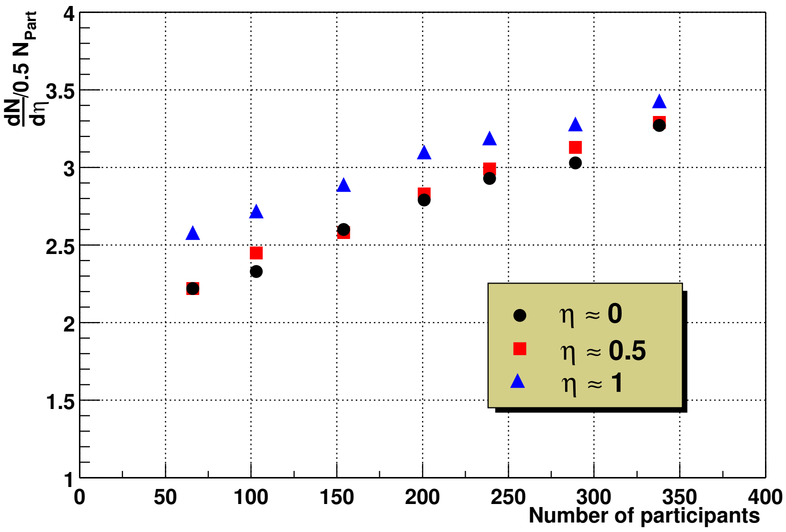

Figure 8.21: $dN/d\eta$ per number of participant pairs from TPM1 at three angles. The statistical error bars are within the points.

ϵ_{Fit}	ϵ_{Max}	ϵ_{Min}
$1.45 \cdot 10^{-4}$	$2.65 \cdot 10^{-4}$	$0.790 \cdot 10^{-4}$

Table 8.15: Changes in the average slope of efficiency vs. $N_{Clusters}$ when the fit is changed within the error bars.

8.7.2 Background subtraction

As mentioned in section 8.4.4, I make a cut in the allowed distance from the vertex the y–projection of a track at the beam–plane may have. I have set this cut at $3\sigma_{Signal}$, but since this is effectively a direct cut in the number of primary tracks it has a large impact on the result.

To take this into account, I vary the cut by $+\sigma_{Signal}$ and check the effects on my $dN/d\eta$ analysis. The change is constant for all centrality classes, and equal to +5%. Cutting down to $2\sigma_{Signal}$ is not correct, since that will cut into the very sharp signal peak and reduce my measurement by much more than the systematic error. I make the assumption that the systematic error is the same for both positive and negative variations, giving me

$$\delta^{Syst.}_{BGsubtr} = \pm 5\% \tag{8.34}$$

This is the major contribution to my systematic error.

8.7.3 Tracking parameters

The parameters I input to the clustering and tracking algorithms are in no way a priori given, and can have an effect on the number of tracks found. Examples here are what is the minimum ADC value required in a timebin to make a cluster, what is the search width of the TrackFollowFinder etc. I have run a series of tests using

- Clusterfinding parameters changed according to "cut 4" in [71], which removes most noise clusters by cutting on cluster widths and the minimum peak ADC value.
- **BrTrackFollowFinder** parameters changed within reasonable values.
- Used **BrTrackStringFinder** with default parameters.
- Used a new, crash–free version of **BrTrackFollowFinder** that was recently made by Peter Christiansen.

From these different analyses, I estimate a systematic effect of less than 3% on the final $dN/d\eta$ values for all centrality bins.

8.7.4 Ghost correction

Figure 8.13 has statistical uncertainties on its data points. By varying my ghost fraction for each bin within the error bars, I estimate

$$\delta^{Syst.}_{Ghostcorr.} \ll \pm 1\% \tag{8.35}$$

This effect is negligible relative to the effects described above, so I choose to disregard it in the final analysis. Note that I have also assumed that $N_{Ghostspcacings} = N_{Ghosttracks}$ (see sec. 8.4.5 above), and again I assume that the effect of this on the final result is <1%.

8.7.5 Errors in $N_{Participants}$

To remove the dependency of $dN/d\eta$ I divide by the number of participating nucleons. This number is however very uncertain, since it is not directly measurable and depends both on model parameters and the method used to select centrality. One can either use a model output directly, or one can simulate the response of ones detectors, see which simulated events fall in each centrality class according to the same cuts that are used on experimental data and get the average N_{Part} from those.

The numbers I quoted in table 8.13 above were calculated in the latter way in [64], using HIJING as an input. Claus E. Jørgensen has made a similar analysis

Centrality Cut [%]	Approximate b range [fm]	$\langle N_{part} \rangle$ (HIJING)	$\langle N_{part} \rangle$ (FRITJOF)	$\langle N_{part} \rangle$ (Glauber[16])
0 - 10	0 - 5	329.2	321.7	316
10 - 20	5 - 7	233.8	230.0	223
20 - 30	7 - 8.5	163.3	162.9	154
30 - 40	8.5 - 10	108.6	111.8	102
40 - 50	10 - 11	70.0	72.9	63

Table 8.16: Centrality cuts with corresponding impact parameter range and average number of participants. Table from [61].

in his thesis using HIJING and FRITJOF, and also includes pure Glauber–model numbers quoted in [16]. His numbers are slightly different than the ones from [64] since he uses an alternative centrality selection — see table 8.16. I will take the spread in these values as the primary systematic error on my N_{Part} numbers — see table 8.18.

In addition, there is an uncertainty related to how well we really measure the min–bias distribution. If we are e.g. inefficient at selecting the most peripheral events, this will have a significant impact on the centrality selection. From comparisons with simulations BRAHMS claims to measure 99% of the total $Au - Au$ cross–section, and in an upcoming publication on our measured $\frac{\bar{p}}{p}$ ratio [14] we estimate a systematic uncertainty of 2% on this measurement. I include the effect of this error on N_{Part} in table 8.18 and in the calculations below.

8.7.6 Total systematic errors

In tables 8.17 and 8.18 I sum up all the contributions discussed above, and calculate a total systematic uncertainty for my numbers using a squared sum approach. My final $dN/d\eta$ and $\frac{dN}{d\eta}/0.5 \cdot N_{Part}$ results are shown in tables 8.19 and 8.20.

8.8 Comparison with GEANT simulations

An important test of any data analysis is that it should be able to reproduce a given simulated input. To test this, I have run a small sample of very central HIJING events through digitization plus my entire analysis and calculated $dN/d\eta^{Sim}$ at $\theta_{MRS} = 90^o$.

One change had to be made from the procedure described above, and that is the background subtraction. The GEANT simulation that I have does not treat delta electrons properly and also lacks some of the dense material close to the

Cent. Class	Track. Eff.	Back. subtr.	Tracking par.	Total
1	$^{+7\%}_{-4\%}$	$\pm5\%$	$\pm3\%$	$^{+9\%}_{-7\%}$
2	$^{+6\%}_{-3\%}$	$\pm5\%$	$\pm3\%$	$^{+8\%}_{-7\%}$
3	$^{+5\%}_{-3\%}$	$\pm5\%$	$\pm3\%$	$^{+8\%}_{-7\%}$
4	$^{+4\%}_{-2\%}$	$\pm5\%$	$\pm3\%$	$^{+7\%}_{-6\%}$
5	$^{+4\%}_{-2\%}$	$\pm5\%$	$\pm3\%$	$^{+7\%}_{-6\%}$
6	$^{+3\%}_{-2\%}$	$\pm5\%$	$\pm3\%$	$^{+7\%}_{-6\%}$
7	$^{+1\%}_{-1\%}$	$\pm5\%$	$\pm3\%$	$^{+6\%}_{-6\%}$

Table 8.17: Summary table of systematic uncertainties on my $dN/d\eta$ measurement.

Cent. Class	From $dN/d\eta$	Model dep.	Min–bias	Total
1	$^{+9\%}_{-7\%}$	$^{+5\%}_{-0\%}$	$\pm0.1\%$	$^{+10\%}_{-7\%}$
2	$^{+8\%}_{-7\%}$	$^{+5\%}_{-0\%}$	$\pm0.5\%$	$^{+9\%}_{-7\%}$
3	$^{+8\%}_{-7\%}$	$^{+6\%}_{-0\%}$	$\pm0.8\%$	$^{+10\%}_{-7\%}$
4	$^{+7\%}_{-6\%}$	$^{+6\%}_{-0\%}$	$\pm1\%$	$^{+9\%}_{-6\%}$
5	$^{+7\%}_{-6\%}$	$^{+6\%}_{-0\%}$	$\pm2\%$	$^{+9\%}_{-6\%}$
6	$^{+7\%}_{-6\%}$	$^{+9\%}_{-1\%}$	$\pm3\%$	$^{+12\%}_{-7\%}$
7	$^{+6\%}_{-6\%}$	$^{+10\%}_{-5\%}$	$\pm5\%$	$^{+13\%}_{-9\%}$

Table 8.18: Summary table of systematic uncertainties on my $\frac{dN}{d\eta}/0.5 \cdot N_{Part}$ measurement.

beampipe that produces background. In addition the TPC is much less noisy in simulations, which also reduced the background contribution. The result is that my two–Gaussian background fit is not as correct as for real data, though the general shape of the background is the same. Instead I have used the fact that in simulated data I know what tracks are primary and used

$$f_{Background} = \frac{N_{Secondaries}}{N_{Total}} \tag{8.36}$$

to correct for the background ratio. I set the cut to be a sphere around the GEANT vertex, analog to a method used in [64].

The output from this analysis is

$$dN/d\eta^{Out} = 595 \tag{8.37}$$

while HIJING with our parameters predicts

$$dN/d\eta^{In} = 601 \tag{8.38}$$

	$dN/d\eta$ per unit of η		
Cent. Class	90^o	60^o	40^o
1	$553\pm4^{+50}_{-39}$	$557\pm6^{+50}_{-39}$	$579\pm4^{+52}_{-41}$
2	$438\pm3^{+35}_{-31}$	$452\pm5^{+36}_{-32}$	$475\pm4^{+38}_{-33}$
3	$350\pm3^{+28}_{-24}$	$358\pm5^{+29}_{-25}$	$381\pm3^{+30}_{-27}$
4	$281\pm3^{+20}_{-17}$	$285\pm4^{+20}_{-17}$	$311\pm3^{+22}_{-19}$
5	$200\pm2^{+14}_{-12}$	$198\pm3^{+14}_{-12}$	$223\pm2^{+16}_{-13}$
6	$120\pm1^{+8}_{-7}$	$126\pm2^{+9}_{-8}$	$140\pm2^{+10}_{-8}$
7	$73\pm1^{+4}_{-4}$	$73\pm2^{+4}_{-4}$	$85\pm1^{+4}_{-4}$

Table 8.19: Charged particle production ($dN/d\eta$) normalized to one unit of pseudorapidity, including statistical and systematic errors.

	$\frac{dN}{d\eta}/0.5 \cdot N_{Part}$ per unit of η		
Cent. Class	90^o	60^o	40^o
1	$3.27\pm0.02^{+0.33}_{-0.23}$	$3.29\pm0.04^{+0.33}_{-0.23}$	$3.43\pm0.03^{+0.34}_{-0.24}$
2	$3.03\pm0.02^{+0.27}_{-0.21}$	$3.13\pm0.04^{+0.28}_{-0.22}$	$3.28\pm0.02^{+0.30}_{-0.23}$
3	$2.93\pm0.02^{+0.29}_{-0.20}$	$2.99\pm0.04^{+0.30}_{-0.20}$	$3.19\pm0.03^{+0.32}_{-0.22}$
4	$2.79\pm0.03^{+0.25}_{-0.17}$	$2.83\pm0.04^{+0.26}_{-0.17}$	$3.10\pm0.03^{+0.28}_{-0.19}$
5	$2.60\pm0.02^{+0.23}_{-0.16}$	$2.58\pm0.03^{+0.23}_{-0.15}$	$2.89\pm0.02^{+0.26}_{-0.17}$
6	$2.33\pm0.03^{+0.28}_{-0.16}$	$2.45\pm0.04^{+0.29}_{-0.17}$	$2.72\pm0.03^{+0.32}_{-0.19}$
7	$2.22\pm0.04^{+0.29}_{-0.20}$	$2.22\pm0.06^{+0.29}_{-0.20}$	$2.58\pm0.04^{+0.33}_{-0.23}$

Table 8.20: Charged particle production ($dN/d\eta$) per number of participant pairs, normalized to one unit of pseudorapidity. Includes statistical and systematic errors.

i.e. the analysis reproduces the model input to within 1%. This gives us confidence in that we understand the output of our detectors and that the analysis is correct in all major respects.

8.9 Comparison with other measurements

Several other $dN/d\eta$ measurements have been made from year–one RHIC data, both by other BRAHMS collaborators and the PHENIX and PHOBOS collaborations. I will below compare their numbers to mine.

8.9.1 The BRAHMS globals

The BRAHMS global detectors, BB and the TMA/SMA barrel, have produced a continuous $dN/d\eta$ measurement out to $|\eta| = 4$ from the year one BRAHMS

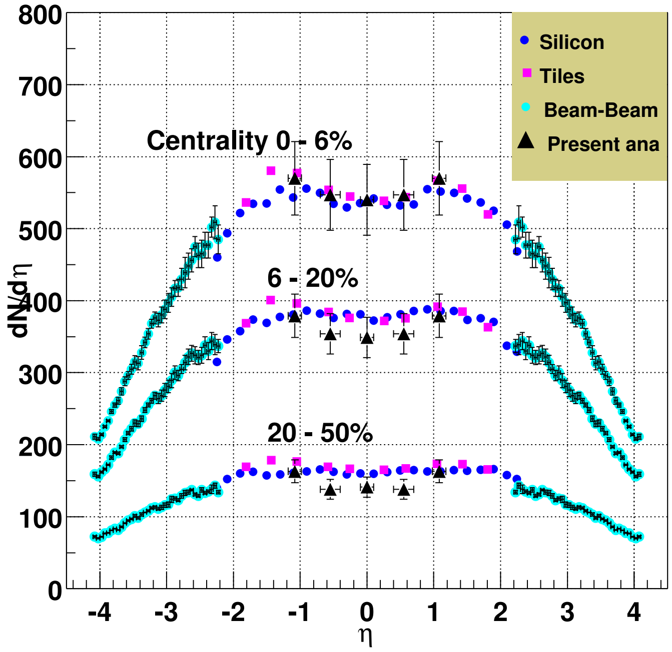

Figure 8.22: $dN/d\eta$ from TPM1, compared with the BRAHMS global detectors. The black triangles are the present analysis, reflected about $\eta = 0$. Error bars include statistical and systematic errors.

data. Figure 8.22 shows their numbers compared to the TPM1 measurement presented above.

The version of the numbers presented here is slightly outdated, being made with a different version of the centrality selection code. New numbers, calculated for the official BRAHMS centrality classes (see app. A), are due out at any time but did not reach me in time to be included here. This change will probably not affect the numbers much, at most a few percent.

My numbers are seen to follow the shape measured by the globals nicely. I have reflected the numbers about $\eta = 0$ to better show this. For 0–5% central events my numbers overlap perfectly with the TMA/SMA numbers, while for more peripheral collisions the TPM1 numbers end up low relative to the globals. The relative difference seems correlated with the centrality.

The global numbers do not yet have systematic errors included. I believe the measurements will be consistent when these are plotted in, and there is also a possibility that the TMA/SMA numbers will drop slightly when calculated with the newest centrality code.

Still, within systematic errors the measurement I have presented is consistent with that from the global BRAHMS detectors at all centralities. This is as

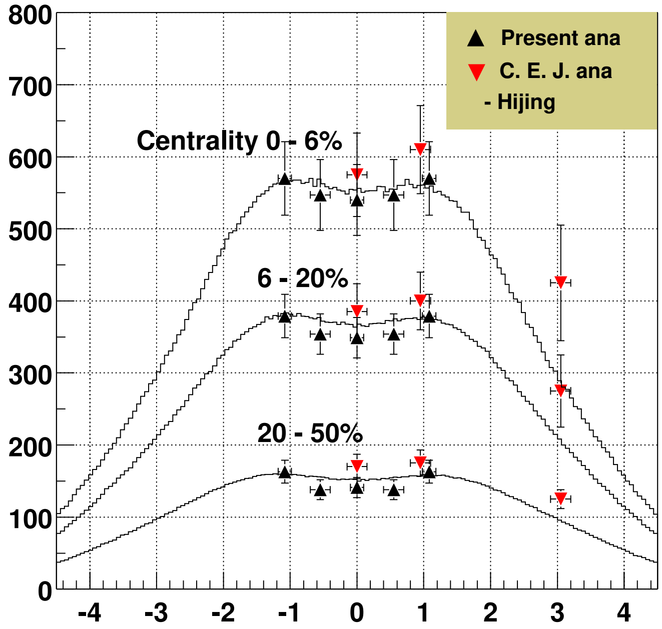

Figure 8.23: $dN/d\eta$ from TPM1, compared with predictions from HIJING and the analysis made by Claus E. Jørgensen in [61]. My points are reflected about $\eta = 0$. Error bars include statistical and systematic errors.

expected, since the only difference in what the detectors measure comes from the fact that TPM1 is positioned $\sim 70cm$ further from the beamline than the mult barrel. This means a $\sim 2ns$ longer flight time for the produced hadrons, and a portion of them will have undergone weak decays. From a related discussion in [61] based on GEANT simulations this effect can be estimated to be on the order of $\leq 2\%$, i.e. much lower than my quoted systematic errors.

8.9.2 Another TPM1 analysis

As indicated above, Claus E. Jørgensen from NBI has recently published a Master thesis on the same analysis as I have just presented. His numbers are shown relative to mine in 8.23. Our analyses are quite similar, but we use different methods of centrality selection — see [61] for details. We also calculate acceptance, background and efficiency corrections slightly differently.

Claus' numbers are somewhat higher than mine, but well consistent within systematic errors. This lends credibility to the total $dN/d\eta$ extracted from TPM1.

8.9.3 PHENIX and PHOBOS

Two of the first publications on RHIC physics were about $dN/d\eta$ measurements. In [36] the PHOBOS collaboration present a single point for 0-6% central collisions (though for two collision energies), and in [37] the PHENIX collaboration present a full centrality–dependent $dN/d\eta$ at $\eta = 0$.

In figure 8.24 I compare their numbers to mine, both as "raw" $dN/d\eta$ numbers (top) and with the system size dependency divided out (bottom). The PHOBOS measurement is almost identical to the one I have presented, but the PHENIX numbers are significantly higher than mine. Note though that systematic errors have not been plotted for the PHENIX points — if they were the numbers would just barely be consistent. At Quark Matter 2001 the PHOBOS collaboration also presented a full centrality dependent $dN/d\eta$ at $\eta = 0$ — see [52]. Since they are preliminary I have not plotted these numbers, but they are again almost identical to what I have presented above.

In the bottom panel of figure 8.24 I have also plotted the point for pp collisions at $\sqrt{s} = 130GeV$ (extrapolated from UA(5) data [72]). Since this represents a collision with two participants, one would expect a plot of $dN/d\eta$ per participant pair vs. N_{Part} to extrapolate to this point either smoothly or with some discontinuities. A straight line fit to my points crosses the y axis slightly below this point, but within the systematic errors $dN/d\eta$ from TPM1 is consistent with a smooth rise in $dN/d\eta$ per participant pair from 2 to 388 participating nucleons. The PHENIX numbers also extrapolate well to the pp point, but they see a "kink" in the distribution at ~ 150 participants.

8.10 Discussion

Having presented my analysis, I will discuss some points that may be extracted from it.

8.10.1 Total particle production

Throughout this presentation, I have consistently used $dN/d\eta$ where I should have used $dN_{ch}/d\eta$ since charged particles are what I measure. As presented in section 8.1, one can to a good approximation say that

$$\frac{dN}{d\eta} \approx \frac{3}{2}\frac{dN_{Charged}}{d\eta} \tag{8.39}$$

From this equation I can calculate the approximate total number of produced particles per unit of pseudorapidity. The resulting numbers for 0–5% central collisions is shown in table 8.21.

The total production of particles, for all pseudorapidities, can be extracted from the full $dN/d\eta$ distribution by extrapolating it smoothly to large η and

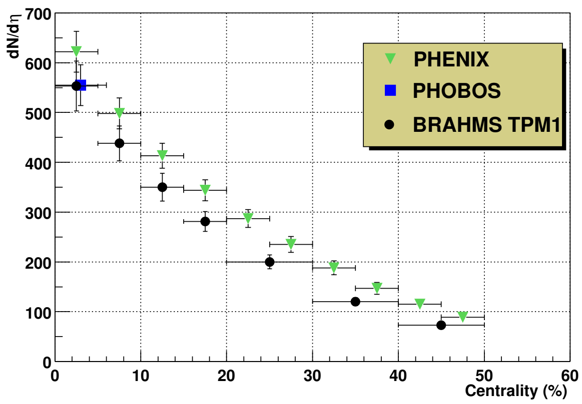

(a) $dN/d\eta$ vs centrality

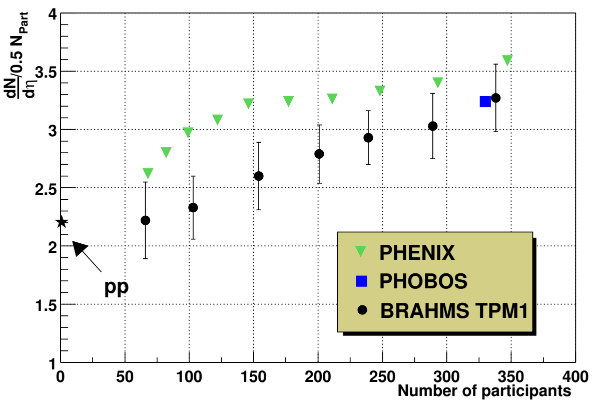

(b) $dN/d\eta$ per participant pair

Figure 8.24: $dN/d\eta$ from TPM1 at $\eta = 0$, compared with measurements published by the PHENIX [37] and PHOBOS [36] collaborations. The relevant point from *pp* collisions (UA5) is also shown.

η	0	0.5	1.1
$\frac{dN}{d\eta}^{Tot}$	830	836	869

Table 8.21: The approximate total number of produced particles per unit of pseudorapidity, for 0–5% central collisions.

integrating. The preliminary value from the BRAHMS globals is

$$N_{ch} = 4050 \pm 200 \rightarrow N_{tot} = 6075 \pm 300 \tag{8.40}$$

Claus E. Jørgensen has made a comparison of this number with values from the SPS and also a beam energy dependence analysis in [61]. I will not repeat his work, but rather refer the reader to his plots and numbers.

8.10.2 Model comparisons

$dN/d\eta$ predictions

Having presented a measurement, it is of course interesting to see how it compares with model predictions. Please refer to section 3.4 for details about the specific models.

In figure 8.23 I have plotted the HIJING prediction for $Au - Au$ collisions at $\sqrt{s} = 130GeV$ for the various centralities together with my numbers, and it is apparent that this model well predicts the measurement from TPM1.

In figure 8.25 I show predictions on $dN/d\eta$ and $\frac{dN}{d\eta}/0.5 \cdot N_{Part}$ from other models. From the top panel, it is clear that unlike HIJING both UrQMD and FRITJOF strongly overpredict the charged particle density at midrapidity. (The points in this figure are older BRAHMS measurements and not from the present analysis, but still consistent with the latest results.) This indicates both one of the most basic hadronic transport models available and the most sophisticated field theory based model overpredict the energy deposit at midrapidity, which can naively be taken to be proportional to the baryon stopping.

In the bottom panel of figure 8.25 I have plotted my numbers for $\frac{dN}{d\eta}/0.5 \cdot N_{Part}$ at $\eta = 0$ compared to HIJING and the EKRT saturation model. Again HIJING seems to well describe my measurement, while EKRT predicts a dependency with a slope of the wrong sign. However, the QCD saturation picture has never been thought to be relevant for other than the most central collisions at RHIC (see e.g. [31]), so the fact that it predicts a value very close to my measurement in the most central bin is actually a good sign for this model. It will be very interesting to see how its predictions compare to ALICE data at $\sqrt{s} = 6.3ATeV$, where saturation is predicted to play a much larger role.

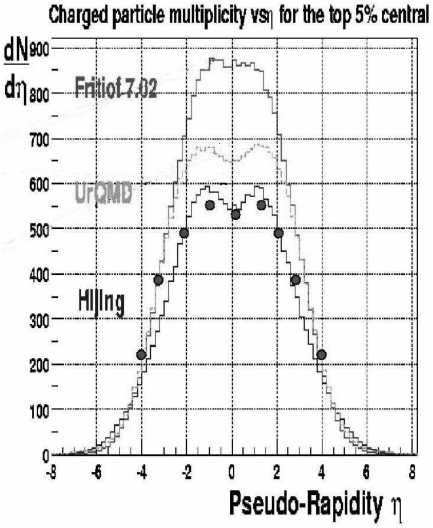

(a) $dN/d\eta$

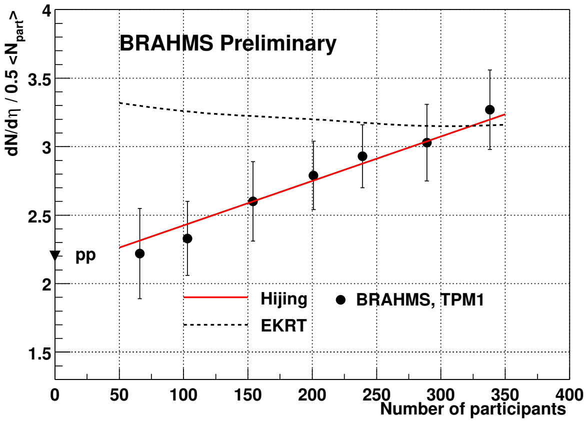

(b) $\frac{dN}{d\eta}/0.5 \cdot N_{Part}$

Figure 8.25: Model predictions of $dN/d\eta$ (tob) and $\frac{dN}{d\eta}/0.5 \cdot N_{Part}$ (bottom) for $Au-Au$ collisions at $\sqrt{s} = 130GeV$. The points on the left panel are old BRAHMS numbers, not the present analysis.

HIJING physics

As shown in figure 8.23, my numbers are consistent with the predictions of the HIJING model. This makes it interesting to review the physics of this model.

In recent reviews of event generator predictions of $dN/d\eta$ at RHIC energies [30, 73] HIJING is seen to give one of the lowest numbers. To achieve this, the model includes two effects that explicitly alter the particle production — jet quenching and nuclear shadowing. The first reduces p_T for minijets and may slightly increase particle production due to increased energy deposition at midrapidity, while the second explicitly lowers $dN/d\eta$ by giving the projectile partons fewer target partons to collide with. See sec. 3.4.4. Both of these effects are included in the simulation shown in figure 8.23.

Using the data from the global detectors, we can also compare the total width of the $dN/d\eta$ distribution with HIJINGs prediction — see the summary figure 9.1 on page 148. It is clear that HIJING underpredicts the FWHM[11] of the distribution for all centralities.

Recall that the width of this distribution is naively inversely proportional to the NN cross section. If the nucleons are transparent σ_{NN} is small and they do not interact much, leading to a wide $dN/d\eta$ of produced particles. On the other hand, if the nucleons experience a high degree of stopping — i.e. have a high σ_{NN} — the $dN/d\eta$ distribution will be piled up at midrapidity and consequently narrower. That HIJING underpredicts the width of this distribution may indicate that it overpredicts the baryon stopping in $Au - Au$ collisions at $\sqrt{s} = 130GeV$. The same is the case for FRITJOF and UrQMD.

However, if we look at $\bar{p}/p$ ratio predicted by HIJING compared to numbers from a BRAHMS publication recently submittet to Phys. Rev. Lett. [14], the model overpredicts this measurement by $\sim 25\%$. See fig. 8.26. Since a $\bar{p}/p$ ratio closer to one indicates less stopping (closer to the transparent Bjorken limit), this contradicts the former conclusion based on the width of the inclusive $dN/d\eta$ distribution. On the other hand, the classical string based FRITJOF, with a higher degree of stopping, seems to predict the numbers quite well. To resolve this inconsistency it is necessary to meausre the full net baryon rapidity distribution, which gives direct, qualitative information on the degree of stopping.

Conclusions

The conclusion so far is that while pQCD–based HIJING correctly predicts charged hadron production at midrapidity for $\sqrt{s} = 130GeV$ and string–based, hadronic FRITJOF predicts the $\bar{p}/p$ ratio, none of the most common models can yet consistently predict several of the first results from RHIC. That no one model is yet sophisticated enough to do this is no surprise, but rather gives

[11] FWHM = Full Width Half Maximum

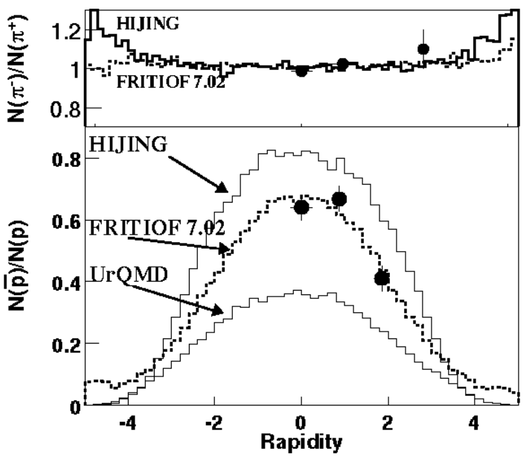

Figure 8.26: The $\bar{p}/p$ ratio for $Au - Au$ collisions at $\sqrt{s} = 130GeV$ as measured by BRAHMS, compared with event generator predictions. From [14].

hope that as more RHIC physics is published we can use the strengths of each model to get a better understanding of the (hopefully) deconfined matter we are studying.

8.10.3 Systematics of baryon stopping

The *nuclear stopping power* is the degree of stopping that an incident nucleon suffers when colliding with a nucleus, and can be estimated by the shift of the rapidity distributions of the incoming nucleons towards midrapidity. As mentioned above, the shape of the baryon rapidity distribution after a collision is seen as a good signal for the onset of new physics, since it is closely related to the baryon–baryon cross section and thus to reaction mechanisms.

At intermediate energies we expect a pile–up of produced particles around midrapidity because of a high degree of stopping. (The Landau scenario — see sec. 3.3.2.) As the CM energy increases we hope to see a gradual transition to the Bjorken limit of full nuclear transparency — the creation of an "excited vacuum". This will show itself first as a widening plateau in the $dN/d\eta$ distribution at midrapidity, gradually evolving into a "double–Gaussian" shape with a "dip" at the CM rapidity.

In pp collisions this transition is well documented by e.g. the UA5 collaboration (see e.g. [72]). Already at $\sqrt{s} = 56GeV$ there is a clear plateau at midrapidity in inclusive charged hadron rapidity distributions, widening to a very clear dip at energies ranging up to $0.9TeV$.

The same is true for the rapidity spectra of protons from central AA collisions studied at the AGS and SPS — see the left panel of figure 8.27. The AGS data at $\sqrt{s} = 10.8AGeV$ (open triangles) follow a wide Gaussian distribution

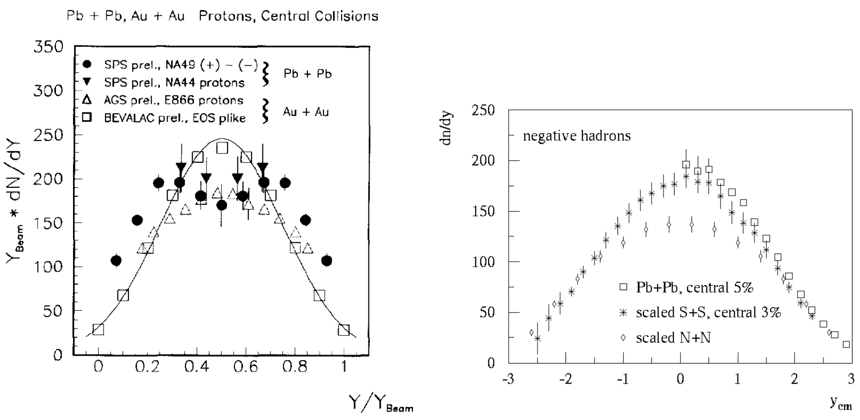

(a) Protons (b) AA

Figure 8.27: Stopping of a) Protons. Data compiled by the NA49 collaboration at the SPS.[74] b) All charged hadrons, $\sqrt{s} = 17.3AGeV$. Data from [75]

with maybe a hint of a plateau, while the SPS data at $\sqrt{s} = 17.3AGeV$ are clearly double–Gaussian with a dip. Clearly there is a transition to a transparent regime for the incident protons between these energies, probably close to or even at the AGS energies [79].

For full $dN/d\eta$ distributions from AA collisions, however, such a transition had not yet been seen. See the right panel of figure 8.27, which shows data from NA49 at $\sqrt{s} = 17AGeV$. The distribution is again a wide Gaussian with a hint of a plateau.

For the numbers I have presented above, however, the trend is that $dN/d\eta$ rises with increasing $|\eta|$, and looking at the full BRAHMS measurement in figure 8.22 we see a clear dip at midrapidity for central collisions. This result, which is backed by a similar, unpublished result from the PHOBOS collaboration [52], is the first measurement of a transition to a transparency regime with a Bjorken–like emitting source so extended in rapidity that the inclusive $dN/d\eta$ spectrum has evolved into a double–Gaussian. This clearly indicates the onset of new physics in the energy regime between SPS and RHIC, and in the coming years RHIC will study this transition extensively.

Looking again at the top panel of figure 8.25 it is clear that HIJING and UrQMD both predict the observed behaviour, while FRITJOF does not. However, as shown e.g. in the left panel of figure 8.28 [30], the depth of the predicted dip is very dependent on the parametrization of nuclear shadowing used in the model (EKS and HIJ in the figure). The presence of jet quenching also seems to reduce the dip. Note that this figure is for $\sqrt{s} = 200AGeV$. This may indicate that the width of the plateau at midrapidity is very sensitive to the details of

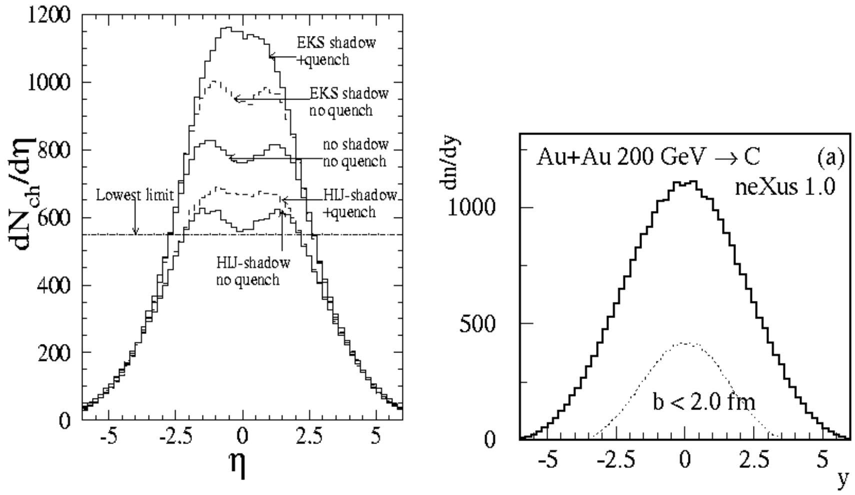

(a) HIJING (b) neXus

Figure 8.28: $dN/d\eta$ for $Au - Au$ collisions at $\sqrt{s} = 200AGeV$ from a) HIJING and b)neXus. Figures are from [30].

the reaction mechanisms.

In the right panel of figure 8.25 I show the predictions, still at $\sqrt{s} = 200AGeV$, from the neXus model [30]. Here we see no indication at all of a transition to the Bjorken scenario and a $dN/d\eta$ which is probably somewhat too high, which indicates that this universality model currently does not treat stopping and energy deposition at midrapidity correctly.

8.10.4 The ratio of hard scatterings

At the AGS and SPS, the production of charged particles at midrapidity was approximately described in the framework of the wounded nucleon model, which assumes that

$$\frac{dN}{d\eta} \propto N_{Wounded} = N_{Participants} \tag{8.41}$$

See e.g. [76]. There are some reported deviations from this scaling — e.g. in [77] the WA98 collaboration report a dependency that is well described by $dN/d\eta \propto (N_{Part})^{1.08}$. This shows that even at SPS energies the pure wounded nucleon scaling is slightly violated.

A fit to my numbers

As the $\sqrt{s}$ energy increases, it is predicted that parton–parton scatterings transferring $p_T \gg \Lambda_{QCD}$ will start to become important for the hadron production — i.e. processes that can be considered perturbatively. If this is so, then one can predict that the charged particle production will have one component scaling with N_{Part} and one scaling with the number of binary collisions N_{Coll}:

$$\frac{dN}{d\eta} = A \cdot N_{Part} + B \cdot N_{Coll} \tag{8.42}$$

If one has an estimate of $< N_{Part} >$ and $< N_{Coll} >$, and in addition a $dN/d\eta$ measurement, one can fit this functional to extract A and B and then calculate the fraction of produced hadrons due to hard and soft processes as

$$F_{Soft} = \frac{AN_{Part}}{dN/d\eta} \tag{8.43}$$

$$F_{Hard} = \frac{BN_{Coll}}{dN/d\eta} \tag{8.44}$$

This is again interesting because it can tell us much about the reaction mechanisms in an ultrarelativistic heavy–ion collision.

In [16] Kharzeev and Nardi (K&N) calculate $< N_{Part} >$ and $< N_{Coll} >$ for $Au - Au$ collisions at $\sqrt{s} = 130GeV$ from a pure Glauber model.[12] Our $< N_{Part} >$ numbers (see table 8.13 are slightly different, and I here make the assumption that to estimate our $< N_{Coll} >$ I can scale K&Ns numbers by this difference. The result is shown in table 8.22.

I am now in a position to fit my measured $dN/d\eta$ and extract values for A and B. The fit is shown in figure 8.29 and the numbers with errors are shown in table 8.24. The errors are calculated by varying the data points within their error bars. Note that the errors on A and B are anticorrelated. In table 8.23 I show the resulting values of F_{Hard} ($F_{Soft} = 1 - F_{Hard}$) for three values of η. There is a variation of $\sim 15\%$ from central to peripheral events, and a significant drop from $\eta = 0.55$ to $\eta = 1.1$.

It is interesting to compare my result at $\eta = 0$ to a similar fit made by the PHENIX collaboration in [37] to the data shown in figure 8.24. They report $A = 0.88 \pm 0.28$, $B = 0.34 \mp 0.12$ for $\eta = 0$. An exact comparison is not easy since both $< N_{Part} >$ and $< N_{Coll} >$ are extremely model dependent — e.g. for the most central bin PHENIX report a number of collisions $\sim 10\%$ lower than the one I have taken from [16] — but I can at least make an order–of–magnitude

[12] In [16] the numbers are actually given in integrated centrality bins, so I have had to assume a linear dependence of $< N_{Part} >$ and $< N_{Coll} >$ on centrality within each class to calculate the numbers I will use. See [69] for more details of this calculation.

Cent. class	$< N_{Part} >$	$< N_{Coll} >$
1	338	1032
2	289	827
3	239	638
4	201	512
5	154	351
6	103	203
7	66	106

Table 8.22: The average number of participating nucleons and binary collisions in each centrality class. $< N_{Part} >$ are from [64], $< N_{Coll} >$ are scaled from Glauber numbers given in [16].

Cent. class	$F_{Hard}^{\eta=0}$	$F_{Hard}^{\eta=0.55}$	$F_{Hard}^{\eta=1.1}$
1	0.77	0.76	0.57
2	0.77	0.75	0.56
3	0.75	0.73	0.54
4	0.75	0.74	0.53
5	0.72	0.73	0.50
6	0.79	0.66	0.46
7	0.60	0.60	0.40

Table 8.23: Fractions of the inclusive charged hadron production that are due to hard processes, extracted from a fit to $dN/d\eta$ from TPM1.

assessment. Their value for A is much higher than mine, as one could expect from their higher absolute numbers, but their B value is actually consistent with mine within errors. This value roughly determines the slope of the fit as it is plotted in fig. 8.29, and the consistency indicates that we see roughly the same amount scaling with $< N_{Coll} >$ independent of our different in absolute $dN/d\eta$ numbers. For $\eta = 0$ the PHENIX measurement gives an $F_{Hard}^{\eta=0}$ ranging from ~ 0.50 at central collisions to ~ 0.30 at $N_{Part} = 68$, i.e. somewhat lower than my numbers. This is because of their lower $< N_{Coll} >$ — using their values my F_{Hard} would be consistent with theirs within systematic errors.

An eikonal approach

In [16] K&N present an alternative way of calculating F_{Hard} based on an eikonal formalism.

Let n_{pp} be the charged multiplicity seen per unit of pseudorapidity in pp collisions, and let x be the fraction of this multiplicity that is due to "hard" or perturbative processes. We can then set up an eikonal equation for the charged

η	A	B
0	$0.36^{-0.11}_{+0.03}$	$0.41^{+0.09}_{-0.04}$
0.55	$0.37^{-0.06}_{+0.02}$	$0.41^{+0.09}_{-0.04}$
1.1	$0.73^{-0.01}_{+0.02}$	$0.32^{+0.05}_{-0.05}$

Table 8.24: A fit of $\frac{dN}{d\eta} = A \cdot N_{Part} + B \cdot N_{Coll}$ to the numbers from TPM1. Errors are estimated by varying the data points within their error bars. Notice that the errors on A and B are anticorrelated.

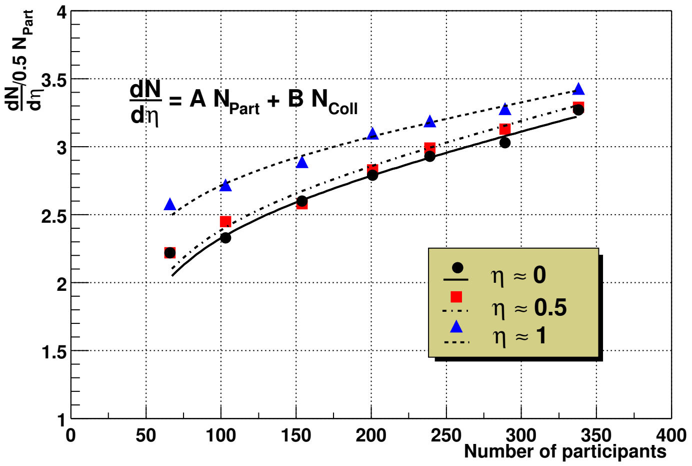

Figure 8.29: Results from TPM1 fitted with $\frac{dN}{d\eta} = A \cdot N_{Part} + B \cdot N_{Coll}$. Values for A and B are given in table 8.24

particle production in AA collisions:

$$\frac{dN}{d\eta} = (1-x)n_{pp}\frac{< N_{Part} >}{2} + xn_{pp} < N_{Coll} > \tag{8.45}$$

Again using model calculations of $< N_{Part} >$ and $< N_{Coll} >$ plus a measurement of $dN/d\eta$ we can solve this equation for x, and then calculate the absolute fraction of produced hadrons due to hard processes as

$$F^{K\&N}_{Hard} = \frac{xn_{pp}N_{Coll}}{dN/d\eta} \tag{8.46}$$

This approach is of course again very model dependent and relies on a rather simplistic assumption of scaling from pp to AA collisions, but it can at least give an order–of–magnitude estimate.

For $\sqrt{s} = 130AGeV$ the value of n_{pp} at $\eta = 0$ is [78]

$$n^{130AGeV}_{pp} = 2.25 \tag{8.47}$$

Cent. class	x	$F^{K\&N}_{Hard}$
1	0.089	0.37
2	0.074	0.31
3	0.070	0.29
4	0.059	0.24
5	0.043	0.17
6	0.012	0.05
7	0.0076	0.03

Table 8.25: Fractions F of the charged hadron production produced by hard scatterings in $Au - Au$ collisions at $\sqrt{s} = 130AGeV$. Method taken from [16].

Using the values for $< N_{Part} >$ and $< N_{Coll} >$ in table 8.22 I can calculate F from my numbers at $\eta = 0$. See table 8.25.

While remembering that these numbers are *very* model dependent, it is interesting to note that I see a contribution to the hadron production from hard processes that goes from $\sim 40\%$ at central events to an almost negligible amount for 40–50% central events (certainly consistent with 0 within model dependencies and systematic errors). This is what one would expect, since the energy density of the fireball is proportional to the system size.

For $\eta \neq 0$ I have no reliable values for n_{pp}, so I have not tried to make the calculation for my 60^o and 40^o numbers. However I can use the ratios between my extracted values for B in table 8.24 to estimate that the ratio for central events stays roughly the same at $\eta \approx 0.55$ and drops to

$$F^{\eta\approx 1}_{0-5\%} \approx 0.29 \tag{8.48}$$

at $\eta \approx 1$.

Comparing these numbers to the results from the fit, shown in table 8.23, there is clearly a large difference between the two analyses. In both cases F_{Hard} varies with centrality, but in absolute value the fit results are way higher. The main reason for this difference is probably that while the two methods are essentially identical the K&N analysis constrains the fit to go through the *pp* point at $N_{Part} = 2$. Extrapolating the curves in figure 8.29 show that they do not intersect this point.

Conclusion

I have shown that we see a major contribution to our charged particle multiplicities that scales with N_{Coll}, sinking with increasing rapidity and decreasing centrality. My extracted scaling is consistent with one presented by the PHENIX collaboration, at least within model dependent errors. Using an eikonal formalism constraining the fit to my points to pp data produces the same qualitative behavior as for a "pure data" fit, but much lower absolute values of F_{Hard}.

Chapter 9

Conclusions and outlook

In the two preceding chapters I have presented the vertex finding capability of the BRAHMS experiment, and an analysis of the charged particle multiplicity $dN/d\eta$ around midrapidity for $Au - Au$ collisions at $\sqrt{s} = 130AGeV$. Below I briefly summarize my main results and give some thoughts about possible future developments.

9.1 Vertex finding

9.1.1 Results

The BRAHMS global detectors, BB and ZDC, are efficient at determining the global z position, but their precision is not good enough for precise PID. I have shown that relative to well–determined TPC vertices (see below) we have

$$\sigma_z^{BB} \approx 2.6cm \tag{9.1}$$

and

$$\sigma_z^{ZDC} \approx 3.5cm \tag{9.2}$$

I have presented the current status of more precise vertex finding with TPM1, the first midrapidity TPC, and shown that the two existing algorithms give results that are well correlated with the global measurements. The algorithms are nicely complementary, and in total $\sim 60\%$ efficient for $|z| < 35cm$.

BrTPMClusterVertexModule is the most precise algorithm, showing

$$\sigma_z^{CVTX} \approx 0.1cm \tag{9.3}$$

versus GEANT simulations for all MRS angles. It is, however, quite slow because of the combinatorial nature of the algorithm, and quite inefficient at lower spectrometer angles where the cluster multiplicity is high. Its strength is currently for medium cluster densities, but this will improve significantly when TPM1 is rebuilt and less noisy.

BrTPMTrackVertexModule is a quick algorithm, but inefficient for low cluster multiplicities since it requires several tracks to make a good measurement. With the MRS at 90^o it shows

$$\sigma_z^{TVTX,90^o} \approx 0.2cm \tag{9.4}$$

versus GEANT simulations, rising to

$$\sigma_z^{TVTX,35^o} \approx 0.8cm \tag{9.5}$$

at 35^o, reflecting the fact that its 3D least–squares fit is very imprecise in the direction along the tracks. However, with the new crash–free **BrTrackFollowFinder** it is by far the most efficient algorithm, especially at lower spectrometer angles.

9.1.2 Outlook

The performance of both **BrTPMClusterVertexModule** and **BrTPMTrackVertexModule** will greatly improve once TPM1 is rebuilt and consequently gets less noisy. Especially the ClusterVertex will make a quantum leap in both speed and efficiency. The TPM1 vertex will never rival the BB and ZDC in efficiency because of the need for a minimum amount of clusters in the TPC, but for central events efficiency will hopefully not be a problem for post–year–one BRAHMS data.

Software–wise, both algorithms need some cleaning up to become fully compatible with the current BRAT philosophy, and **BrTPMClusterVertexModule** needs a small revision to precisely determine the y coordinate. Both of these are relatively small changes, and if all goes well I will have had time to fix them by the time I have my exam. If not, any BRAT developer should be able to make these changes without too much effort.

Also, a vertexing module for TMA and SMA data is currently being developed. When ready, this will further increase the precision and efficiency of our total vertexing capabilities, and hopefully provide the missing x coordinate. The class **BrVertexModule** is a good base class for combining all of these different measurements into one global BRAHMS vertex.

9.2 $dN/d\eta$ from TPM1

9.2.1 Results

I have presented a measurement of centrality dependent $dN_{Ch}/d\eta$ in $Au-Au$ collisions at $\sqrt{s}=130AGeV$, using the front midrapidity TPC of the BRAHMS

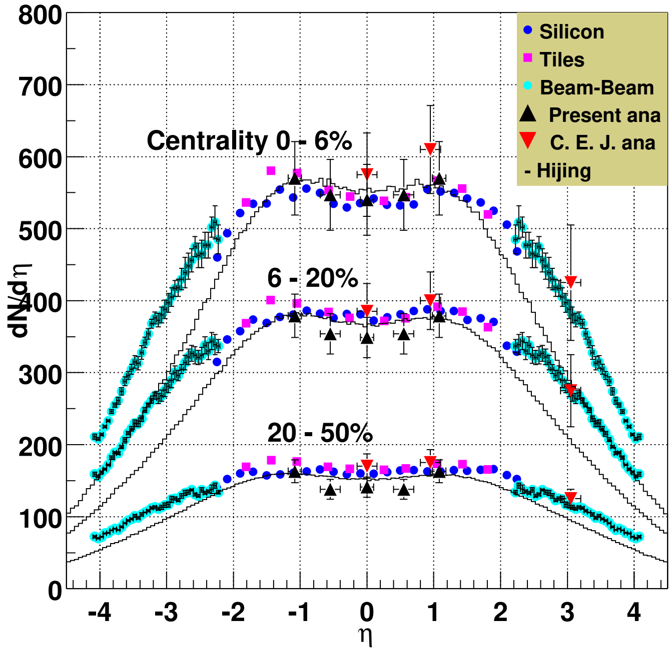

Figure 9.1: $dN/d\eta$ from TPM1, compared with predictions from HIJING (histogram), the analysis made by Claus E. Jørgensen in [61] and preliminary numbers from the BRAHMS globals. My points are reflected about $\eta = 0$. Error bars include statistical and systematic errors.

experiment (TPM1). My results for pseudorapidity $\eta = 0$, 0.55 and 1.1 are shown in figure 9.1 where they can be seen to be consistent with measurements from the BRAHMS globals and a similar analysis using TPM1 made by Claus E. Jørgensen. I have also shown that my numbers are lower than, but still barely consistent with, a similar measurement at $\eta = 0$ made by the PHENIX collaboration, and almost identical to one made by the PHOBOS collaboration.

My measured $\frac{dN}{d\eta}|_{\eta=0}$ for 0–5% central collisions is $553{\pm}4^{+50}_{-39}$. This is in the lower end of the range of multiplicities expected from various event generators, and consistent with predictions from the HIJING model (see fig. 9.1). Other models like UrQMD and FRITJOF have been shown to predict a too high charged particle production at all measured rapidities. A naive interpretation of this is that the physics included in HIJING, the contribution of hard and soft processes plus jet quenching and nuclear shadowing, provide a good description of energy deposition around midrapidity at this energy. However, HIJING fails to reproduce $\bar{p}/p$ ratio measured by BRAHMS, indicating that the model does not describe the degree of stopping well.

$dN/d\eta$ from TPM1 joins the other BRAHMS detectors in measuring a dip at midrapidities. This effect, signaling a transition from a Landau scenario of high stopping to a more transparent Bjorken scenario, has not before been seen in full charged hadron spectra from heavy ion collisions.

Finally, I have used my numbers to extract an estimate of the scaling of the charged hadron production with $N_{Participants}$ and $N_{Collisions}$ through

$$\frac{dN}{d\eta} = A \cdot N_{Part} + B \cdot N_{Coll} \tag{9.6}$$

My derived values of B indicate a fraction of hadrons produced by hard processes that is constant $B \approx 0.41$ between $\eta = 0$ and $\eta = 0.55$, and then drops by $\sim 10\%$ to $B \approx 0.36$ at $\eta = 1.1$. My measurement at $\eta = 0$ is consistent with one presented by the PHENIX collaboration. Using this fit to extract the fraction F_{Hard} of hadrons produced in hard scatterings at $\eta = 0$ gives me a value of $F_{Hard} \approx 77\%$ at central events and dropping to $F_{Hard} \approx 60\%$ at $N_{Part} = 66$. Similar results were shown for the other values of η.

I also used a simplistic eikonal approach, formulated as

$$\frac{dN}{d\eta} = (1-x)n_{pp}\frac{< N_{Part} >}{2} + xn_{pp} < N_{Coll} > \tag{9.7}$$

to estimate F_{Hard}. This analysis gave qualitatively similar results, but with much lower absolute values since it constrains my fit to go coincide with pp data. F_{Hard} is here seen to decrease smoothly with centrality to a value consistent with 0 for centralities $> 30\%$.

9.2.2 Outlook

One of the great expectations the community had of the first RHIC data was that they would be able to differentiate between different theoretical scenarios, as well as extending the known systematics of AA collisions to higher energies. While the data presented in this thesis are not enough in themselves to accomplish this, they fit well in with both other BRAHMS measurements and those of other collaborations to start to give us an idea of what goes on in nuclear collisions at an energy not before reached in an experiment.

All in all, the BRAHMS experiment has made a very good determination of $dN/d\eta$ at $\sqrt{s} = 130AGeV$, showing the first sign of a "dip" at midrapidity due to nuclear transparency. This result is corroborated by our measurement of the $\bar{p}/p$ ratio. We have also seen the onset of a stronger scaling of hadron production with $N_{Collisions}$.

In a few weeks time, RHIC goes on–line again for year two of running, this time at its maximum energy of $\sqrt{s} = 200AGeV$. BRAHMS is ready to take even better data than in year one, and we expect to quickly produce new measurements of total particle production as well as spectra of identified hadrons over a rapidity interval of ~ 8 units for this new energy regime. This will provide the heavy–ion community with unprecedented data on the systematics of baryon stopping, produced energy densities etc. Hopefully this will bring us even closer to our goal of understanding the reaction mechanisms of ultrarelativistic heavy ion collisions and the properties of excited QCD matter, and maybe give an answer to whether or not we are able to produce and study a deconfined, thermalized Quark–Gluon Plasma.

Appendix A

$dN/d\eta$ for the official BRAHMS centrality classes

At the BRAHMS collaboration meeting in april 2001, it was decided that the official centrality classes for use in our publications should be 0–5%, 5–10%, 10–20%, 20–30%, 30–40% and 40–50%. In chapter 8 I presented my results for a slightly different set, and instead give just the final results for the official classes below. See table A.1 and A.2. I also include the altered numer of participants in table A.3.

	$dN/d\eta$ per unit of η		
Centrality (%)	90^o	60^o	40^o
0–5	$553{\pm}4^{+50}_{-39}$	$557{\pm}6^{+50}_{-39}$	$579{\pm}4^{+52}_{-41}$
5–10	$438{\pm}3^{+35}_{-31}$	$452{\pm}5^{+36}_{-32}$	$475{\pm}4^{+38}_{-33}$
10–20	$316{\pm}3^{+25}_{-22}$	$321{\pm}5^{+26}_{-23}$	$347{\pm}3^{+28}_{-24}$
20–30	$200{\pm}2^{+14}_{-12}$	$198{\pm}3^{+14}_{-12}$	$223{\pm}2^{+16}_{-13}$
30–40	$120{\pm}1^{+8}_{-7}$	$126{\pm}2^{+9}_{-8}$	$140{\pm}2^{+10}_{-8}$
40–50	$73{\pm}1^{+4}_{-4}$	$73{\pm}2^{+4}_{-4}$	$85{\pm}1^{+4}_{-4}$

Table A.1: Charged particle production ($dN/d\eta$) normalized to one unit of pseudorapidity, including statsitical and systematic errors.

	$\frac{dN}{d\eta}/0.5 \cdot N_{Part}$ per unit of η		
Centrality (%)	90^o	60^o	40^o
0–5	$3.27{\pm}0.02^{+0.33}_{-0.23}$	$3.29{\pm}0.04^{+0.33}_{-0.23}$	$3.43{\pm}0.03^{+0.34}_{-0.24}$
5–10	$3.03{\pm}0.02^{+0.27}_{-0.21}$	$3.13{\pm}0.04^{+0.28}_{-0.22}$	$3.28{\pm}0.02^{+0.30}_{-0.23}$
10–20	$2.87{\pm}0.02^{+0.29}_{-0.20}$	$2.92{\pm}0.04^{+0.29}_{-0.20}$	$3.15{\pm}0.03^{+0.32}_{-0.22}$
20–30	$2.60{\pm}0.02^{+0.23}_{-0.16}$	$2.58{\pm}0.03^{+0.23}_{-0.15}$	$2.89{\pm}0.02^{+0.26}_{-0.17}$
30–40	$2.33{\pm}0.03^{+0.28}_{-0.16}$	$2.45{\pm}0.04^{+0.29}_{-0.17}$	$2.72{\pm}0.03^{+0.32}_{-0.19}$
40–50	$2.22{\pm}0.04^{+0.29}_{-0.20}$	$2.22{\pm}0.06^{+0.29}_{-0.20}$	$2.58{\pm}0.04^{+0.33}_{-0.23}$

Table A.2: Charged particle production ($dN/d\eta$) per number of participant pairs, normalized to one unit of pseudorapidity. Includes statsitical and systematic errors.

Centrality (%)	$< N_{Part} >$
0–5	338
5–10	289
10–20	220
20–30	154
30–40	103
40–50	66

Table A.3: The avereage number of participating nucleons in each centrality class. Numbers from BAN26.

Appendix B

How to get and use ROOT and BRAT

Assuming that the reader has a computer account at the RHIC Computing Facility (RCF) and access to the BRAHMS CVS cell, this is a short HowTo on getting and setting up the software packages ROOT and BRAT, and some application packages.

B.1 ROOT

ROOT is freely obtainable over the net, from

```
root.cern.ch
```

The *Downloads* page at this website contains both the full source tree for ROOT, and precompiled binaries for diverse linux editions, Windows and other operating systems. Since I have only used the binary versions, I will assume that the reader can also do the same.

Download a packed binary distribution to your local machine, e.g.

```
root_v3.00.06.Linux.2.4.1.tar.gz
```

Move this file to a directory where you want your ROOT to reside, and unpack it by doing

```
gunzip root_v3.00.06.Linux.2.4.1.tar.gz
tar -xvf root_v3.00.06.Linux.2.4.1.tar
```

A new directory /root/ has now been created in the current directory, containing the entire distribution.

Now, in a local setupfile like .cshrc or .bashrc, you must set some environment variables:

```
setenv ROOTSYS 'full_path_of_ROOT_dir'
setenv LD_LIBRARY_PATH ${ROOTSYS}/lib
setenv PATH ${PATH}:${ROOTSYS}/bin/:${ROOTSYS}/include
alias root=$ROOTSYS/bin/root
```

After doing this, restart your xterm or do

```
soruce .cshrc
```

or equivalent, and the command

```
root
```

should call up your ROOT distribution.

B.2 BRAT

To download the latest version of BRAT, you must first acquire a CVS token. This is a verification that you are allowed to access the BRAHMS cell of the CVS repository. To do this, log into *rcf.rhic.bnl.gov* and issue the command

```
klog
```

You will be prompted for your AFS password, and after giving that you can log out of rcf again. Now, move to a directory where you want BRAT to be installed, and call

```
cvs checkout brat
```

This created a new directory /brat/ in the current directory, containing the entire latest BRAT version.

If you already have BRAT installed and simply want to update any files that have changed in CVS, you have the option of instead invoking

```
cvs update brat
```

This saves disk space, but you may run into problems when CVS attempts to merge any changed files with ones you have changed in your own, local version.

Now you must again set some environment variables. In either .bashrc or .cshrc add the lines

```
setenv BRATSYS 'full_path_of_BRAT_dir'
setenv BRATHOME $BRATSYS
setenv BRAHMS_ARCH linux
setenv LD_LIBRARY_PATH ${LD_LIBRARY_PATH}:${BRATHOME}/lib/${BRAHMS_ARCH}
setenv PATH ${PATH}:${BRATSYS}/include:${BRATSYS}/bin/${BRAHMS_ARCH}
```

Now restart your xterm or do

```
soruce .cshrc
```

or equivalent.

After downloading BRAT, it must be compiled. To do this, do

```
cd $BRATSYS
make install
```

This compiles all the BRAT libraries, and in addition makes some programs like *bratroot* and *BrNtuple*. They should be runnable from the command prompt. *bratroot* is a script made by C. Holm that calls ROOT and automatically loads the BRAT libraries, thus eliminating the need for the normal BratLoad.C.

B.3 BRAHMS_APP

In addition to the two software packages above, many useful BRAT applications are placed in the CVS package brahms_app. To get this, obtain a CVS token as described above and go to a directory where you want it installed. Then do

```
cvs checkout brahms_app
```

and it will be placed under a new directory /brahms_app/.

Appendix C

Reconstruction parameters

This appendix contains a brief summary of the most relevant software parameters used in my $dN/d\eta$ analysis.

DetectorParameters.txt

This is the TPM1 entry in **DetectorParameters.txt**:

```
TYPE:BrDetectorParamsTPC
NAME:TPM1
   fTwoPar:        0.80
   fDlong:         0.04
   fDtrans:        0.05
   fEff:           0.97
   fDriftVelocity:    0.0013
   fRowDistance:   4.0
   fNumberOfRows:  14
   fPadsprow:      96
   fPadDistance:   .39
   fPadWidth:      .35
   fPadLength:     2.95
   fAnodeGap:      0.4
   fTimeBucket:    100.0
   fNoBuckets:     158
   fShapingTime:   180.0
   fADCGain:       8.0
   fADCChannels:   1024
   fNumberOfRows:      12
   fTimeBasePosition:  12.5
   fTimingOffset:      500.0

   fRowPosition[irow] = (Float_t)-3.05*5.5  + (Float_t)(3.05*irow);
```

```
fRowPosition: 1  -16.775
fRowPosition: 2  -13.725
fRowPosition: 3  -10.675
fRowPosition: 4   -7.625
fRowPosition: 5   -4.575
fRowPosition: 6   -1.525
fRowPosition: 7    1.525
fRowPosition: 8    4.575
fRowPosition: 9    7.625
fRowPosition: 10   10.675
fRowPosition: 11  13.725
fRowPosition: 12  16.775
fRowActive:    1  kTRUE
fRowActive:    2  kTRUE
fRowActive:    3  kTRUE
fRowActive:    4  kTRUE
fRowActive:    5  kTRUE
fRowActive:    6  kTRUE
fRowActive:    7  kTRUE
fRowActive:    8  kTRUE
fRowActive:    9  kTRUE
fRowActive:   10  kTRUE
fRowActive:   11  kTRUE
fRowActive:   12  kTRUE
```

Geometry file

This is the TPM1 entry in **mrs.geo**:

```
DETECTOR=TPM1    TYPE:TRAK
 Det size   x = 38.4000 cm
 Det size   y = 20.0000 cm
 Det size   z = 36.6000 cm
 rotation ang =  90.006875 deg.
 Det center x =  94.49  cm
 Det center y =   -0.20 cm
 Det center z =   -0.13 cm
```

Cluster- and TrackFinder parameters

In my reconstruction program, I set the following parameters for **BrTPCClusterFinder** and **BrTrackFollowFinder**:

```
t1_localtrack = new BrTrackFollowFinderModule(t1name, "t1 Local Track Module");
t1_localtrack->GetClusterFinder()->SetMaxPixelCutoff(10.0);
t1_localtrack->GetClusterFinder()->SetLowCutPsig(0.6);
t1_localtrack->GetClusterFinder()->SetHighCutPsig(1.5);
t1_localtrack->GetClusterFinder()->SetLowCutTsig(0.6);
t1_localtrack->GetClusterFinder()->SetHighCutTsig(2.2);

tracker = (BrTrackFollowFinder*)t1_localtrack->GetTrackFinder();
tracker->SetSearchWidthX(0.60);
tracker->SetSearchWidthY(0.0);
tracker->SetHitSearchWidthX(0.3);
tracker->SetHitSearchWidthY(0.6);
tracker->SetTrackingMethod(1);
tracker->SetLocalTrackLimit(1000);
```

Appendix D

The BRAHMS collaboration

At the time of writing, the BRAHMS collaboration has the following members and institutions:

I. G. Bearden[7], D. Beavis[1], Y. Blyakhman[6], J. Brzychczyk[4], B. Budick[6], H. Bøggild[7], C. ChasmanÅ[1], P. Christiansen[7], J. Cibor[4], R. Debbe[1], E. Enger[2], J. J. Gaardhøje[7], K. Grotowski[4], J. I. Jordre[9], F. Jundt[3], K. Hagel[8], O. Hansen[7], A. Holm[7], C. Holm[7], A. K. Holme[2], H. Ito[11], E. Jacobsen[7], A. Jipa[10], C. E. Jørgensen[7], E. J. Kim[5], T. Kosic[4], T. Kreutgel[4], T.M.Larsen[2], J. H. Lee[1], Y. K. Lee[5], G. Løvhøiden[2], Z. Majka[4], A. Makeev[8], B. McBreen[1], M. Mikelsen[2], M. Murray[8], J. Natowitz[8], B. S. Nielsen[7], K. Olchanski[1], D. Ouerdane[7], J. Olness[1], R. Planeta, F. Rami[3], D. Roehrich[9], B. Samset[2], S. Sanders[11], I.S.Zgura[10], R. A. Sheetz[1], Z.Sosin[10], P. Staczel[7], T.F. Thorsteinsen[10] +, T.S. Tveter[2], F. Videbæk[1], R. Wada[8], A. Wieloch[4].

[1] Brookhaven National Laboratory, Upton, NY 11973-5000, USA
[2] Fysisk Institutt, University of Oslo, Blindern, Norway.
[3] IReS, University Louis Pasteur, Strasbourg, France.
[4] Jagiellonian University, Krakow, Poland.
[5] Johns Hopkins University, Baltimore, USA.
[6] New York University, USA.
[7] Niels Bohr Institute, University of Copenhagen, Denmark.
[8] Texas A&M University, College Station. USA
[9] University of Bergen, Norway.
[10] University of Bucharest, Romania
[11] University of Kansas, USA.
+ Deceased.

Bibliography

[1] D. E. Groom et al. Review of Particle Physics. *Europ. Ph. J.*, C15, 2000.

[2] F. Halzen and A. D. Martin. *Quarks & leptons.* Wiley, 1984.

[3] R. Barate et al. Observation of an excess in the search for the standard model Higgs boson at ALEPH. *Phys. Lett.*, B495:1–17, 2000. hep-ex/0011045.

[4] C. W. de Jager et al. *At. and Nucl. Data Tabl.*, 14:479–508, 1974.

[5] E. V. Shuryak. *Zh. Eksp. Theor. Fiz.*, 74:408, 1978.

[6] E. V. Shuryak. *Phys. Lett.*, B78:150, 1978.

[7] S. A. Bass, M. Gyulassy, H. Stocker, and W. Greiner. Signatures of quark-gluon-plasma formation in high energy heavy-ion collisions: A critical review. *J. Phys. G*, G25:R1, 1999. hep-ph/9810281.

[8] L. D. Landau and E. M. Lifshitz. *Statistical Physics, Part 1*, volume 5 of *Course of Theoretical Physics.* Pergamon Press, 3rd edition, 1980.

[9] Fridolin Weber. Strangeness in neutron stars. *J. Phys.*, G27:465–474, 2001. astro-ph/0008376.

[10] A New State of Matter created at CERN. CERN Press release, February 2000.

[11] Gunnar Løvhøiden. *Et kurs i eksperimentell tung-ione fysikk.* UiO, 1997.

[12] L. Ahle et al. Antiproton production in Au + Au collisions at 11.7-A-GeV/c. *Phys. Rev. Lett.*, 81:2650–2654, 1998.

[13] J. Bachler et al. Hadron production in nuclear collisions from the NA49 experiment at 158-GeV/c/A. *Nucl. Phys.*, A661:45–54, 1999.

[14] I. Bearden et al. Rapidity dependence of antiproton to proton ratios in Au + Au collisions at $\sqrt{s} = 130 GeV$. *Subm. to Phys. Rev. Lett.*, 2001.

[15] Cheuk-Yin Wong and Zhong-Dao Lu. Multiple–collision models or high–energy nucleus–nucleus collisions. *Phys. Rev. D*, 39:2606–2616, 1989.

[16] Dmitri Kharzeev and Marzia Nardi. Hadron production in nuclear collisions at RHIC and high density QCD. 2000. nucl-th/0012025.

[17] Hong Pi. An event generator for interactions between hadrons and nuclei: FRITIOF version 7.0. *Comput. Phys. Commun.*, 71:173, 1992.

[18] K. Werner. Strings, pomerons and the VENUS model of hadronic interactinos at ultrarelativistic energies. *Phys. Rep.*, 232, 1993.

[19] X N Wang and M Guylassy. HIJING: A Monte Carlo model for multiple jet production in pp, pA, and AA collisions. *Phys. Rev. D*, 44:3501, 1991.

[20] H. J. Drescher, M. Hladik, S. Ostapchenko, and K. Werner. A unified treatment of high energy interactions. *J. Phys. G*, G25:L91, 1999. hep-ph/9903296.

[21] S. A. Bass et al. Microscopic models for ultrarelativistic heavy ion collisions. *Prog. Part. Nucl. Phys.*, 41:225–370, 1998. nucl-th/9803035.

[22] K. J. Eskola, K. Kajantie, P. V. Ruuskanen, and K. Tuominen. Scaling of transverse energies and multiplicities with atomic number and energy in ultrarelativistic nuclear collisions. *Nucl. Phys.*, B570:379, 2000. hep-ph/9909456.

[23] T. Sjostrand. PYTHIA 5.7 and JETSET 7.4 physics and manual. CERN Geneva - TH. 7112 (94/02,rec.Mar.) 310 p. and e: CERN th-7112-93.

[24] T. Sjostrand and M. Bengtsson. *Comp. Phys. Comm.*, 43, 1987.

[25] X N Wang and M Guylassy. HIJING 1.0: A Monte Carlo Program for Parton and Particle Production in High Energy Hadronic and Nuclear Collisions. Program writeup. Supplied with source code, avaliable from xnwang@nsdssd.lbl.gov.

[26] K. Kajantie, P. V. Landshoff, and J. Lindfors. *Phys. Rev. Lett.*, 59:2517, 1987.

[27] B. Andersson, G. Gustafson, G. Ingelman, and T. Sjostrand. Parton Fragmentation and String Dynamics. *Phys. Rept.*, 97:31, 1983.

[28] J. Ashman et al. EM Collab. *Phys. Lett*, 202B:603, 1988.

[29] A.H.Mueller and J. Qiu. *Nucl. Phys.*, B 268:427, 1986.

[30] S. A. Bass et. al. Last call for RHIC predictions. In [80].

[31] K. J. Eskola, P. V. Ruuskanen, S. S. Rasanen, and K. Tuominen. Multiplicities and transverse energies in central a a collisions at RHIC and LHC from pQCD, saturation and hydrodynamics. 2001. hep-ph/0104010.

[32] K. J. Eskola and K. Kajantie. Baryon-to-entropy ratio in very high energy nuclear collisions. *Z. Phys.*, C75:515, 1997. nucl-th/9610015.

[33] K. J. Eskola, V. J. Kolhinen, and P. V. Ruuskanen. Scale evolution of nuclear parton distributions. *Nucl. Phys.*, B535:351–371, 1998. hep-ph/9802350.

[34] K. J. Eskola, V. J. Kolhinen, and C. A. Salgado. The scale dependent nuclear effects in parton distributions for practical applications. *Eur. Phys. J.*, C9:61–68, 1999. hep-ph/9807297.

[35] Josef Sollfrank et al. Hydrodynamical description of 200-A-GeV/c S + Au collisions: Hadron and electromagnetic spectra. *Phys. Rev.*, C55:392–410, 1997. nucl-th/9607029.

[36] B. B. Back et al. Charged particle multiplicity near mid-rapidity in central Au + Au collisions at $\sqrt{s_{NN}} = 56AGeV$ and $130AGeV$. *Phys. Rev. Lett.*, 85:3100–3104, 2000. hep-ex/0007036.

[37] K. Adcox et al. Centrality dependence of charged particle multiplicity in Au Au collisions at $\sqrt{s_{NN}} = 130GeV$. 2000. nucl-ex/0012008.

[38] Thomas Vik. Λ– og $\bar{\Lambda}$–produksjon i bly–bly–kollisjoner ved $158GeV/c$ per nukleon. Master's thesis, University of Oslo, 2001.

[39] F. Antinori et al. Production of strange and multistrange hadrons in nucleus nucleus collisions at the SPS. *Nucl. Phys.*, A661:130–139, 1999.

[40] Nicola Carrer. Results on multi–strange baryons from NA57. In [42].

[41] Francesco Prino et al. J/psi suppression in Pb Pb collisions at CERN SPS. 2001. hep-ex/0101052.

[42] *Quark matter '01 Proceedings*. To be published in Nucl. Phys. A.

[43] Alexandre Lebedev. Direct photons in WA98. In [42].

[44] H. Specht. Experimental conference summary. In [42].

[45] RHIC design manual. Technical report, BNL. www.rhichome.bnl.gov/NT-share/rhicdm/.

[46] Flemming Videbaek et al. *Nucl. Phys.*, A566, 1994.

[47] Eli Renate Grüner. Simuleringsstudier av λ–rekonstruksjon i tungioneeksperimentet BRAHMS. Master's thesis, University of Bergen, 1999.

[48] W. R. Leo. *Techniques for nuclear and particle physics experiments.* Springer-Verlag, 1994.

[49] Pawel Staszel and Jerzy Cibor. Test of the T3 Detector. BRAHMS Analysis Note 27, Niels Bohr Institute, University of Copenhagen, Institute of Nuclear Physics, March 2001.

[50] Ramio Debbe. Stop the press !!: Rings out of RICH. BRAHMS Analysis Note 15, Brookhaven National Laboratory, November 2000.

[51] The NA49 Collaboration. Projectile fragmentation in Pb+Pb collisions at 158 AGeV. NA49 Note number 133, 1997.

[52] J. Roland. Results from PHOBOS. In [42].

[53] K. Adcox. Measurement of the mid-rapidity transverse energy distribution from $\sqrt{s_{nn}} = 130gev$ Au + Au collisions at RHIC. 2001. nucl-ex/0104015.

[54] B. Zajc. Results from PHENIX. In [42].

[55] K. H. Ackermann et al. Elliptic flow in Au + Au collisions at $\sqrt{s_{NN}} = 130GeV$. *Phys. Rev. Lett.*, 86:402–407, 2001. nucl-ex/0009011.

[56] C. Adler. Mid-rapidity anti-proton to proton ratio from Au + Au collisions at $\sqrt{s_{NN}} = 130gev$. 2001. nucl-ex/0104022.

[57] J. Harris. Results from STAR. In [42].

[58] W. G. Gong. The STAR-TPC Slow Simulator. Technical report, STAR collaboration, 1995.

[59] Jens Ivar Jørdre. Performance of the Time Projection Chambers of the BRAHMS experiment at RHIC. Master's thesis, University of Bergen, 2000.

[60] Peter H. L. Christiansen. Cluster finder manual. BRAHMS Analysis Note 10, Niels Bohr Institute, University of Copenhagen, October 2000.

[61] Claus Ekman. Charged Particle Production in Au + Au Collisions at $\sqrt{s_{NN}} = 130GeV$. Master's thesis, Niels Bohr Institute, April 2001.

[62] J. D. Bjorken. Highly relativistic nucleus-nucleus collisions: The central rapidity region. *Phys. Rev.*, D27:140–151, 1983.

[63] L. Van Hove. Multiplicity dependence of p(t) spectrum as a possible signal for a phase transition in hadronic collisions. *Phys. Lett.*, B118:138, 1982.

[64] H. Ito and S. Sanders. $dn/d\eta$ Analysis by Silicon and Tile. BRAHMS Analysis Note 26, New York University, Texas A&M University, February 2001.

[65] Claus Ekman Jørgensen and Christian Holm Christensen. Centrality estimates using the Scintilator Tiles in the Multiplicty Array. BRAHMS Analysis Note 22, Niels Bohr Institute, University of Copenhagen, February 2001.

[66] Yury Blyakhman. *Beam–beam counters and charged particle multiplicity in the BRAHMS experiment at RHIC.* PhD thesis, New York University, 2001.

[67] Michael Murray. Forward energy and multiplicity in Au Au reactions at $\sqrt{s_{NN}} = 130GeV$. 2001. nucl-ex/0102011.

[68] F. Videbæk. Results from BRAHMS. In [42].

[69] Bjørn H. Samset, Truls M. Larsen, and Trine S. Tveter. Centrality dependent $dn/d\eta$ at $\eta = 0$. BRAHMS Analysis Note 23, Fysisk Institutt, University of Olso, February 2001.

[70] Pawel Staszel. Correction for absorption. BRAHMS Analysis Note 28, Niels Bohr Institute, University of Copenhagen, April 2001.

[71] J. I. Jørdre. Comparison of on-track and off-track clusters in TPM1. BRAHMS Analysis Note 21, University of Bergen, January 2001.

[72] G. J. Alner et al. Scaling of pseudorapidity distributions at c.m. energies up to 0.9-TeV. *Z. Phys.*, C33:1, 1986.

[73] Kari J. Eskola. On predictions of the first results from RHIC. 2001. hep-ph/0104058.

[74] T. Wienold et al. Stopping and collective effects at SPS energies. *Nucl. Phys.*, A610:76c–87c, 1996.

[75] H. Appelshauser et al. Baryon stopping and charged particle distributions in central Pb + Pb collisions at 158-GeV per nucleon. *Phys. Rev. Lett.*, 82:2471–2475, 1999.

[76] P. G. Jones et al. Hadron yields and hadron spectra fom the NA49 experiment. *Nucl. Phys.*, A610:188c–199c, 1996.

[77] M. M. Aggarwal et al. Scaling of particle and transverse energy production in 208-Pb + 208-Pb collisions at 158-A-GeV. *Eur. Phys. J.*, C18:651–663, 2001. nucl-ex/0008004.

[78] F. Abe et al. Pseudorapidity distributions of charged particles produced in $\bar{p}p$ interactions at $\sqrt{s} = 630 GeV$ and 1800 GeV. *Phys. Rev.*, D41:2330, 1990.

[79] B. B. Back et al. Baryon rapidity loss in relativistic Au + Au collisions. *Phys. Rev. Lett.*, 86:1970–1973, 2001. nucl-ex/0003007.

[80] (ed.) L. Riccati, (ed.) M. Masera, and (ed.) E. Vercellin. Quark matter '99. Proceedings, 14th International Conference on ultra-relativistic nucleus nucleus collisions, QM'99, Torino, Italy, May 10-15, 1999. *Nucl. Phys.*, A661:1–765, 1999.